THE EFFECTS OF ADDITIVES ON THE FRACTURE TOUGHNESS OF MAGDOL

THE EFFECTS OF ADDITIVES ON THE FRACTURE TOUGHNESS OF MAGDOL

By

R.D. ROY

A Thesis

Submitted to the School of Graduate Studies

in Partial Fulfilment of the Requirements

for the Degree

Master of Engineering

MASTER OF ENGINEERING
(Metallurgy and Materials Science)

McMASTER UNIVERSITY
Hamilton, Ontario

TITLE: The Effects of Additives on the Fracture Toughness of Magdol

AUTHOR: Robert D. Roy, B. Sc.

SUPERVISOR: Dr. P.S. Nicholson

NUMBER OF PAGES: xviii, 213

ABSTRACT

The effects of small additions of Fe_2O_3, GeO_2, Ta_2O_5, V_2O_5, TiO_2, and SiO_2 on the microstructure and fracture toughness of magnesia enriched doloma were investigated. Effects of up to 5% additive oxides on grain growth and sintering in MgO and CaO were determined in preliminary tests. One percent additions were made to 40%, 60% and 80% MgO dolomas and the fracture toughness at temperatures up to 1500°C determined using the single edge notched beam specimen. Fracture surfaces were studied on the scanning electron microscope to determine fracture mode. Silica and Ta_2O_5 doped material showed high toughness at 1500°C possibly due to microcracks, while TiO_2 resulted in formation of a viscous grain boundary film producing high toughness at 1300°C followed by a rapid decline by 1500°C. In undoped samples increases in MgO resulted in the appearance of a toughness peak near 1300°C. This was attributed to grain boundary segregation of impurities.

ACKNOWLEDGEMENTS

I take this opportunity to express my thanks to all those people who provided help and encouragement in the course of this work. I thank in particular Dr. P.S. Nicholson for his continuing advice, Mr. M. Hasin for his aid in fabricating the specimens, Mr. V. Krstic and Mr. A. Khaund for their contributions during endless discussions and the other students and faculty of the department who have made my time at McMaster enjoyable and productive. Thanks also go to Mrs. W. Smith for typing of my sometimes obscure handwriting.

Finally I acknowledge the financial support of the National Research Council and Steetley of Canada Limited.

TABLE OF CONTENTS

			Page
CHAPTER 1	Introduction		1
CHAPTER 2	Literature Review		4
	2.1.	Calcination	4
		2.1.1. Calcination of Dolomite	4
		2.1.2. Calcination of $MgCO_3 \cdot nH_2O$	5
		2.1.3. Calcination of $CaCO_3 \cdot nH_2O$	7
	2.2.	CaO and MgO	7
		2.2.1. The Chemistry of CaO and MgO	7
		2.2.2. Solubility of Impurities	8
		2.2.3. CaO-MgO Phase Equibrium	8
	2.3.	Sintering	10
		2.3.1. Solid State Sintering	10
		2.3.2. Sintering in the Presence of of Liquid Phase	11
		2.3.3. Sintering in Multicomponent Systems	15
	2.4.	Grain Growth	18
		2.4.1. Grain Growth in Pure Systems	18
		2.4.2. Effects of Impurities on Grain Growth	19
		2.4.3. Exaggerated Grain Growth	20
		2.4.4. Grain Growth in the Presence of a Liquid	23
	2.5.	Grain Growth in CaO and MgO	29
		2.5.1. Grain Growth in CaO	29
		2.5.2. Grain Growth in MgO	31

			Page
2.6.	Additives		33
	2.6.1.	Choice of Additives	33
	2.6.2.	Silica	33
	2.6.3.	Iron Oxide	38
	2.6.4.	Titania	42
	2.6.5.	Tantalium Oxide	45
	2.6.6.	Vanadium Pentoxide	47
	2.6.7.	Tungsten Oxide	49
	2.6.8.	Germanium Oxide	51
	2.6.9.	Effect of Calcia on MgO	51
	2.6.10.	Other Systems	54
2.7.	Mechanical Properties		57
	2.7.1.	Conventional Tests	57
	2.7.2.	The Flaw Theory of Fracture	58
	2.7.3.	Effect of Porosity on Youngs Modulus	61
	2.7.4.	The Components of Effective Surface Energy	62
	2.7.5.	The Effect of Temperature on K_{1C}	71
	2.7.6.	Plasticity in MgO and CaO	72
2.8.	Determination of K_{1C}		74
	2.8.1.	Techniques for the Measurement of K_{1C}	74
	2.8.2.	Use of a Diamond Sawcut to Simulate a Sharp Crack	77
CHAPTER 3	Experimental and Preliminary Results		80
3.1.	Raw Materials		80
	3.1.1.	Chemical Analysis	80

			Page
3.2.	Optimization of Calcination and Processing		83
	3.2.1.	Degree of Decomposition of Carbonates	83
	3.2.2.	Determination of Density	83
	3.2.3.	Effect of Calcination Temperature and Pressing Preasure on the Fired Density	87
	3.2.4.	SEM of Calcined Powders	92
3.3.	Powder Preparation		97
	3.3.1.	Preparation of Powders Following Calcination	97
	3.3.2.	The Mixing of Powders and Additives	100
3.4.	Effects of Additives on MgO and CaO Separately		100
3.5.	Ceramography		101
	3.5.1.	Magnesium Oxide	101
	3.5.2.	Calcium Oxide	102
	3.5.3.	Doloma Mixtures	102
3.6.	Pressing of Mechanical Test Specimens		103
3.7.	Firing Schedule		105
3.8.	Preparation of Test Bars		105
3.9.	Fracture Rig		106
3.10.	Calibration of the Fracture Rig		108
3.11.	SEM of Fracture Faces		108
CHAPTER 4	Results and Discussion		110
4.1.	The Effects of Additives on the Microstructure of CaO and MgO Separately		110

			Page
	4.1.1.	Introduction	110
	4.1.2.	Sintering and Grain Growth in Pure MgO and CaO	110
	4.1.3	V_2O_5 Doped MgO and CaO	112
	4.1.4.	Ta_2O_5 Doped MgO and CaO	115
	4.1.5.	TiO_2 Doped MgO and CaO	117
	4.1.6.	SiO_2 Doped MgO and CaO	119
	4.1.7.	WO_3 Doped MgO and CaO	122
	4.1.8.	GeO_2 Doped MgO and CaO	125
	4.1.9.	Fe_2O_5 Doped MgO and CaO	129
4.2.	Microstructures of the Magdol Compositions		130
	4.2.1.	Introduction	130
	4.2.2.	Microstructure of the Pure MgO/CaO Mixtures	132
	4.2.3.	Effect of SiO_2 on Magdol Microstructures	136
	4.2.4.	Effect of TiO_2 on Magdol Microstructures	137
	4.2.5.	Effect of Fe_2O_3 on Magdol Microstructures	140
	4.2.6.	Effect of Ta_2O_5 on Magdol Microstructures	142
	4.2.7.	Effect of GeO_2 on Magdol Microstructures	142
4.3.	Fracture Toughness Measurements		144
	4.3.1.	Summary of Results	144
	4.3.2.	Fracture Behavior of Undoped Magdols	144
	4.3.3.	Effect of SiO_2 on the Fracture Results	159

			Page
	4.3.4.	Effect of Ta_2O_5 on the Fracture Results	163
	4.3.5.	Effect of Fe_2O_3 on the Fracture Results	166
	4.3.6.	Effect of TiO_2 on the Fracture Results	170
	4.37.	Effect of GeO_2 on the Fracture Results	173
4.4.	Further Aspects of Toughness Results		176
	4.4.1.	Similarities and Differences	176
	4.4.2.	Corrections for Porosity Differences	180
	4.4.3.	Dependence of K_{1C} on Percent MgO	182
	4.4.4.	Effect of Liquid Viscosity	187
	4.4.5.	Subcritical Crack Extension	189
CHAPTER 5	Summary and Conclusions		199
APPENDIX I	Origin of Numerical Constant in K_{1C} Equation		204
APPENDIX II	Statistical Treatment of Experimental Data		205
References			208

LIST OF FIGURES

Figure		Page
2-1	Effect of Calcination Temperature on Fired Density of MgO	6
2-2	CaO - MgO Phase Diagram	9
2-3	Effect of Liquid Phase on Sintering	12
2-4	Sintering in the MgO - CaO System	16
2-5a	Effect of Impurities on Grain Growth	21
2-5b	Conditions for Exaggerated Grain Growth	21
2-5c	Exaggerated Grain Growth in Al_2O_3 doped with Na_2O	22
2-6	Dihedral Angle	26
2-7	Effect of Cr_2O_3 and Fe_2O_3 on ϕ	26
2-8	Effect of ϕ on Grain Growth	28
2-9	Variation of Fractional Contact Areas in CaO - MgO - Fe_2O_3	30
2-10	Grain Sizes of MgO and CaO in MgO - CaO - Fe_2O_3 System	30
2-11	SiO_2 - CaO Phase Diagram	36
2-12	MgO - SiO_2 Phase Diagram	36
2-13	CaO - MgO - SiO_2 Phase Diagram	37
2-14a	Mg - Fe - O Phase Diagram	39
2-14b	MgO - Fe_2O_5 Phase Diagram	39
2-14c	MgO - FeO Phase Diagram	39
2-15a	CaO - FeO Phase Diagram	40
2-15b	CaO - Fe_2O_3 Phase Diagram	40

Figure		Page
2-16	CaO - MgO -"Fe_2O_3" Phase Diagram at 1500°C	41
2-17	MgO - TiO_2 Phase Diagram	43
2-18	CaO - TiO_2 Phase Diagram	43
2-19	Effect of Titania on Sintering of MgO	44
2-20	MgO - CaO - TiO_2 Phase Diagram	44
2-21	MgO - Ta_2O_5 Phase Diagram	46
2-22	CaO - Ta_2O_5 Phase Diagram	46
2-23	V_2O_5 - MgO Phase Diagram	48
2-24	V_2O_3 - MgO Phase Diagram	48
2-25	V_2O_5 - CaO Phase Diagram	48
2-26	MgO - WO_3 Phase Diagram	50
2-27	CaO - WO_3 Phase Diagram	50
2-28	MgO - GeO_2 Phase Diagram	52
2-29	CaO - GeO_2 Phase Diagram	52
2-30	MgO - CaO - GeO_2 Phase Diagram	52
2-31	Effect of Calcia on Sintering of MgO	53
2-32	Temperature Dependence of Effective Surface Energy	65
2-33	Microcracking of MgO	67
2-34	Temperature Dependence of K_{1C} of Al_2O_3	70
2-35	Temperature Dependence of K_{1C} of Impure Al_2O_3	73
2-36	Load Deflection Curves of Impure Al_2O_3	73
2-37	Stress Strain Curves for MgO in Tension	75
2-38	Stress Strain Curves for MgO in Compression	75

Figure		Page
2-39	Fracture Specimens and K calibration	78
3-1	Degree of Decomposition of Carbonates	84
3-2	Effect of Calcination on Specific Gravity of MgO	88
3-3	Effect of Calcination on Bulk Density of Cao and MgO	89
3-4	Effect of Calcination and Pressing on Firing Shrinkage	91
3-5	Effect of Calcination and Pressing on Green Density of MgO	93
3-6	Effect of Calcination and Pressing on Green Density of CaO	94
3-7	Effect of Green Density on Fired Density of MgO	95
3-8	Effect of Green Density on Fired Density of CaO	96
3-9	MgO calcined at 600°C	98
3-10a	MgO calcined at 800°C	99
3-10b	MgO calcined at 800°C	99
3-11a	MgO calcined at 1200°C	99
3-11b	MgO calcined at 1200°C	99
3-12	Mold Crossection	104
3-13	Cutting of Samples	104
3-14	Testing Rig	107
4-1	Microstructure of CaO	113
4-2	Microstructure of MgO	113
4-3a	V_2O_5 Doped CaO	114
4-3b	V_2O_5 Doped CaO	114

Figure		Page
4-4	V_2O_5 Doped MgO	114
4-5a	0.5% Ta_2O_5 Doped MgO	116
4-5b	2.0% Ta_2O_5 Doped MgO	116
4-6a	1.0% Ta_2O_5 Doped SEM	116
4-6b	1.0% Ta_2O_5 Doped Ta X ray Map	116
4-7a	0.5% Ta_2O_5 Doped CaO	118
4-7b	2.0% Ta_2O_5 Doped CaO	118
4-8a	1.0% TiO_2 Doped CaO SEM	118
4-8b	5.0% TiO_2 Doped CaO SEM	118
4-9a	1.0% TiO_2 Doped MgO SEM	120
4-9b	1.0% TiO_2 Doped MgO Ti Map	120
4-10a	2.0% TiO_2 Doped CaO SEM	120
4-10b	2.0% TiO_2 Doped CaO Ti Map	120
4-11a	1.0% SiO_2 Doped CaO SEM	121
4-11b	5.0% SiO_2 Doped CaO SEM	121
4-12	1.0% SiO_2 Doped MgO SEM	121
4-13a	5.0% SiO_2 Doped MgO SEM	123
4-13b	5.0% SiO_2 Doped MgO Si Map	123
4-14a	5.0% SiO_2 Doped CaO SEM	123
4-14b	5.0% SiO_2 Doped CaO Si Map	123
4-15a	0.5% WO_3 Doped MgO	124
4-15b	2.0% WO_3 Doped MgO	124

Figure		Page
4-16a	0.5% WO_3 Doped CaO	124
4-16b	2.0% WO_3 Doped CaO	124
4-17a	0.4% GeO_2 Doped MgO	126
4-17b	2.0% GeO_2 Doped MgO	126
4-18a	0.4% GeO_2 Doped CaO	126
4-18b	2.0% GeO_2 Doped CaO	126
4-19a	0.5% Fe_2O_3 Doped CaO	128
4-19b	5.0% Fe_2O_3 Doped CaO	128
4-20a	0.5% Fe_2O_3 Doped MgO	128
4-20b	5.0% Fe_2O_3 Doped MgO	128
4-21	2.0% Fe_2O_3 Doped MgO	129
4-22a	4MP Microstructure	133
4-22b	4MP Ca X ray Map	133
4-23a	6MP Microstructure	133
4-23b	6MP Ca X ray Map	133
4-24	8MP Microstructure	134
4-25a	4MS Microstructure	134
4-25b	6MS Microstructure	134
4-26	8MS Microcracking	134
4-27a	4MTi Microstructure	138
4-27b	4MTi Ca X ray Map	138
4-28a	6MTi Microstructure	138
4-28b	6MTi Ca X ray map	138

Figure		Page
4-29	8MTi Microstructure	139
4-30	4MF Microstructure	139
4-31a	4MF Microstructure	141
4-31b	4MF Fe Map	141
4-31c	4MF Ca Map	141
4-32	6MF Microstructure	139
4-33a	4MTa Microstructure	143
4-33b	4MTa Microstructure	143
4-34	K_{1C} vs Temperature 4MP	150
4-35	K_{1C} vs Temperature 6MP	151
4-36	K_{1C} vs Temperature 8MP	152
4-37	Fracture Surface 4MP6	155
4-38	Fracture Surface 4MP11	155
4-39	Fracture Surface 4MP13	155
4-40	Fracture Surface 4MP15	155
4-41	Fracture Surface 6MP6	156
4-42	Fracture Surface 6MP11	156
4-43	Fracture Surface 6MP13	156
4-44	Fracture Surface 6MP15	156
4-45	Fracture Surface 8MP11	157
4-46	Fracture Surface 8MP13	157
4-47	Fracture Surface 8MP15	157
4-48	Fracture Surface 6MV13	157

Figure		Page
4-49	K_{1C} vs Temperature 6MSi	160
4-50	Fracture Surface 6MSi6	161
4-51	Fracture Surface 6MSi13	161
4-52	Fracture Surface 6MSi15	161
4-53	K_{1C} vs Temperature for 6MTa	164
4-54	Fracture Surface 6MTa6	165
4-55	Fracture Surface 6MTa13	165
4-56	Fracture Surface 8MTa13	165
4-57	K_{1C} vs Temperature for 6MFe	167
4-58	Fracture Surface 6MFe6	168
4-59	Fracture Surface 6MFe11	168
4-60	Fracture Surface 6MFe13	168
4-61	Fracture Surface 6MFe15	168
4-62	Fracture Surface 4MFe13	169
4-63	K_{1C} vs Temperature 6MTi	171
4-64	Fracture Surface 4MTi Rm	172
4-65	Fracture Surface 4MTi13	172
4-66	Fracture Surface 4MTi11	172
4-67	Fracture Surface 4MTi15	172
4-68	Fracture Surface 6MGe13	174
4-69	Illustration of Narrow K_{1C} vs Temperature Peak	179
4-70	K_{1C} vs % MgO Undoped	183

Figure		Page
4-71	K_{1C} vs % MgO Doped	184
4-72	Viscosity Temperature Dependence	188
4-73a	Subcritical Crack Extension in Ta_2O_5 Doped Magdol	190
4-73b	Subcritical Crack Extension in Ta_2O_5 Doped Magdol	190
4-73c	Subcritical Crack Extension in Ta_2O_5 Doped Magdol	190
4-74	Subcritical Crack Extension in Fe_2O_3 Doped Magdol	191

CHAPTER 1

INTRODUCTION

Chemically basic bricks are required to contain the steel and slag produced in the basic oxygen process. The basic oxides used are MgO and CaO with magnesite containing less than 2% CaO presently being widely used in North America. Canada has no economic source of high quality magnesite so all the magnesite used in Canada must be imported. However recent developments in Japan have demonstrated the superiority of refractories containing up to 36% CaO. Canada has a high quality deposit of dolomite in the Niagara escarpment which could thus be utilized.

Dolomite is a mixed carbonate $(Mg, Ca)CO_3$ of approximately equimolar composition which upon calcination produces doloma, a hetrogenous mixture of MgO and CaO crystals. This material is used as-is in some furnaces but is inferior to the magnesite since the CaO is the continuous phase which rapidly dissolves in iron oxide slags. This causes the refractory to lose coherence and fail rapidly. By increasing the content of MgO above that of the doloma a "Magdol" with continuous MgO phase may be formed.

The increased interest (1-3) in doloma is based on the increase of lining life achieved by the Japanese. As of August 5, 1976 the lining of the #2 vessel in #1 BOF shop of the Kimitsu works of Nippon Steel

had reached a life of 7619 heats, while in the United States, U.S. Steel claimed slightly over 2000 heats in their operations at South Works in 1973 (4).

The BOF Bricks in use at Kimitsu works have the following composition excluding carbon

MgO	60 - 86%
CaO	12 - 36%
Fluxes	1 - 6%

It has recently been postulated that a major reason for the resistance of the high MgO bricks to slag is formation of a dense layer of MgO by the reduction of MgO by carbon in the interior of the brick followed by reoxidation at the surface. It is possible that the presence of the CaO grain increases the strength of the MgO poor region behind the dense layer thus preventing wholesale loss of the MgO dense layer. Thus qualities that steel making refractories must possess include good slag resistance, thermal shock resistance, abrasion resistance and refractoriness under load. All of these properities are sensitive functions of the microstructure of the brick and all but the slag resistance of the material can be related to the more fundamental parameter of fracture toughness. The measurement of the fracture toughness of ceramics has undergone much development recently and has been demonstrated as a powerful tool for the characterization of microstructures.

In view of these facts it was decided to study the development of Magdol microstructures in the presence of known dopants. In this

way it was hoped to reduce the additions of imported magnesite required to achieve satisfactory refractory properties in Canadian doloma. The fracture toughness of the materials at elevated temperatures was used in addition to direct observation of microstructure to determine the effectiveness of the additives.

CHAPTER 2

LITERATURE REVIEW

2.1. Calcination

In order to do a controlled study of the CaO - MgO system consideration must first be given to the initial calcination process.

2.1.1. Calcination of Dolomite

When dolomite is calcined, the following reaction takes place (5,6)

$$2(Ca,Mg)CO_3 \rightarrow CaCO_3 + MgO + CO_2 \qquad (2\text{-}1)$$

followed by

$$CaCO_3 \rightarrow CaO + CO_2 \qquad (2\text{-}2)$$

Differential thermal analysis curves for this reaction (7,8) indicate that reaction 2-1 occurs at 800°C and reaction 2-2 at 940°C. In view of the good agreement among several authors upon this, the earlier work by Britton et al.(8) which indicated direct decomposition of dolomite to MgO and CaO appears incorrect.

Recent work of Obst (9) indicating a large residual solid solution of CaO - MgO in the calcined material also conflicts with the more detailed work of Leipold (10,11) who found almost complete rejection of CaO and SiO_2 from MgO even at relatively high cooling rates.

Since the dolomite decomposes in two distinct stages and as high purity dolomite is not readily available it seemed appropriate to

produce artificial doloma using simple $MgCO_3$ and $CaCO_3$ as starting materials.

2.1.2. Calcination of $MgCO_3 \cdot nH_2O$

It is known that calcination temperatures markedly effect the compaction and sintering characteristics of powder compacts (14-18). It is characteristic of the literature results that MgO obtained by calcination of carbonates, oxalates or hydroxides shows different calcination and sintering behavior depending upon its source and purity. Kriek et al.(19) found "pure" $MgCO_3$ to decompose over the range 200° - 500°C, as would be expected from equibrium considerations (20) while natural magnesite decomposed between 500°C and 650°C. Iawai et al (21) also observed this behavior. Upon firing MgO produced by calcination it was found by most authors (13,14,15), in contrast to the results of Hench and Russel (22), that an optimum bulk density is obtained with calcination between 800°C and 1000°C. These results are illustrated in Figure 2-1.

Study of the structure of calcined MgO indicates that the particle size of MgO increases with calcination temperature (12,21,23,24). It has also been found that the MgO particles produced begin to rapidly sinter at approximately 1100°C with the most readily sinterable MgO powder being produced at 600°C (12). Moodie et al.(24) found that calcine produced at 550°C consisted of platelets crazed into flat crystalites approximately 150Å across. This resulted from the collapse of the

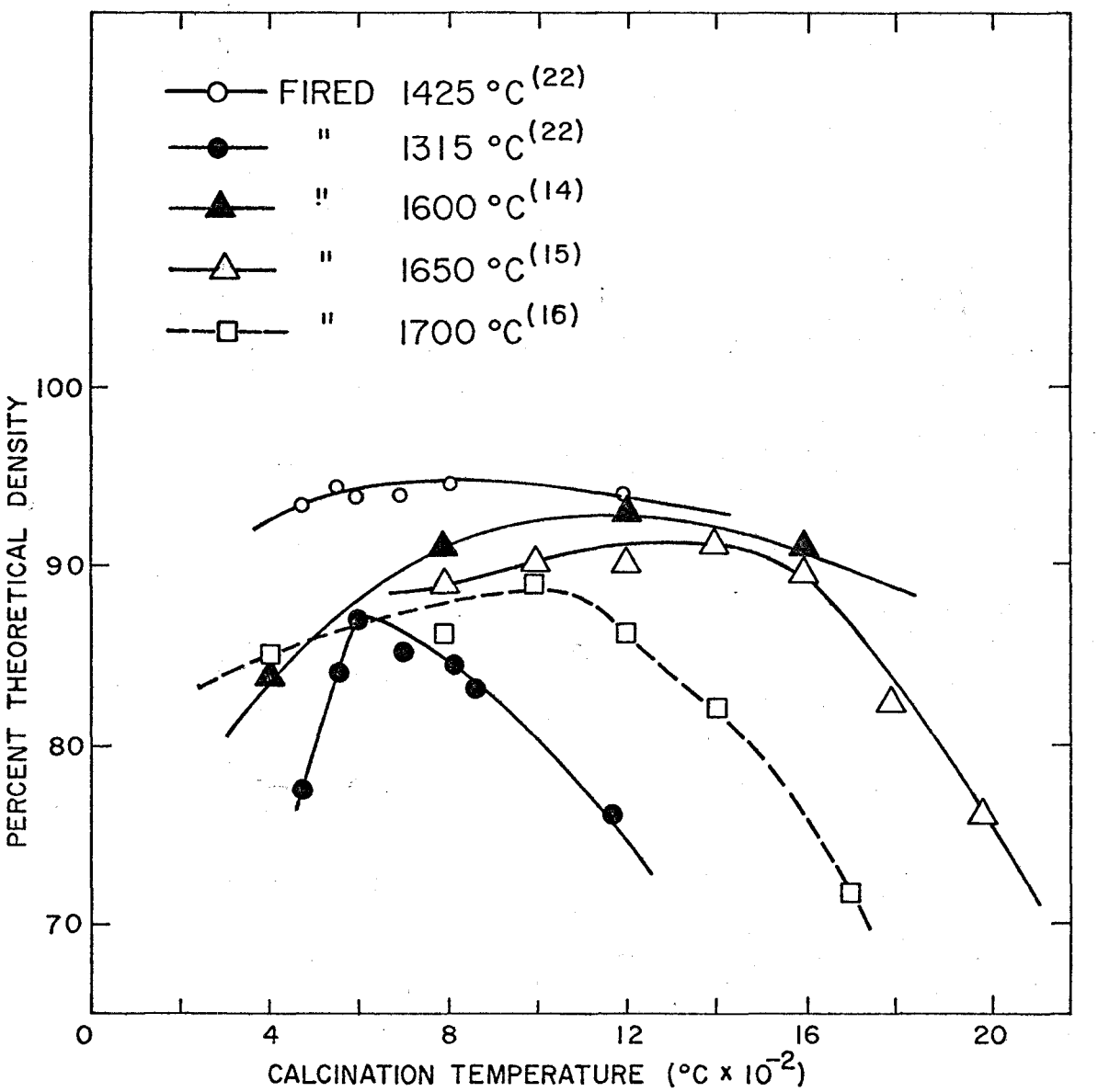

Figure 2-1 Effect of calcination temperature on sintered density.

layered carbonate structure. At higher temperatures they found more developed cubic crystalites which began to sinter together.

2.1.3. Calcination of $CaCO_3 \cdot nH_2O$

Sakadeda and Fujihara (25) studied an impure limestone, largely to investigate the effect of various salts upon the dead burning behavior. Equilibrium considerations (20) indicate that a temperature of at least 800°C is needed. Fisher (27,28) studied the effect of various preparation parameters on crystalite size and found rapid growth at 900°C. However in the absence of information on purity, no definite conclusion can be drawn from this data. Brown (26) using calcium oxalate as a starting material, found an optimum bulk density after calcination at 1000°C.

2.2. CaO and MgO

2.2.1. The Chemistry of CaO and MgO

Both CaO and MgO have the cubic NaCl crystal structure. Both are very stable having melting points of 2570°C and 2800°C respectively. These oxides are highly stoichiometric and show characteristic sharply-curved solubility limit for other oxides. However, as the densification and grain growth processes in these oxides are diffusion controlled, it is important to consider the role of impurities in creating lattice defects.

In these oxides most impurities occupy substitutional positions

as discussed by Cutler (29) and Cutler and Jones (30), so that the vacancy concentration may be enhanced by aliovalent impurities. Thus the addition of Ti^{+4}, Fe^{+3}, Si^{+4}, for Mg^{+2} promotes cation vacancies, as would the substitution of F^- or Cl^- for O^{-2}. Since most MgO and CaO available commercially is less than 99.9% pure the diffusion behavior will be in the extrinsic range for all practical temperatures.

2.2.2. Solubility of Impurities

Due to the relatively high stability of CaO and MgO only limited solubility is observed for many oxides. Leipold (12,30) showed, using microprobe techniques, that in electronic grade MgO, CaO and SiO_2 segregated to grain boundaries even upon rapid quenching. A similar effect is also shown by the hardening of grain boundaries in Al_2O_3 doped with MgO as found by Jorgenson and Westbrook (31). This concentration of impurities at grain boundaries could thus have large effects upon the surfaces of both MgO and CaO grains which in turn will markedly effect the equilibrium microstructures developed during firing as is discussed later.

2.2.3. CaO - MgO Phase Equilibrium

The most recent CaO - MgO phase diagram (Figure 2-2) available is that of Domain et al.(32), who used quenching and x-ray techniques to determine the extent of solid solubility in this system. There is considerable conflict between their results and those of Leipold (12, 13) who detected segregation of Al, Si and Ca near the grain boundaries

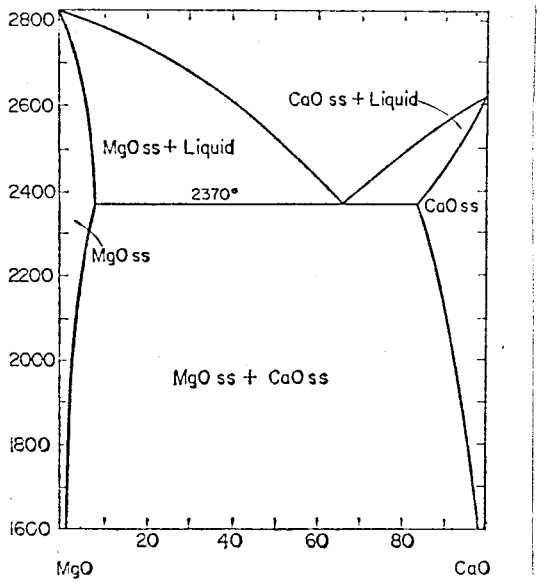

Figure 2--2 CaO MgO phase diagram.

of MgO at bulk concentrations as low as 30 ppm. This was detected in the absence of visible precipitation which Leipold interpreted as evidence that the grain boundary was wide atomicly and had a high affinity for impurities.

In a more recent study by Henny and Jones (15) involving x-ray measurement of lattice parameters the solubility of CaO in MgO at 1700°C was found to be 1.7% which is in fair agreement with the results of Domain et al.

2.3. Sintering

2.3.1. Solid State Sintering

When a powder compact is heated to a high enough temperature to allow material transport, shrinkage and densification occurs. This sintering process can be separated into three stages. The initial stage involves the formation of necks between particles. This stage is extremely sensitive to the exact nature of the surface of the particles and the atmosphere. Several possible mechanisms may operate including viscous flow (observed in many salts) and diffusion (most generally observed for metals and oxides). Once these necks have grown to a large fraction of the radius of the particles the second or intermediate stage begins.

At this point limited grain growth by particle coalescence is possible and the compact can be characterized as a continuous porosity phase penetrating a continuous solid. As this stage progresses

shrinkage continues and the continuous porosity is gradually pinched off and isolated within the solid.

When the density reaches 90 percent theoretical, the third and final stage begins with the removal of intergranular porosity by diffusion of vacancies and extensive grain growth may occur. Detailed reviews of the theoretical and practical aspects of solid state sintering have been written by Cutler (12), Thummler and Thomma (135), Stuijts (136), Johnson (137) and Beere (138).

2.3.2. Sintering in the Presence of a Liquid Phase

It has often been found that the presence of a liquid phase during sintering results in a dramatic increase in the rate of densification (Figure 2-3) and a marked reduction of the temperatures required for densification. There have been several recent reviews of the topic by Eremenko (44), White (45), Huppman (46), and Whalén and Haveluk (47). All agree that Kingery's (48) kinetic analysis of the mechanism is correct. Kingery identified three stages in the process;

1. Initially rapid densification of the powder compact is brought about by the particles sliding over each other under the influence of capilliary forces and reduced friction.
2. A solution reprecipitation process, if the solid is soluble in the liquid phase. The particles will preferentially dissolve at the contact points thus allowing shrinkage.

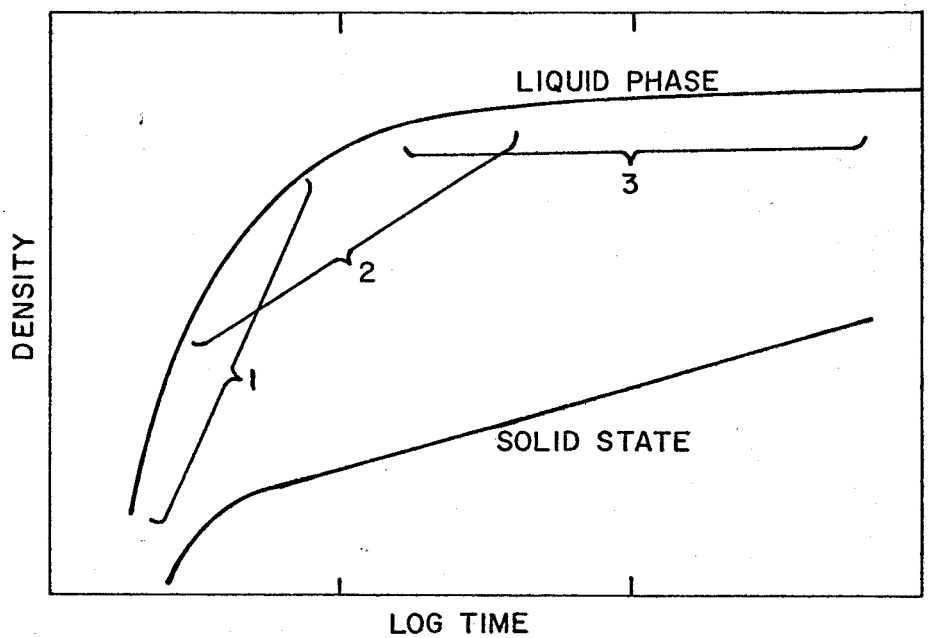

Figure 2-3 Sintering kinetics with and without a liquid phase: 1. particle rearrangement
2. solution reprecipitation
3. solid state

3. Once the solid particles come in direct contact, only normal diffusive transport processes will occur and densification will markedly slow and will resemble solid state sintering kinetics.

In the earlier stages of this process the viscosity of the liquid, the solubility of the solid phase in the liquid and the dihedral angle between the liquid and solid are important parameters which influence the densification behavior. This they do by modifying the forces required to rearrange the particles, the rate of solution at the contact points and the capillary forces produced respectively. Aspects of these effects are discussed elsewhere in this chapter.

A serious drawback to the liquid phase sintering technique is that if the compact retains the liquid phase at its working temperature serious reductions of strength may occur. Problems like this have been overcome in the steel industry where low concentrations of sulfur result in a film of iron sulfide completely enclosing the iron grains. Additions of manganese to the iron results in the formation of MnS which does not "wet" the iron grains and in turn results in the preservation of strength of the metal at high temperatures. It is interesting to note that below 1000°C iron sulphide is a solid whose equilibrium angle (discussed in more detail in Section 2.3.3.) is greater than 60° and it therefore crystalizes as discrete particles of FeS rather than as a grain boundary film. The result of this is that sufficient FeS to cause hot shortness will not substantially affect the room temperature

properties of steel or its microstructure.

It is possible for an additive to the doloma system to have a similar effect of improving the hot strength of the impure material.

There are other possible ways in which the benefits of liquid phase sintering may be attained without the loss of strength at high temperature. Rice (109) fabricated fully dense MgO by use of a 2 percent LiF additive and hot pressing. Analysis of the material following fabrication indicated almost complete loss of the additive and mechanical tests indicated no loss of room temperature strength. Subsequent tests of the temperature dependence of strength showed little loss of strength to 1500°C (Ref. 157 and Section 2.8.3.). The technique of using a fugitive liquid to attain fully dense and often transparent ceramics is finding increased application.

Another alternative which may avoid the high temperature loss of strength is that proposed by Tacvorian (66,67,68), by which an additive might melt forming a non-equibrium liquid which would aid densification. Later as equibrium is approached a refractory solid solution or refractory compound might be formed with the primary phase. Layden and McQuarie (72) found evidence of such compound formation in their work on the sintering of MgO with V_2O_5 and WO_3 additions by observation of "fluoresence" of the specimens. Unfortunately the exact nature of these results is not reported and no clearcut conclusion is therefore possible.

2.3.3. Sintering in Multicomponent Systems

There has been little work done on the kinetics of sintering in multicomponent nonreacting ceramic systems (43). Some work involving sintering in the presence of more than 10% liquid has been discussed by Kuczynski (43) and Eramenko (44). Kriek et al, (19) have worked in the periclase, lime and iron oxide system, again with more than 10% liquid present.

Often multicomponent systems react forming stable or metastable interoxide compounds or solid solutions which may hinder sintering. Due to unequal diffusion flows (the Kirkendall - Hartely effect), vacancies may precipitate on the side of the oxide whose diffusivity is greater, causing large deformation of the neck geometry thus interfering with sintering.

Kriek et al, (19) found that mixtures of CaO and MgO did show inhibition of sintering with increasing numbers of unlike contacts - as shown in Figure 2-4. They suggested that this phenomenom could be the result of a large difference in the coefficient of thermal expansion of the two phases causing disruption of the points of contact. The literature (154) values of $12.6 \times 10^{-6} {}^{\circ}C^{-1}$ and $13.7 \times 10^{-6} {}^{\circ}C^{-1}$ for MgO and CaO respectively are sufficiently close to cast doubt upon this mechanism, especially since a large portion of the sintering is carried out isothermally.

An alternative explanation presented was that interparticle diffusion was inhibited by the complete insolubility of MgO and CaO. It is now known however that there does exist limited solubility at high temperatures.

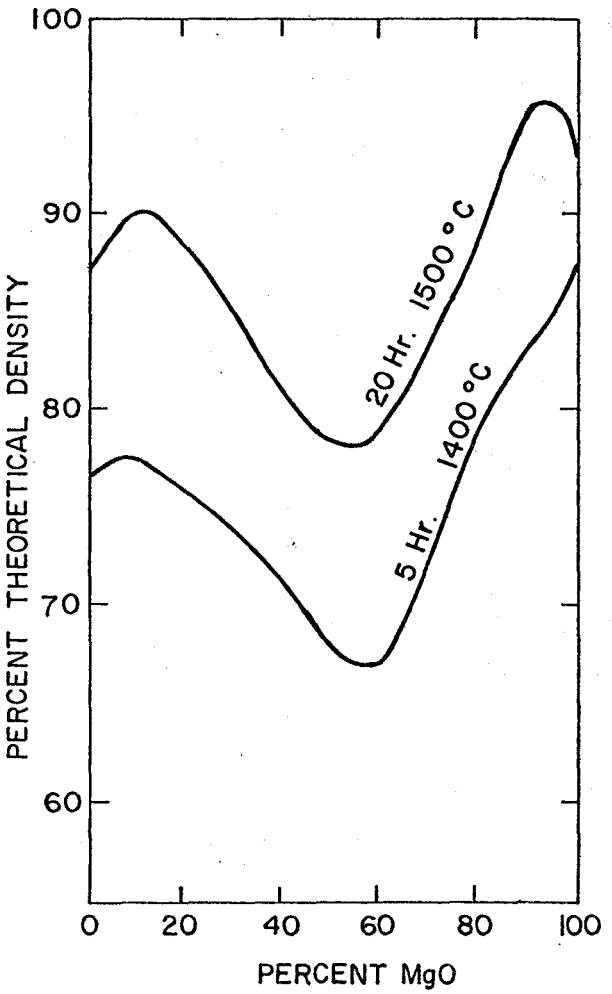

Figure 2-4 Sintering in the MgO-CaO system.

This is more plausible as it can be seen from the phase diagram that solubility is limited at temperatures below 1500°C. It could be anticipated that the use of higher sintering temperatures would tend to reduce the magnitude of the effect although solubility remains limited at all subliquidus temperatures.

In Kriek et al. work on the addition of SiO_2, TiO_2, Al_2O_3 and Fe_2O_3 to MgO, it was found that all improved sintering in low concentrations while only Fe_2O_3 enhanced sintering in higher concentrations (>5%). It was noted that the formation of $MgO \cdot Al_2O_3$, $2MgO \cdot SiO_2$ and $2MgO \cdot TiO_2$ resulted in expansions of 8%, 20% and 22% respectively while formation of $MgO \cdot Fe_2O_3$ exhibited no expansion.

It was accordingly proposed that expansion due to reaction at the relatively few contact points between MgO and the additive could provide a physical explanation of the higher densities observed with the lower concentration of additives. If the increase in density is due exclusively to the sintering at the unlike contact points then the like contact points in the shell around the additive particle should prevent shrinkage. An expansion at the unlike contacts will result in particle rearrangement and attendant densification. This is plausible in the case of additions which remain solid at sintering temperatures and form compounds by solid state reaction.

2.4. Grain Growth

2.4.1. Grain Growth in Pure Systems

Most theoretical studies of grain growth have been conducted with high purity metals. Aust and Rutter (134) showed that very low levels of impurities markedly reduce growth rates in tin. Ceramic systems should be even more sensitive to the effects of impurities since extrinsic diffusion is expected to much higher purity levels. In addition, the nature of grain boundaries in ceramics is much more complex as discussed thoroughly by Westbrook (130). Another major difference between grain growth in metals and ceramics is that growth in metals often starts from homogenous nucleation of stress free grains in a strained matrix while in ceramics it often begins from a mixture of extremely small grains in a continuous net of porosity.

The theory of normal grain growth is based upon the reduction of interfacial free energy providing the driving force. It can be shown that

$$D^2 - D_o^2 = K_o t \exp\left[-Qb / RT\right] \qquad (2\text{-}3)$$

where D is grain size at time t

D_o is initial grain size

K_o constant

Qb grain boundary diffusion activation energy

R gas constant

T temperature

Many authors have noted that this law seldom holds as the activation energy for grain growth is often much higher than that for grain boundary diffusion and the exponential relation between D and t is often greater than 2.0.

2.4.2. Effects of Impurities on Grain Growth

Several possible causes for deviation from the ideal grain growth laws have been considered by various authors. Hilbert (132) and Feltham (133) reformulated the equations in terms of alternate grain growth and disappearance criterion but arrived at similar rate laws. In metals a common effect is the collection of impurity "atmospheres" near the grain boundaries resulting in an effective drag force. Cahn (129) has analysed this case in detail. In ceramic systems this effect is more pronounced. Jorgenson and Westbrook (31) found that concentrations of MgO at the grain boundaries of Al_2O_3 markedly influenced grain growth. Leipold (12,13) has also detected significant grain boundary segregation of impurities in MgO. Hollenberg and Gordon (31a) attributed the anomalously high activation energies for sintering to these impurities as well. If the impurity is insoluble it is often found to impede the grain growth by pinning the boundaries at precipitates thus giving rise to an upper limit to grain growth.

The condition for limiting grain size (D_1) has been predicted to be related to the inclusion diameter (d) and volume fraction of inclusions (f) by the following relation

$$D_1 = \frac{2d}{3f} \approx \frac{d}{f} \qquad (2\text{-}4)$$

This effect is illustrated in Figure 2-5a, b. Arias (103) found a refinement of grain size occurred in MgO with dispersions of tungsten metal and boron carbide.

2.4.3. Exaggerated Grain Growth

Burke (33) proposed that if the grain boundaries are sufficiently mobile they may break away from the impurity atmosphere or inclusions thus leading to exaggerated grain growth. Such growth is often observed when the inhibiting phase is disappearing or coalescing. Rutter (78) demonstrated this in wustite. In Figure 2-5b the grain size (D) changes expected and the limiting grain size (D_1), assuming a cubic rate law for pore coalescence, are presented.

If the initial particle size is D_o then only very limited grain growth can occur until $D_1 = D_o$. At this point grain growth can occur at a rate controlled by the change of D_1 provided the grain boundary mobility is high. If the mobility is lower than that permitted by pore removal then the grain size will ultimately be controlled solely by the boundary mobility.

In either of the preceding cases, grain growth will be "normal". However if the boundary mobility is high enough for pore removal to be limiting, a series of growth steps may give rise to large grains having high boundary curvature thus providing enough driving force to allow migration of the boundary past the pores. These may then be trapped inside the grains where they are difficult to remove. As more such large

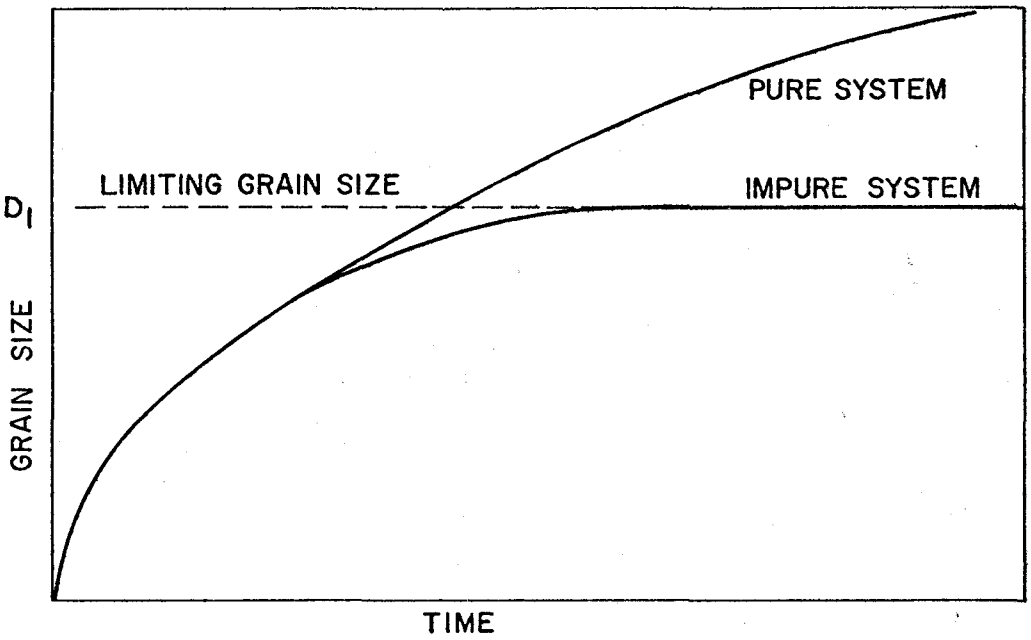

Figure 2-5a Effect of impurities or inclusion on grain growth

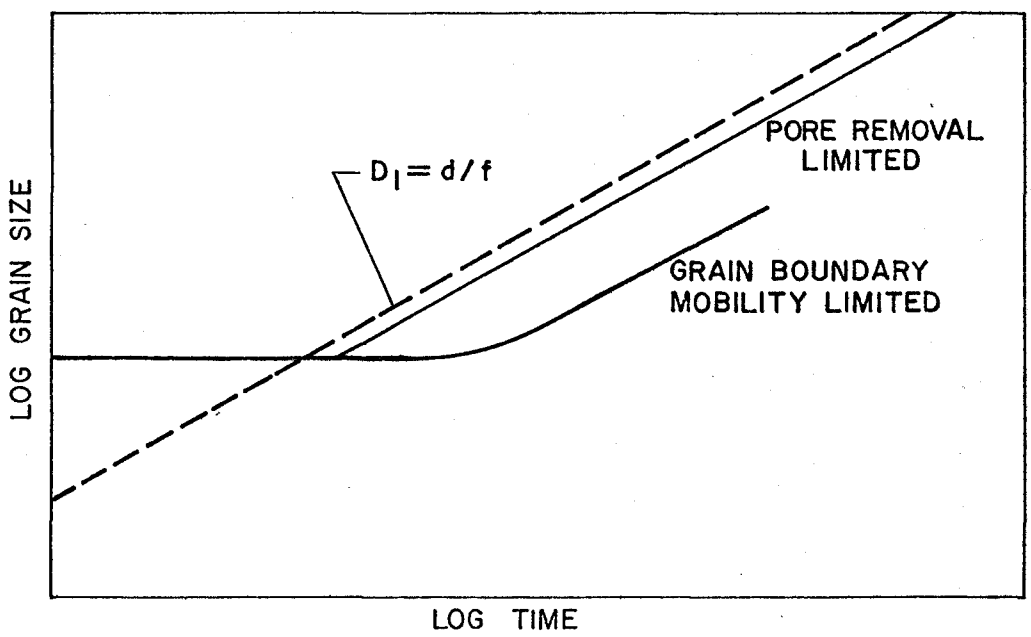

Figure 2-5b Conditions for exaggerated grain growth

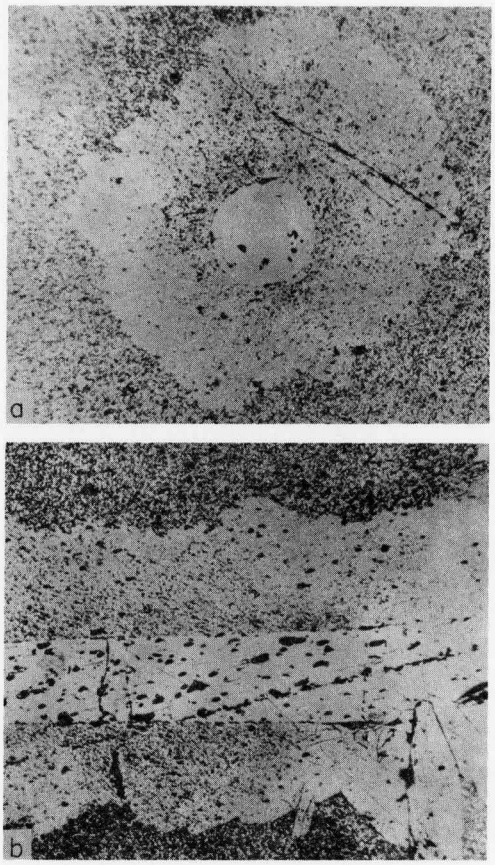

Figure 2-5c Exaggerated grain growth in Al_2O_3 around a Na_2O doped saphire rod (from Cutler (141)).

multi-faceted grains develop, a double peak will appear in the grain size distribution. As the number of large grains increases and the new grains grow the smaller grains are eliminated and the new larger grains again follow normal growth laws. The presence of soluble impurities at the grain boundaries should prevent such exaggerated grain growth and permit achievement of higher densities. That this is true has been demonstrated in MgO doped Al_2O_3 by Westbrook (31), and is the basis for production of the fully dense translucent Al_2O_3 known as Lucalox.

There is considerable evidence that exaggerated grain growth can also occur as a result of impurities. Cutler (12) quotes four authors who have shown in work at Utah that exaggerated grain growth in Al_2O_3 is induced by low concentration of impurities, particularily Na_2O.

It has been found that alumina with less than 1000 PPM Na_2O will produce exaggerated growth. Cutler also refers to work in which alumina doped with iron oxide did not show exaggerated grain growth in air but did so in the presence of Na_2O vapor. The effect of Na_2O can clearly be seen in Figure 2-5c, where sapphire rods doped with Na_2O are surrounded by exaggerated grains while the matrix retains the finer "normal" grain size.

It is thus clear that impurities may perform a dual role in ceramic systems either preventing or producing exaggerated grain growth.

2.4.4. Grain Growth in the Presence of a Liquid

In the presence of a reactive liquid at the grain boundaries the diffusion of the primary phase will be greatly increased. This may

remove limitations on grain growth caused by soluble impurities. However, the liquid phase may also be regarded as rounding the grains thus reducing the driving force arising from boundary curvature.

Lay (155) studied grain growth in the UO_2-Al_2O_3 system and found that as little as ½% alumina resulted in a doubling of the grain size of the UO_2 when annealing was carried out above the melting point of Al_2O_3. He also developed the relation first proposed by Greenwood (79) for the growth of soluble particles dispersed in a liquid. Lay based his work on a model of solid particles separated by a liquid layer which increased in thickness as the particle size increased. Both this approach and Greenwood's result in a growth law which depends upon the cube of time. Brown (93) observed a similar time dependence in the MgO - V_2O_5 system with as little as 0.1 cation percent vanadium. This is discussed in more detail in Section 2.6.5.

The equilibrium distribution of phases in multiphase systems can be explained on the assumption that at the intersection of three grains the surface tension forces must be in balance. This has been discussed by Eremenko (44), White (45,60), and Smith (59).

This balance will be reached when equation 2-5 is satisfied:

$$\gamma_{aa} = 2\gamma_{ab} \cos(\phi/2) \qquad (2\text{-}5)$$

where γ_{aa} is the surface tension on the a-a boundary

γ_{ab} is the surface tension on the a-b boundary

ϕ is the dihedral angle.

The dihedral angle (Figure 2-6) is very important as it determines what the equilibrium structure will be, particularly in a liquid - solid system. As the dihedral angle increases from zero, the penetration of B between A grains decreases. It is generally found experimentally that the interfacial energy between two unlike grains is less than that between two like grains which results in a higher dihedral angle and decreased penetration of the second phase.

This is confirmed by the results reported by White (60) of values of 10°, 15°, and 35° for $\phi_{CaO\text{-}CaO}$, $\phi_{MgO\text{-}MgO}$, and $\phi_{CaO\text{-}MgO}$ respectively.

In a two phase body the value of ϕ is much more sensitive to small changes in surface energy since the values of ϕ are much smaller than those of single phase systems. This indicates that small additions will more radically alter the relative values of ϕ in two phase bodies.

Previous work reported by Busit et al. (61), Stevenson and White (62), and Jackson and Ford (63), have shown that Cr_2O_3 increased the dihedral angle formed by a silicate liquid phase in contact with periclase grains while Fe_2O_3, Al_2O_3 and TiO_2 all lowered ϕ. The effect of Fe_2O_3 and Cr_2O_3 is shown in Figure 2-7.

If shrinkage during the initial stage of sintering of multicomponent systems depended upon neck growth as in the sintering of pure material then the shrinkage of a compact should increase as ϕ increases. However both Stephenson and White (62), and Richmond (64), found that the opposite

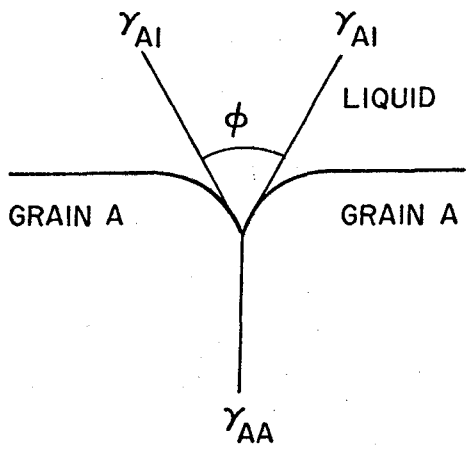

Figure 2-6 Dihedral angle between grain boundary and liquid (ref. 44)

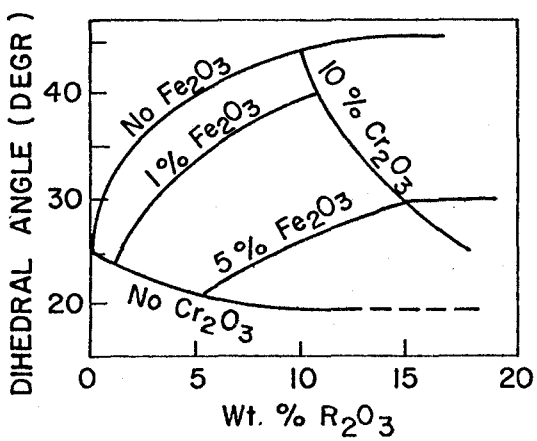

Figure 2-7 Effect of Cr_2O_3 and Fe_2O_3 on the dihedral angle in periclase at 1550°C (ref. 45)

is the case. White interpreted this result as indicating that the shrinkage is controlled primarily by the ability of the solid particles to rearrange themselves as discussed previously.

Any tendency of the grains to adhere to each other, by capillary forces, would oppose shrinkage. Any increase in the value of ϕ will increase the capillary forces of the liquid between grains. This is in accord with the observations of Stevenson and White (62), and of Eremenko (44), for a wide range of systems.

Despite the fact that most of this work was done with 10% to 20% liquid in the system, it has been shown by Richmond (65) that densification is influenced by ϕ even when less than 0.1% liquid is present.

White (60) notes that a few tenths of one percent B_2O_3 severely reduces the high temperature properties of magnesite. By refering to phase equilibrium data he shows that MgO containing 2% $2(CaO)SiO_2$ requires only 0.17% B_2O_3 for the C_2S to be completely fluxed at 1550°C. He concludes that the presence of a second solid phase is desirable in magnesite refactories in order to minimize the penetration of liquid between the periclase grains. The effects of such a penetrating liquid are discussed in Section 2.3.2.

Whalen and Humenik (47) quoted results of grain growth experiments in the presence of liquids having a range of dihedral angles (Figure 2-8). It was found that the ultimate grain size was strongly dependent upon ϕ. This is due to reduced liquid penetration between grains which results in slower mass transfer between grains.

When a liquid is in contact with two solids it must be the eutectic liquid at equilibrium. Busit et al. (61) have studied the CaO-MgO system in the presence of an iron rich liquid and found that the introduction of a second solid phase increased the total solid -

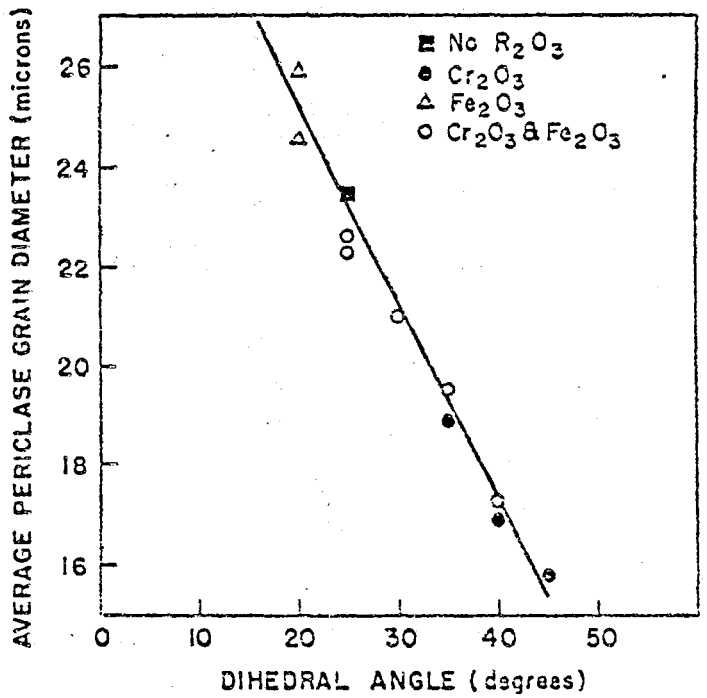

Figure 2-8 Grain growth in periclase as a function of dihedral angle for liquid phase sintered mixtures (from Whalen and Humenik (47)).

solid contact area as fractions of the total interfacial area in the system. In Figure 2-9 the ratios Ncc/N, Nmm/N, Ncm/N, and Ns/N measure resp-ectivly the CaO-CaO, MgO-MgO, CaO-MgO and total solid-solid contact area as fractions of the total interfacial area in the system. Since both Ncm/N and Ns/N reach a maximum near 50% MgO where the number of CaO-MgO contacts would be a maximum, the average area of contact between unlike grains was greater than that between like grains. White (45) interprets this as evidence that the liquid phase was less able to penetrate between unlike grains which in turn means that the surface energy of the interface between unlike grains is much lower than that between like grains.

Figure 2-10 shows how the grain size of CaO and MgO grains varies with composition and it can be seen that in the three phase region the growth of each phase was retarded in the presence of the other. This effect was greatest when the second phase content was low and White suggested that obstruction by the second solid phase was responsible. Other results reported by White (45) support this conclusion as a cubic growth law observed for the growth of both CaO and MgO separately but with both phases present a higher order law was found.

2.5. Grain Growth in CaO and MgO

2.5.1. Grain Growth in CaO

Relatively little work has been done on grain growth in this oxide and that which has been done has involved quite impure material. Rice (50) hot pressed reagent grade CaO containing 1.0% MgO and 1.5% insoluble in HCl. Both this material and material doped with 2% LiF were found to attain densities in excess of 99% theoretical.

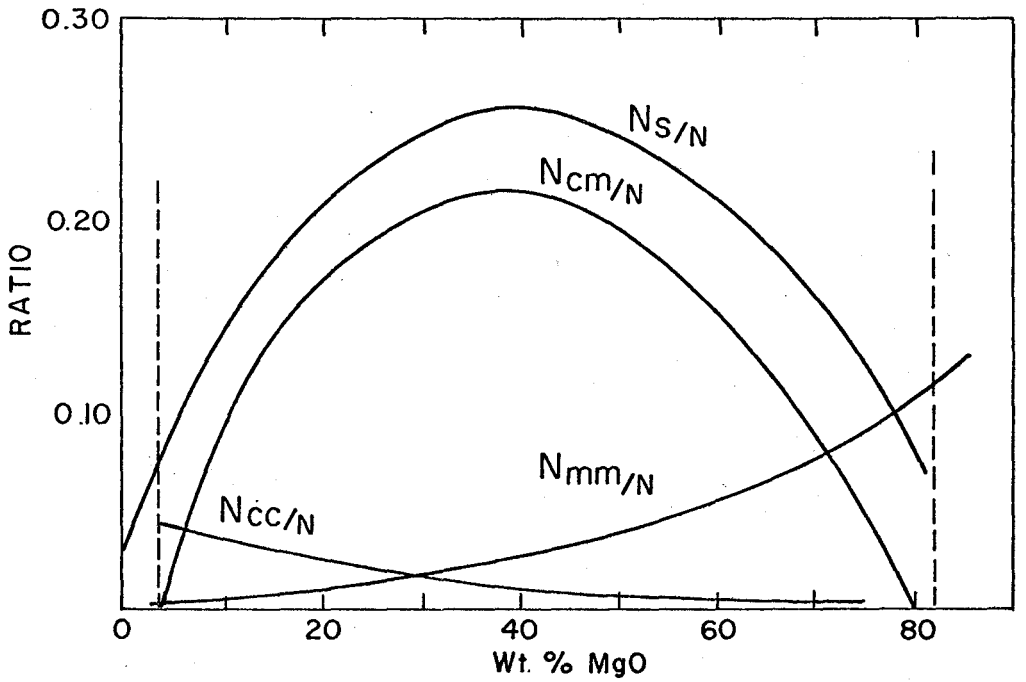

Figure 2-9 Variation of fractional contact areas in CaO-MgO-Fe_2O_3

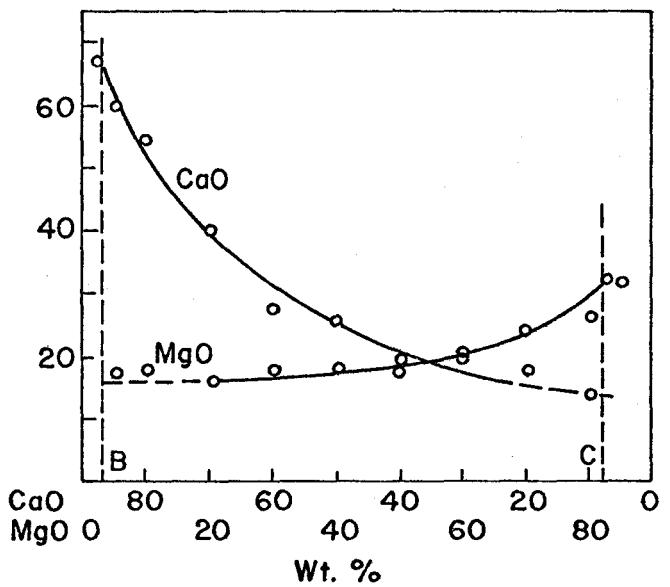

Figure 2-10 Mean grain sizes in MgO and CaO in MgO-CaO-Fe_2O_3 mixtures after firing 2 hours at 1550°C (after White (60))

Chemical studies indicated that all of the Li and all but traces of the flourine evaporated during subsequent annealing above 1300°C. Grain size data was presented indicating a grain size of 150 μm following a 1700°C anneal. Some indication was found of an increased grain size in the case of the LiF doped material, however no kinetic data was produced.

Hepworth and Rutherford (51) also utilized a very impure material containing in excess of 2% impurities of iron oxide and silica in their preliminary work on hot pressing CaO.

Only Danials et al. (49) used a reagent grade CaO to derive kinetic curves for the grain growth of CaO. They used cold pressed powder compacts annealed in air at temperatures to 1600°C for up to 60 hours. They concluded that the CaO followed "normal" grain growth kinetics proportional to the square of time. In addition they observed no influence of porosity on their results. However observation of their micrographs showed porosity trapped within the grains indicating that exaggerated growth had taken place, thus removing the pores from their boundary pinning positions. Burke (33) points out that once the larger grain size due to the exaggerated growth becomes established, normal kinetics would be observed thus accounting for these observations.

2.5.2. Grain Growth in MgO

Grain growth in MgO has been studied by many authors in both fully dense (52,53) and porous (49,54,55) materials. All of the authors cited above found that the grain growth followed the "normal" squared

growth equation 2-3. Again as in CaO, Danials et al. (49) found no effect of porosity upon the growth kinetics. The micrographs of MgO used showed a substantial amount of intragranular porosity again indicating a potential exaggerated growth step during sintering. These results for MgO are in sharp contrast to the detailed work done in Al_2O_3 by Burke (33) and Cutler (56), and for UO_2 by MacEwan (57), in which cubic kinetics were found. The cubic kinetic behavior is expected from the theory of grain growth for these ceramic materials.

However in 1970 Gordon et al. (58), in work related to creep of MgO, found that cubic growth laws applied at 1300°C and 1400°C changing to exaggerated growth at 1500°C. In addition the data of Danials (49) was re-analysed and shown to fit a cubic law as closely as the squared law.

Gordon et al. (58), also found that additions of 0.1% Fe_2O_3 prevented exaggerated growth at 1500°C which is in accordance both with theory and with similar results obtained by Coble (31) for MgO doped Al_2O_3.

It can be concluded therefore that the earlier studies indicating squared kinetics were in error, considering the level of impurities present in the MgO utilized.

2.6. Additives

2.6.1. Choice of Additives

In view of the preceding discussion, a number of additives were chosen to influence the microstructure and fracture behavior of the Magdol systems. Impurities such as silica and iron oxide which are commonly found in commercial materials were chosen as well as a number of other oxides whose phase relations with CaO and MgO were of a widely varing nature. Table 2-1 presents a typical analysis of a doloma.

Vanadium pentoxide was chosen since it was well documented that a liquid phase would form at moderate temperatures. Other oxides such as TiO_2 were considered in view of previous promising work. Finally oxides were chosen which showed promise of formation of a highly refractory compound possibly preceded by liquid formation as proposed by Tacvorian. In this way it was hoped to achieve the widest possible range of effects upon the microstructural development of the magdols while at the same time known systems could be studied for comparison.

2.6.2. Silica

Silica is a common impurity in commercial magnesite and doloma bricks. Nelson and Cutler (70,71) studied the effects of several oxides on the sintered density of MgO fired in a gas - oxygen furnace between 1200°C and 1600°C. They found that up to 2% SiO_2 increased the fired density at 1400°c but had little effect for the 1600°C firing. Layden and McQuarie (72) confirmed these results using the same techniques.

Table 2-1

Chemical Analysis of a Commercial Japanese Doloma (69)

CaO	24.0
MgO	74.0
SiO_2	.6
TiO_2	.02
Al_2O_3	.03
Fe_2O_3	1.1
Cr_2O_3	.03
Mn	.01
BaO	.006
K_2O	<.005
B_2O_3	.17
Loss	1.0

Kriek et al. (19) found that up to 10% silica aided the sintering of a more impure magnesia at 1300°C. Cutler (14) agrees with their analysis that the increased sintering is due to solution of Si^{+4} and formation of a defect structure as noted in Section 2.2.1.

From the phase diagrams in Figure 2-8, no solubility of SiO_2 in CaO exists and $2CaO{\cdot}SiO_2$ would form below 1250°C and $3CaO{\cdot}SiO_2$ above 1250°C. Thus in the CaO-SiO_2 system the possibility of a disruptive phase transformation exists with the decomposition of $3CaO{\cdot}SiO_2$ into $2CaO{\cdot}SiO_2$ and CaO at 1250°C followed by the α - γ transformation of $2CaO{\cdot}SiO_2$ at 725°C. These transformations could introduce cracking which could result in either an increase or decrease of toughness depending on its extent. All of these phases have high melting points and the possibility of non-equilibrium liquid formation appears remote.

The MgO - SiO_2 phase diagram (Figure 2-12) shows that Mg_2SiO_4 (melting point 1900°C) could be expected to form. The fosterite could then disolve in the periclase at high temperatures. The sharply curved solvus indicates that Mg_2SiO_4 would precipitate from the periclase on cooling. Again no liquid would be expected.

The ternary diagram (Figure 2-10) indicates that formation of $MgO{\cdot}CaO{\cdot}SiO_2$ which melts at 1485°C is a remote possibility during the initial non-equilibrium stages of sintering. However there is no low melting compound close enough to the compositions presently explored to expect significant liquid.

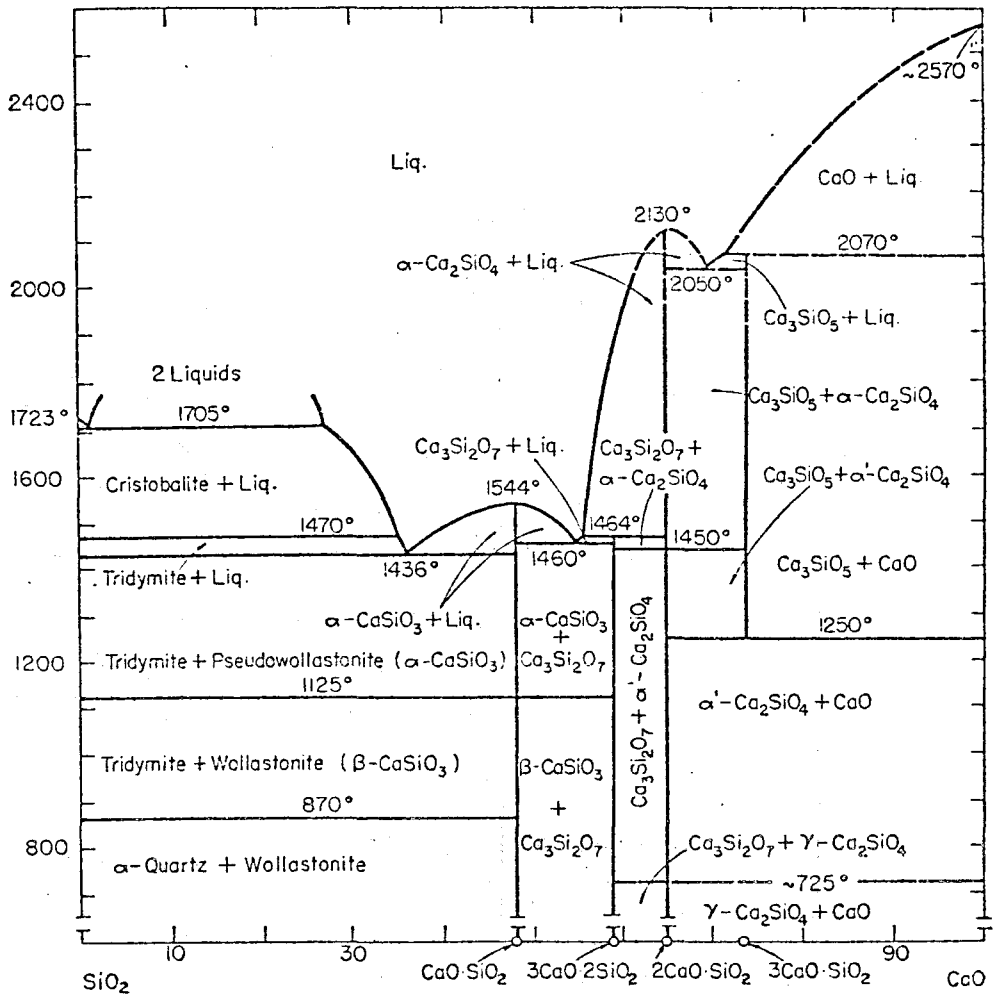

Figure 2-11 SiO - CaO Phase Diagram (Ref. 73)
2

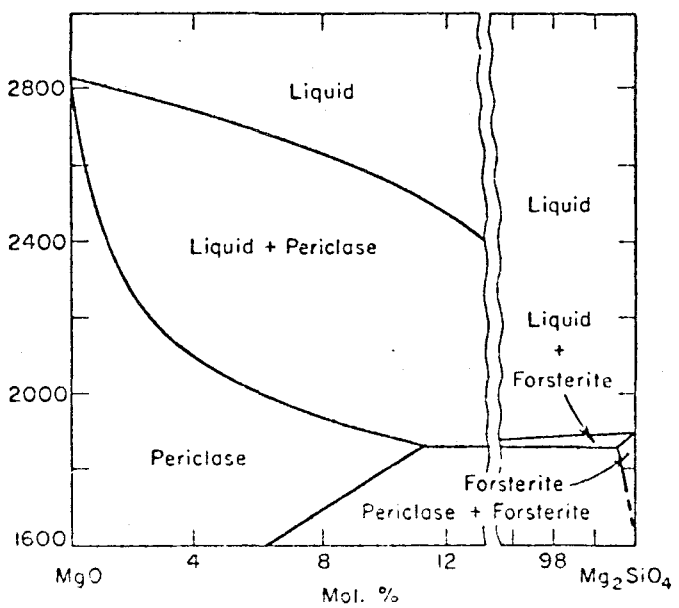

Figure 2-12 MgO - SiO_2 Phase Diagram (Ref. 74)

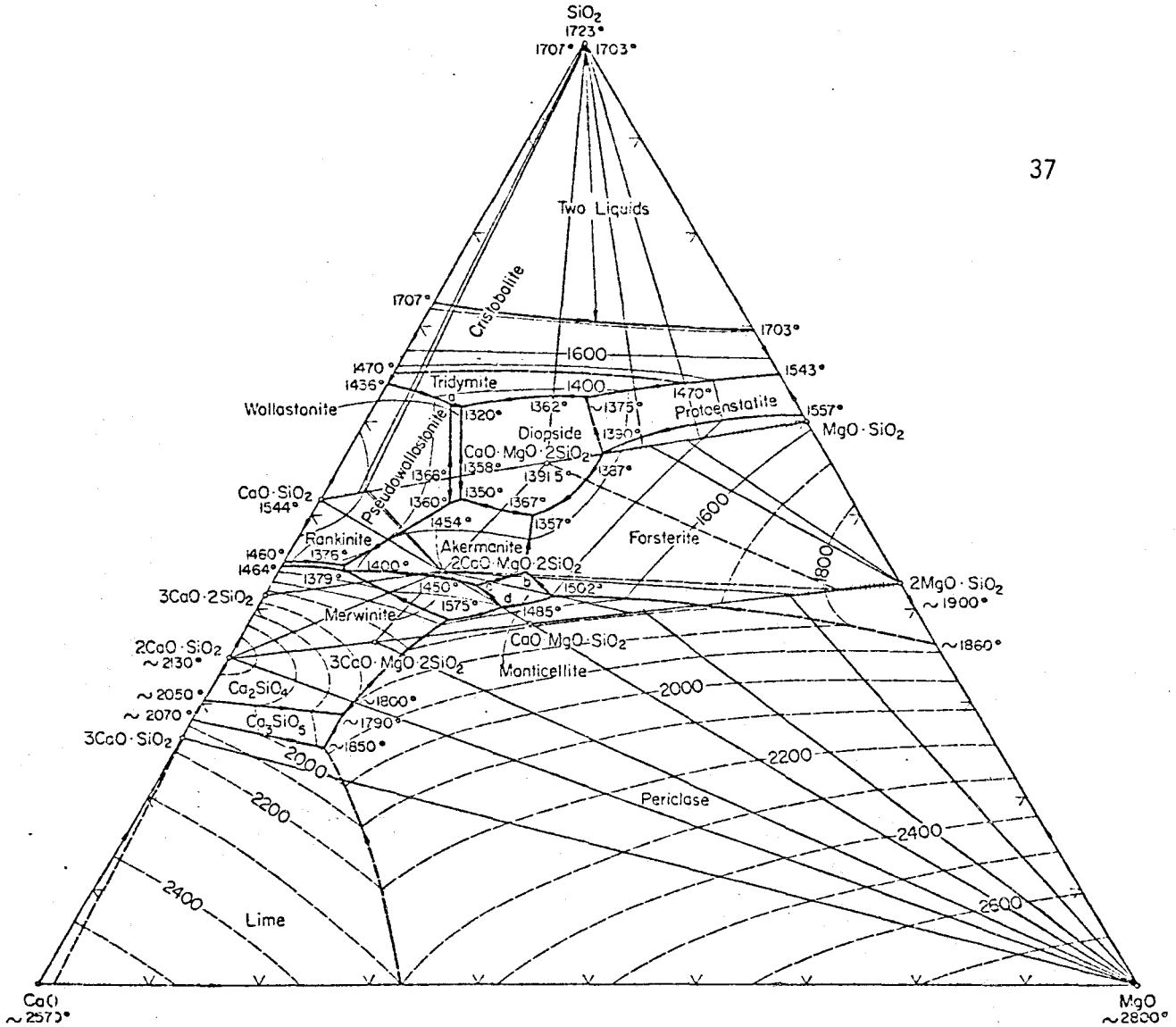

Figure 2-13 CaO - MgO - SiO_2 Phase Diagram

(Ref. 75)

Crystalline Phases

Notation	Oxide Formula
Cristobalite, Tridymite	SiO_2
Pseudowollastonite	α - CaO·SiO_2
Wollastonite	β - (Ca,Mg)O·SiO_2
Rankinite	3CaO·2SiO_2
Lime	(Ca,Mg)O
Periclase	MgO
Forsterite	2(Mg,Ca)O·SiO_2
Protoenstatite	(Mg,Ca)O·SiO_2
Diopside	(Ca,Mg)O·MgO·2SiO_2
Akermanite	2CaO·MgO·2SiO_2
Merwinite	3CaO·MgO·2SiO_2
Monticellite	(Ca,Mg)O·MgO·SiO_2

a = 1336°
b = 1430°
c = 1436°
d = 1490°

2.6.3. Iron Oxide

The effects of Fe_2O_3 on the sintering of MgO have been thoroughly investigated. Kriek et al. (19) showed that additions up to 10% of Fe_2O_3 to MgO enhances sintering up to 1500°C. Unlike SiO_2 and TiO_2 they found that increased additions of Fe_2O_3 increased the fired densities. This they attributed to the lack of expansion on formation of $MgO \cdot Fe_2O_3$.

Nelson and Cutler (70,71) in work confirmed by Layden and McQuarie (72) found that up to 3 atomic percent Fe aided sintering while larger additions hinded sintering. Layden and McQuarie proposed that this was due to 3 atomic percent Fe forming a solid solution with MgO while any excess forms the spinel phase which inhibits sintering. Cutler (14) and Cutler and Jones (29) have proposed models in which the trivalent iron ions induce vacancies in the MgO lattice to explain their role in enhancing sintering. The latter results agree with the much earlier work of Mateki (76) who worked with Manchurian magnesite.

In addition several authors have investigated the effect of iron oxides on grain growth in MgO. Kriek et al.(19) reported an increased grain size following sintering at 1500°C. Nicholson (77) found that grain growth in MgO doped with 1% Fe_2O_3 followed the following growth law:

$$D^4 = Kt \exp [-146000/RT]$$

In contrast Riegger (78) found a squared law applied to both MgO and magnesiowustite with growth in the latter phase being faster ·

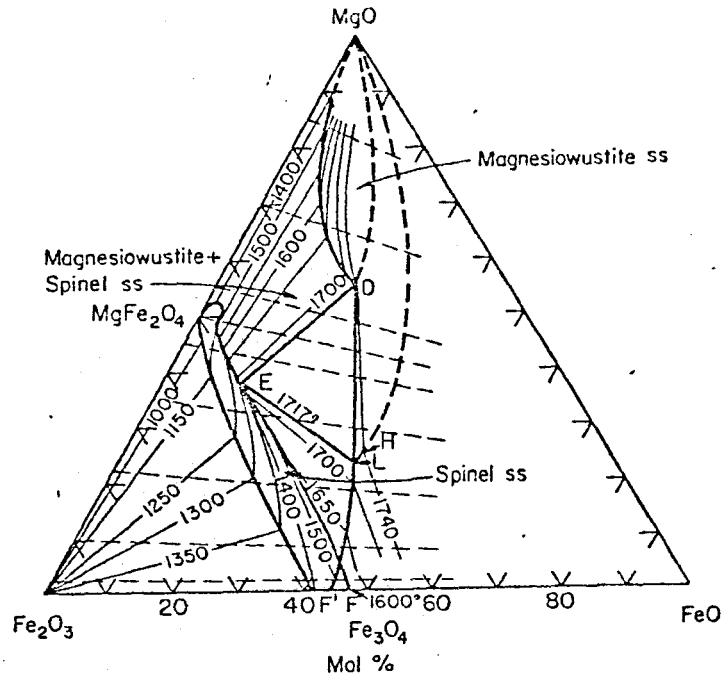

Figure 2-14a Mg - Fe - O Equilibrium Phase Diagram

(Ref. 80)

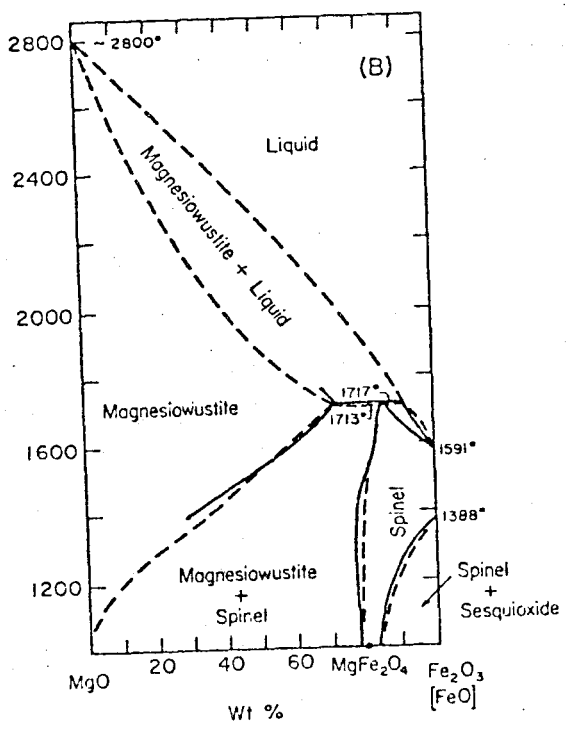

Figure 2-14b Mg - Fe_2O_3 Phase Diagram

(Ref. 81)

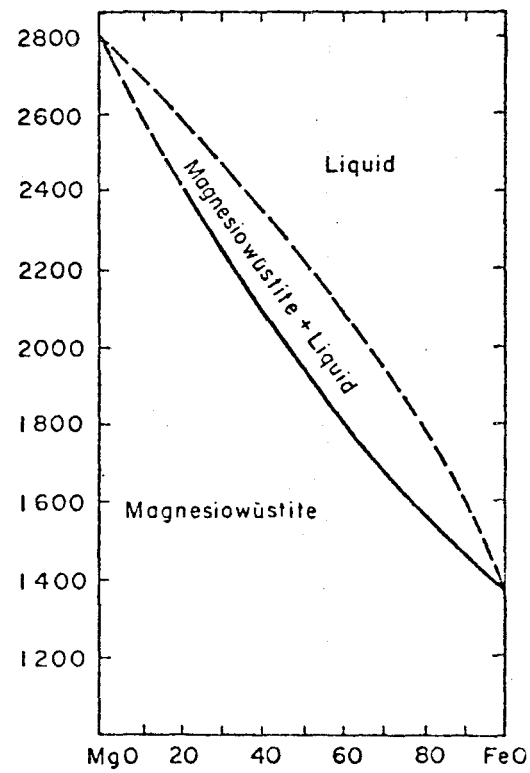

Figure 2-14c MgO - FeO Phase Diagram

(Ref. 82)

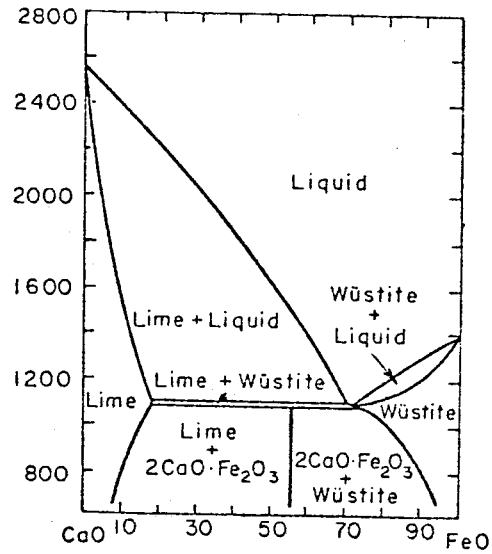

Figure 2-15a CaO - FeO Phase Diagram

(Ref. 83)

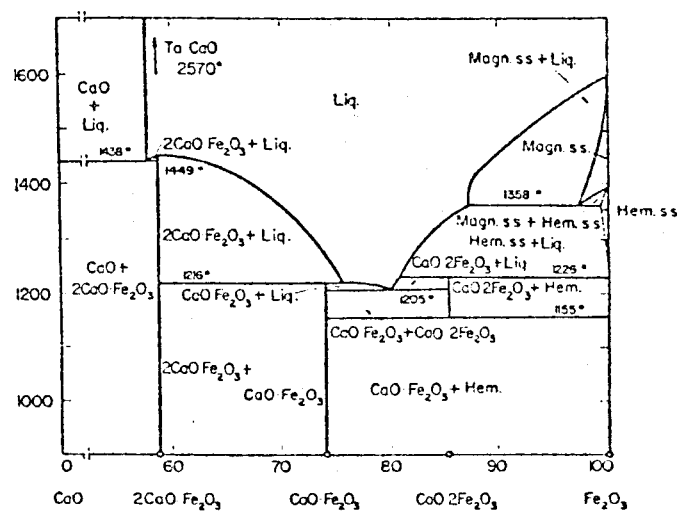

Figure 2-15b CaO - Fe_2O_3 Phase Diagram

(Ref. 84)

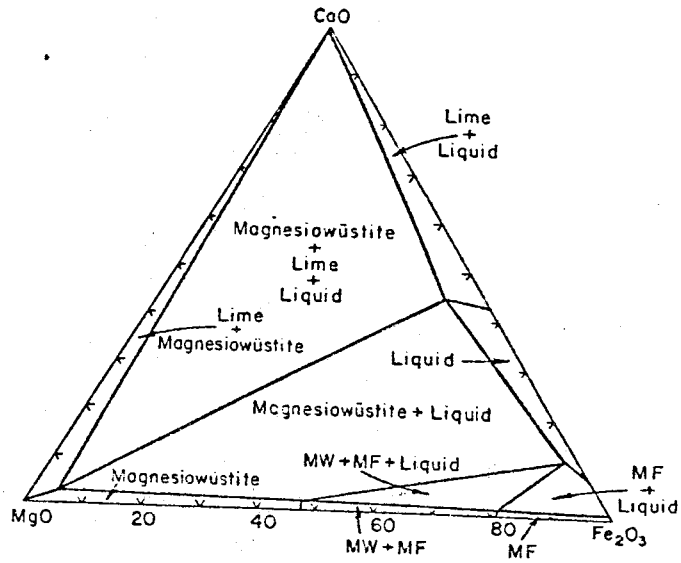

Figure 2-16 System CaO - MgO -"Fe_2O_3" at 1500°C
MW - magnesiowustite
MF - magnesioferrite

(Ref. 85)

Finally the work of Gordon et al. (58), which was very thorough, indicated that the cubic kinetics in fact apply at temperatures above 1300°C with dopant levels of 0.1% and 0.48%. In addition it was found that the growth rate was decreased by increased additions. This is the behavior expected from the theory of impurity atmosphere drag.

Although little or no work has been done on the effects of iron oxide on the grain growth of CaO, the phase diagrams (Figure 2-15) show that at 1438°C liquid would be expected in the CaO-Fe_2O_3 system. However as the Fe_2O_3 would form an equilibrium with FeO at high temperatures some solubility in CaO might be expected (Figure 2-15a).

The ternary diagram (Figure 2-16) indicates that CaO and magnesiowustite would be the only phases present at 1500°C for low Fe_2O_3 contents. However on cooling, magnesioferrite will precipitate.

2.6.4. Titania

The effects of TiO_2 additions on the sintering of MgO have been studied by many authors (19,29,70,71,72,86). The earliest work (86) was on the sintering of Manchurian magnesite, but this work is of little value due to the presence of up to 2% impurities in addition to the TiO_2. Kriek et al.(19) found that 1% TiO_2 produced a marked increase in sintered density at temperatures between 1200°C and 1500°C. However increased additions resulted in progressively less improvement.

Nelson and Cutler (70,71) found that a 1% TiO_2 addition resulted in an increase of theoretical density from 88% to 98% but they failed to observe a decrease with increased additions (Figure 2-19).

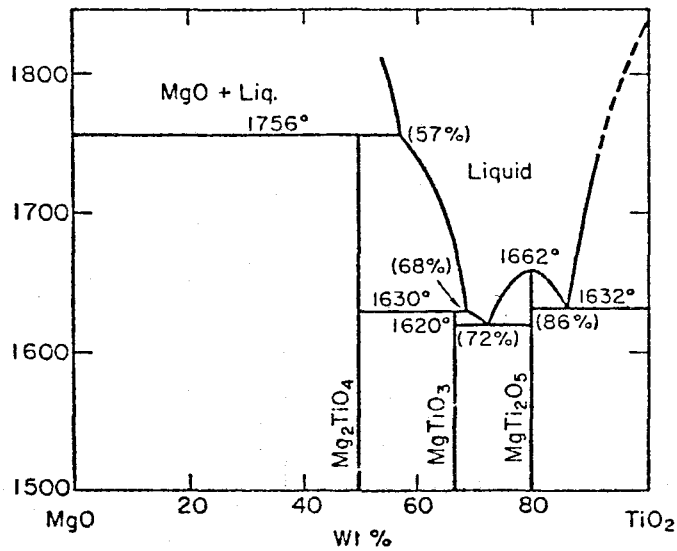

Figure 2-17 $MgO - TiO_2$ Phase Diagram

(Ref. 87)

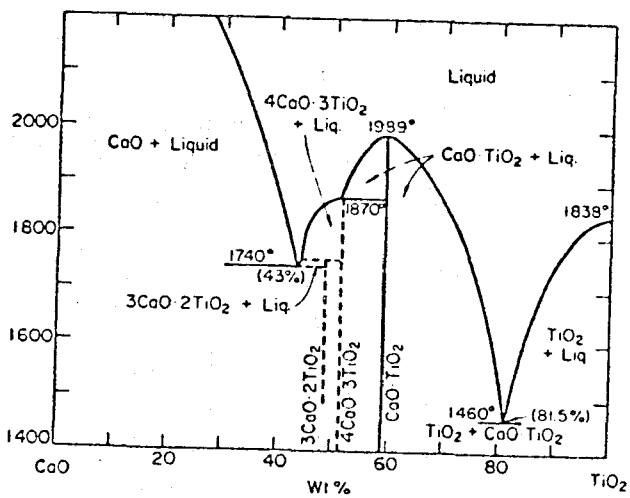

Figure 2-18 $CaO - TiO_2$ Phase Diagram

(Ref. 88)

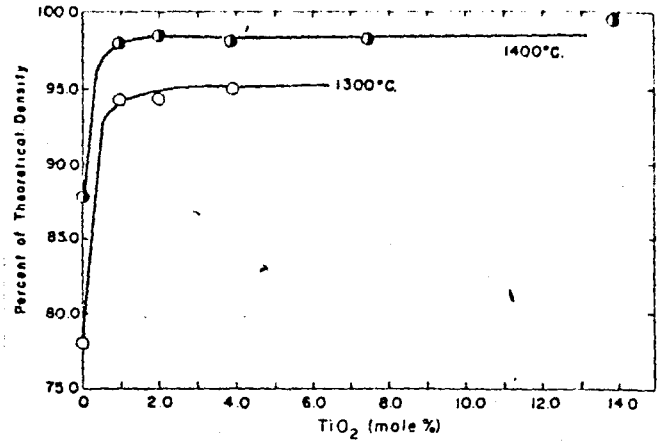

Figure 2-19 Effect of addition of TiO_2 on fired bulk density of Mgo (after Nelson & Cutler (70)).

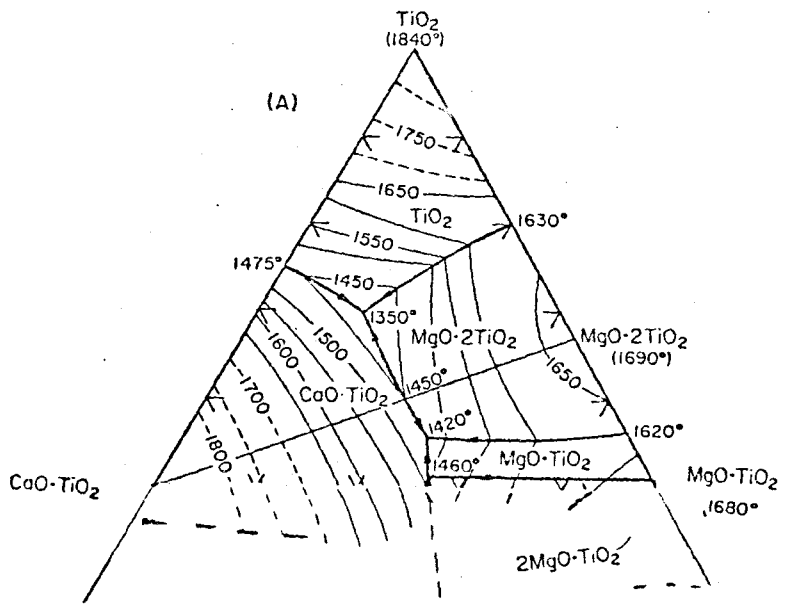

Figure 2-20 MgO - CaO - TiO_2 Phase Diagram

(Ref. 89, 90)

Layden and McQuarie (72) confirmed these results and agreed with the explanation offered by Cutler and Jones (29) that Ti^{+4} ions enter the MgO lattice up to 1 or 2 percent and create vacancies which enhance diffusion.

Kriek et al. (19) found that the 1% TiO_2 addition produced a grain size of 8 μm following five hours at 1500°c which was much larger than that observed for the undoped material (0.03 μm). Nicholson (77) specifically studied the effects of TiO_2 on grain growth and found a rate law proportional to the cube of time.

The phase diagram of MgO-TiO_2, figure 2-17 (87) shows a minimum liquid temperature of 1620°C and three magnesium titanate compounds. With levels of additions used in this study however, no liquid will form below 1756°C.

In the system CaO-TiO_2 (Figure 2-18 (88)) the minimum liquidus is 1460°C but again no liquid would be expected at equibrium below 1740°C. This system also resembles the MgO-TiO_2 system in that a series of calcium titanates form.

2.6.5. Tantalum Oxide

The effects of Ta_2O_5 on the sintering of MgO have apparently been studied by only Layden and McQuarie (72) who concluded, based upon their results at 1225°C, that there was no effect. However their results at 1525°C, which they chose to ignore, indicated that MgO doped with 0.1%, 0.5% and 1.0% mole Ta_2O_5 exhibited increases in density greater than their estimated errors, which is the only criterion

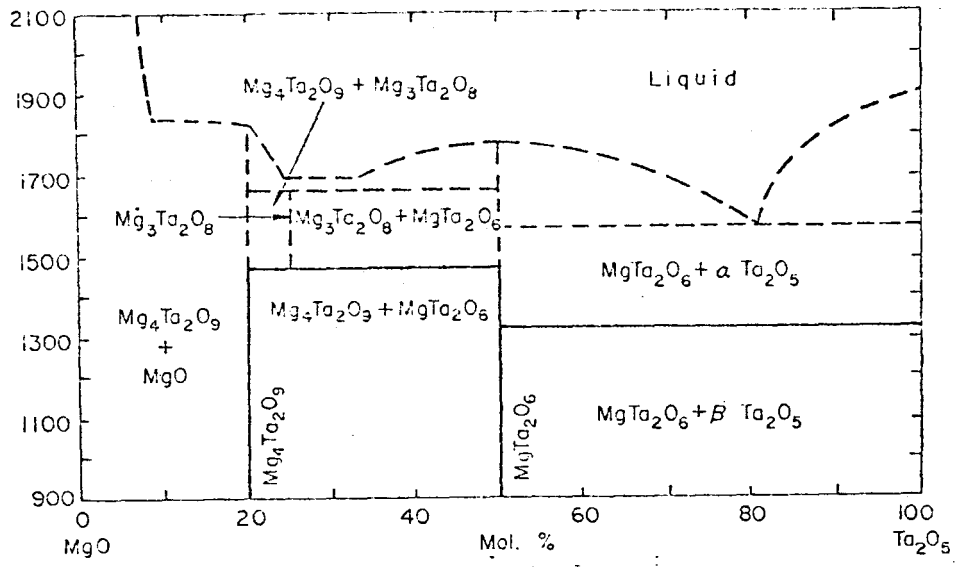

Figure 2-21 $MgO - Ta_2O_5$ Phase Diagram

(Ref. 91)

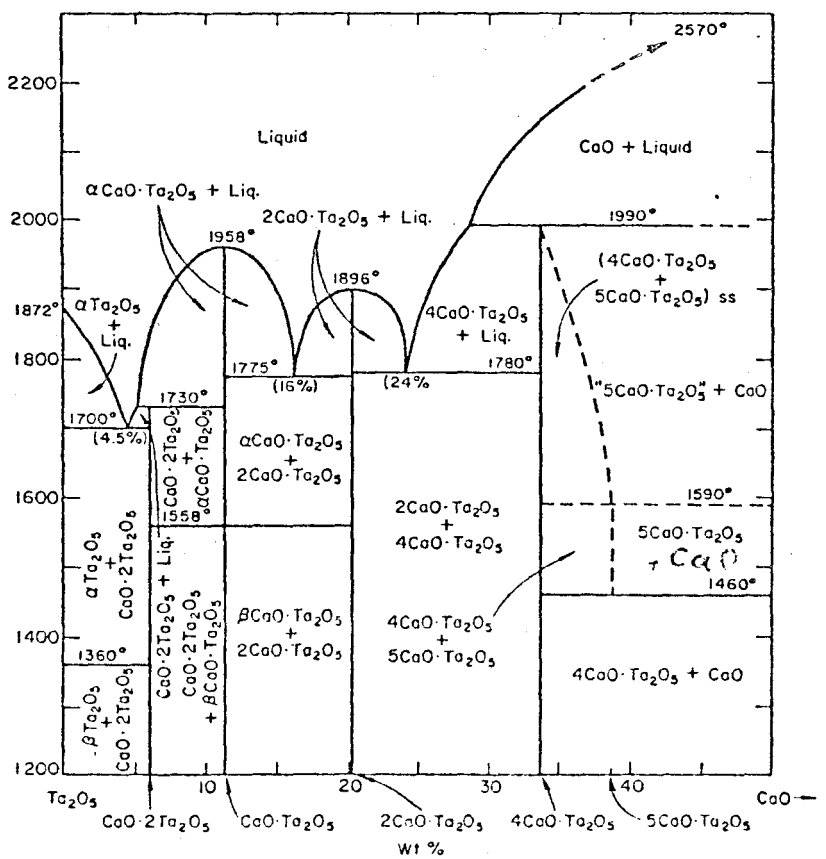

Figure 2-22 $CaO - Ta_2O_5$ Phase Diagram

(Ref. 92)

provided for comparison. Unfortunately little or no work has been done on the effects of Ta_2O_5 on grain growth of either MgO or CaO.

The phase diagram available for MgO-Ta_2O_5 (Figure 2-21) is very sketchy. It indicates that the refractory $Mg_4Ta_2O_9$ phase will form at the low levels of Ta_2O_5 addition used in this work. No liquid will form until 1800°C.

In the CaO-Ta_2O_5 system $5CaO{\cdot}Ta_2O_5$ will form above 1460°C. This decomposes into CaO and liquid at 1900°C. The phase change at 1460°C with the decomposition of the $5CaO{\cdot}Ta_2O_5$ is potentially disruptive. The very refractory compounds formed in both the MgO and CaO systems indicate that grain growth may be enhanced by a getting action as proposed by Burke (33).

2.6.6. Vanadium Pentoxide

Considerable work has been done on this system. Nelson and Cutler (171) found that the presence of 1% - 5% V_2O_5 retarded sintering. This is in sharp contrast to the work of several other authors (93,93, 95,72). Brown (93) in particular found that addition of as little as 0.01% cation vanadium enhanced sintering. This he attributed to solution and defect formation below 1200°C and to liquid formation at contact points above this temperature. Layden and McQuarie (77) confirmed this and reported evidence of excessive liquid formation at 0.1% to 1% levels. The anomalous results of Nelson may have been due to the presence of a reducing atmosphere during firing in a gas + oxygen furnace leading to the formation of the highly refractory V_2O_3 phase (compare Figure 2-23

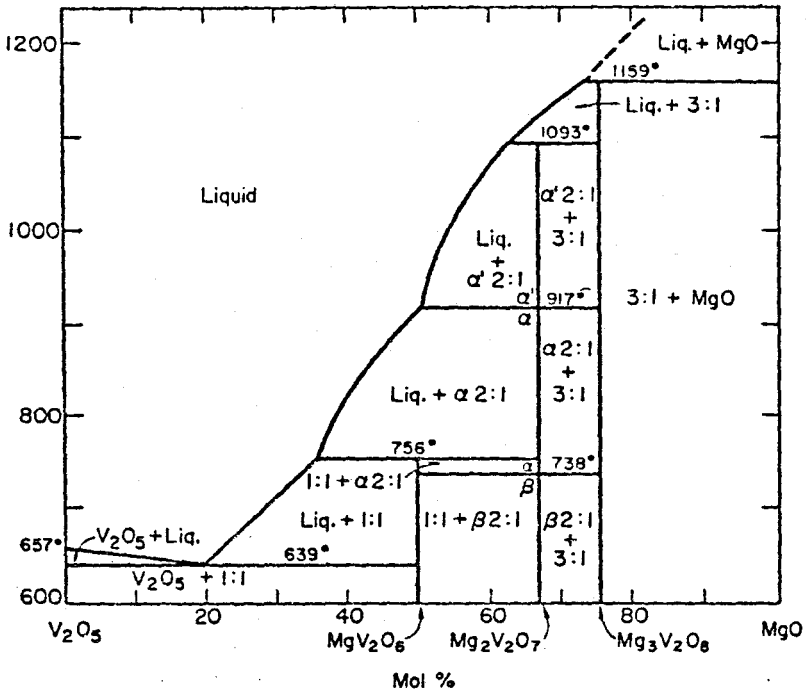

Figure 2-23

V_2O_5-MgO
Phase Diagram
(Ref. 96)

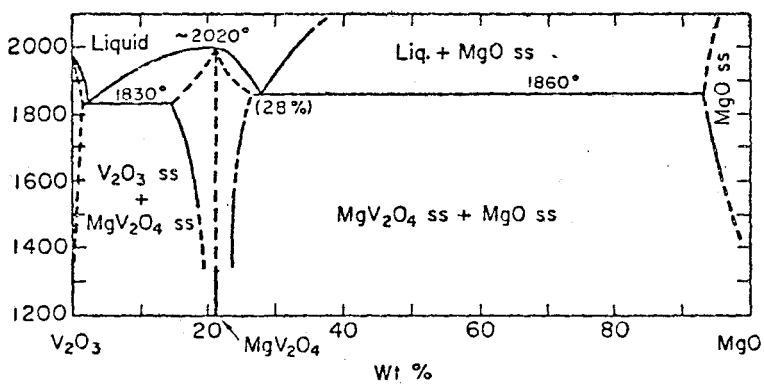

Figure 2-24

V_2O_3-MgO
Phase Diagram
(Ref. 97)

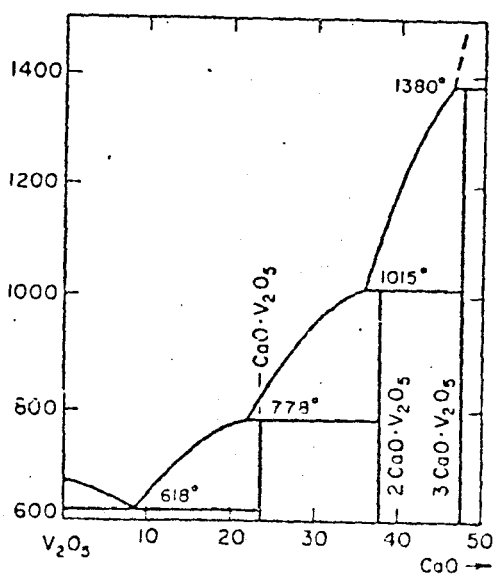

Figure 2-25

V_2O_5-CaO
Phase Diagram
(Ref. 98)

(96) and 2-24 (97)). Layden and McQuaries's observation that previously fired pellets showed no liquid formation when refired to much higher temperatures tends to support this theory. This would be an excellent example of the occurence of behavior such as Tacvorian (66,67,68) proposed, with an addition melting, aiding in densification then forming a highly refractory solid solution or compound with the primary constituent.

Brown (93) also studied the influence of 0.1% V_2O_5 on grain growth and detected cubic kinetics between 1250°C and 1450°C. This would indicate the presence of a liquid phase. Nicholson (93a) confirmed these results in detail for 0.1% to 2.0% vanadium showing cubic grain growth kinetics at temperatures between 1300°C and 1500°C for times up to 100 hours.

2.6.7. Tungsten Oxide

Layden and McQuarie (72) have been the only investigators of the MgO - WO_3 system and concluded that WO_3 was not effective as a sintering aid. In addition, in Figure 2-26 (99), it can be seen that there is a potentially disruptive transformation at 1165°C. In spite of this it was determined to proceed with preliminary experiments in view of the liquid formation in the MgO - WO_3 system at 1318°C while in the CaO - WO_3 system no liquid is expected until 2250°C as shown in Figure 2- 27 (99). This system therefore offers the possibility for the behavior predicted by Tacvorian.

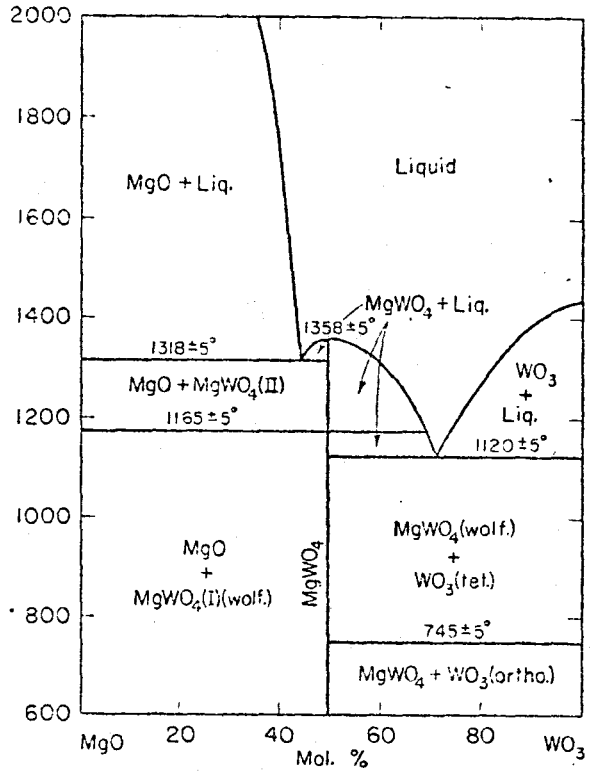

Figure 2-26

$MgO - WO_3$ Phase equibrium

(Ref. 99)

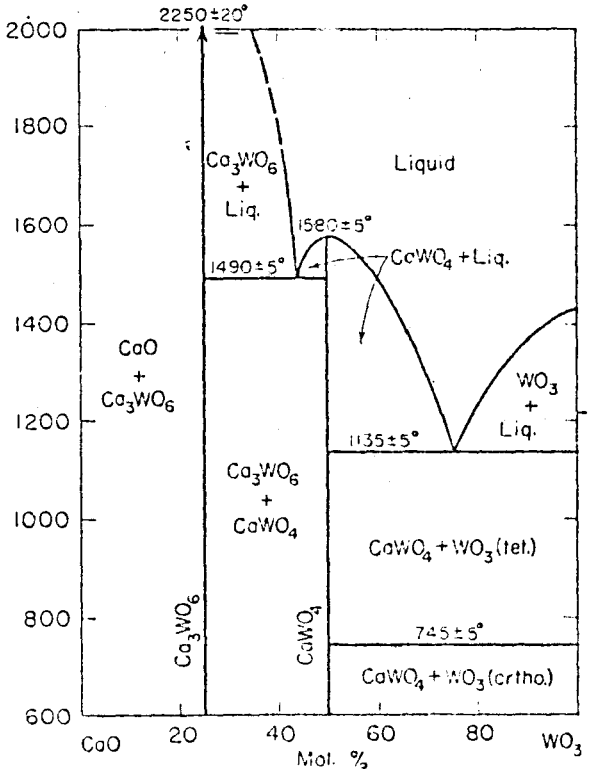

Figure 2-27

$CaO - WO_3$ Phase equibrium

(Ref. 99b)

2.6.8. Germanium Oxide

There has apparently been little or no work done on the influence of GeO_2 on the sintering behavior of MgO or CaO. However in view of its chemical similarity to SiO_2 and possible refractory compound formation, preliminary experiments were done. The phase diagrams for this system are presented in Figures 2-28 to 2-30 (100, 101,102), and indicate that if localized, non equilibrium concentrations pertain, liquids could be expected at temperatures as low as 1100°C. However as equilibrium is approached a series of germanate compounds would form in both CaO and MgO so that no liquid would be present until temperatures in excess of 1800°C.

2.6.9. Effect of Calcia on MgO

Many authors (19,70,71,72) have studied the effects of small additions of CaO on the sintering of MgO. Nelson and Cutler (70,71) with 1% - 8% additions found only a slight increase in sintering as shown in Figure 2-31, while McQuarie (72) found no effect with less than 1%. Kriek et al (19) did a more extensive investigation which has been discussed in Section 2.3.3. and concluded that sintering is inhibited at points of contact between lime and magnesia possibly by limited diffusion. The fact that a second phase inhibits grain growth has been demonstrated by many authors (14,43,103) and is in accord with theoretical considerations discussed previously.

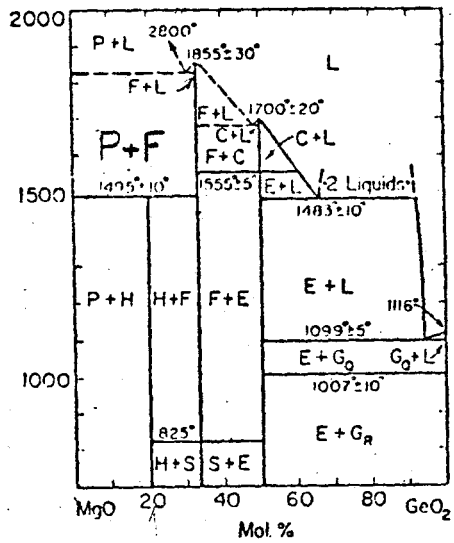

Symbol	Composition
C	$MgO \cdot GeO_2$
E	$MgO \cdot GeO_2$
F	$2MgO \cdot GeO_2$
G_Q	GeO_2
G_R	GeO_2
H	$4MgO \cdot GeO_2$
L	
P	MgO
S	$2MgO \cdot GeO_2$

Figure 2-28 $MgO - GeO_2$ Phase Diagram

(Ref. 100)

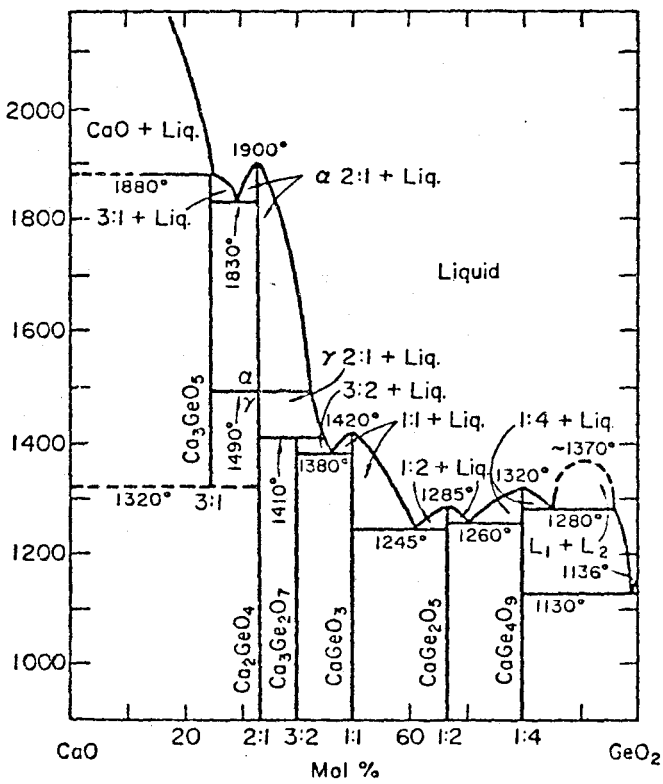

Figure 2-29 $CaO - GeO_2$ Phase Diagram
(Ref. 101)

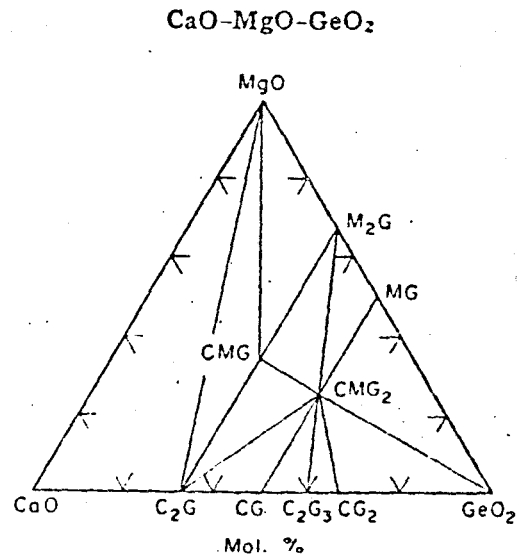

Figure 2-30 $CaO - MgO - GeO_2$ Phase Diagram
(Ref. 102)

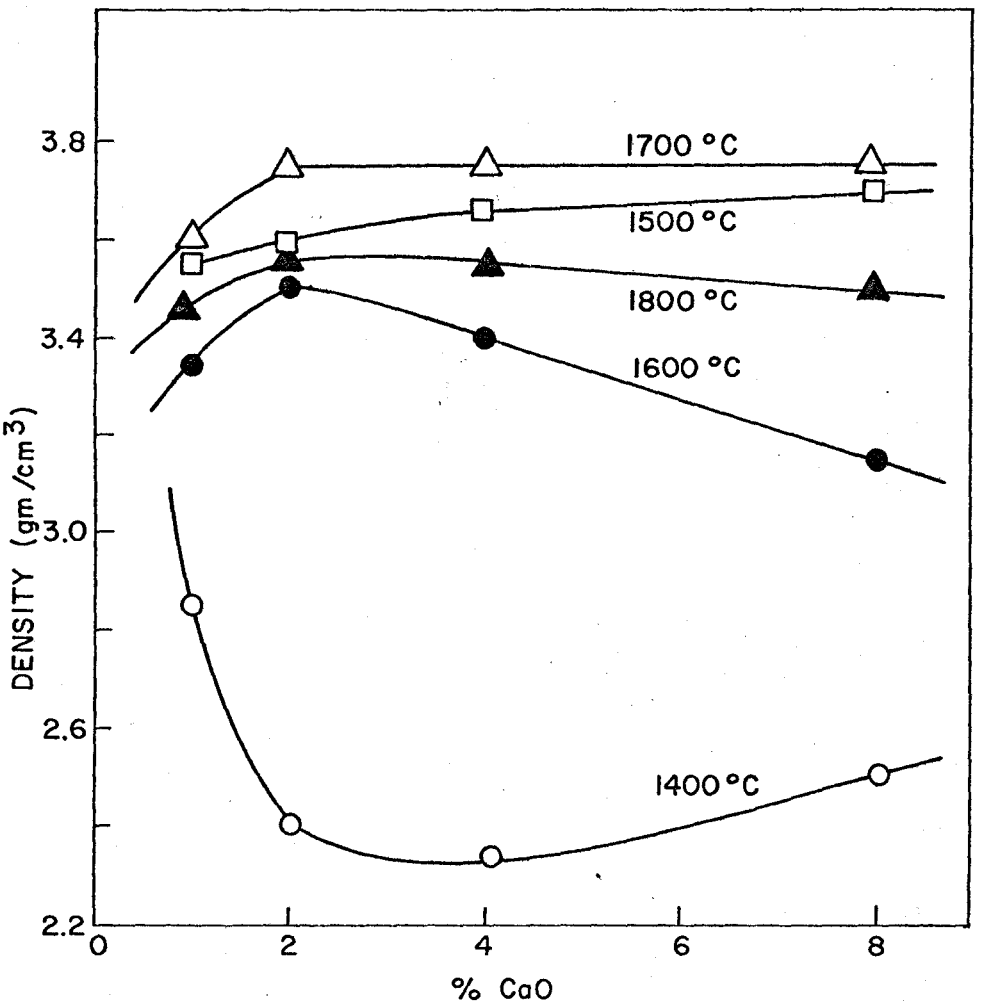

Figure 2-31 Effects of low levels of CaO on sintering of MgO (results of Nelson and Cutler (70)).

2.6.10. Other Systems

Numerous authors have published work on a variety of other oxide and non-oxide additions and their effects on the sintering of MgO. There is also one paper on the effect of strontium oxide on the sintering of CaO. Since some of these additives look promising for future work, the more important results will be outlined here.

The most comprehensive and most in exact study was that of Nelson and Cutler (70,71), who found that additions of 1% to 8% Al_2O_3 to MgO retarded sintering up to 1400°C yet enhanced it at 1600°C. Layden (72) however, found that 0.1% and 0.5% Al_2O_3 did not retard sintering although 1% did. Both authors attributed this to spinel formation .

With the exception of Jones (29), several authors agree (70,72,104), that ZrO_2 aids sintering, probably by a vacancy defect structure. Budnikov (105) also found that additions of 0.025% to 0.3% HfO_2 enhanced both sintering and grain growth in MgO. This could potentially be useful due to the refractory nature of the MgO-CaO-HfO_2 system (106).

Cr_2O_3 has universally been found to inhibit sintering (22,29, 70,71,72). Hench and Russel (22) in a thorough study attributed this effect to the formation of spinel coatings on the MgO by reaction with volatile CrO_3 vapour.

Nelson and McQuarie agree with Atlas (107) and others (108,109) that Li_2O aids sintering by a liquid phase mechanism whilst Na_2O hinders

Table 2- 2

Oxide Additive	Nelson & Cutler (24,25)	Layden McQuarie (26)	Others (Ref.)
LiO	E	N 1525°C E 1225°C	E (107, 109)
Na_2O	X	X	
K_2O	X		
CaO	Y, X	X 1525°C	X (19)
SrO	X		N (153) D (153)
BaO	X	X 1525°C	
TiO_2	E	E	E (31, 19) G (19, 153, 77) D (153) T
ZrO_2	E	E	E (31, 104) <1%S (153) >1%D (153)
HfO_2			E G (105)
Ta_2O_5		E 1525°C	T
Cr_2O_3	X	X	X (22) D (153)
MoO	X		
WO_3		N 1525°C X 1225°C	T
Mn_2O	E	E 1225°C	
Fe_2O_3	<5%E >5%X	E 1225°C	E (31, 19, 153) G (19, 77, 78, 79, 153) D (153) T
V_2O_5	X	E	E (77, 94, 95) G (77) T
CoO	N		

Table 2-2 Continued

Oxide Additive	Nelson & Cutler (24,25)	Layden McQuarie (26)	Others (Ref.)
NiO	N		
Ca_2O	N		
ZnO	E<1400°C		
GeO_2			T
SiO_2	E	E 1225°C	E G (19) T
Al_2O_3	X	E 1225°C	E (19, 153) >1%D (153)
PbO	X		
CdO	X		
SnO_2	X		

Key

E	Effective sintering aid
G	Effective Grain Growth Promoter
X	Hinder sintering
T	This work
Y	Hinder Grain Growth
N	No effect detected
S	Increased strength of MgO
D	Reduced strength

sintering due to its volatibility. Nelson and Cutler also investigated a number of heavy metal oxides and found none to be effective sintering agents.

In summary it would appear that lithium compounds, ZrO_2, HfO_2, Mn_2O, and ZnO, in addition to those discussed in detail in the previous sections may prove effective sintering additives for MgO and doloma.

Naknamura (153) investigated a number of additives and their effect upon the strength of MgO and found that <1000 PPM ZrO_2 increased the strength while Fe_2O_3, SrO, TiO_2, and Cr_2O_3 decreased it. Al_2O_3 had no effect below 1000 PPM.

All of the results reviewed are summarized in Table 2-2.

2.7. Mechanical Properties

2.7.1. Conventional Tests

Many tests of the mechanical and physical properties of materials are used to help predict service perfomance. These measurements are usually based on some load bearing measurement. These tests include compression or crushing tension, torsion and flexure. Unfortunately the temperatures and loads for these tests have often been chosen to provide convenient testing rates and conditions rather than to simulate actual service conditions (110). These tests, involving arbitrary incremental changes in loading and temperatures do not provide any absolute data and no ready comparison can be made between different tests (111).

More recently the breaking strength or "modulus of rupture" at elevated temperatures has been extensively use, however this test also has drawbacks. Due to the large numbers of flaws inherent in these materials the modulus of rupture values are highly variable.

Since fracture energy and flaw shape and size are fundamental in determining the strength of refractories and, in view of the recent applications of fracture toughness measurement to ceramics, it seemed logical to study the fracture toughness behavior of the MgO - CaO system as a function of the microstructures produced.

2.7.2. The Flaw of Theory of Fracture

It has now been accepted that the relatively low strength of engineering ceramics is due to the presence of cracks or microinhomogenieties Cracks cause high stress concentration in the regions near their tips, leading to rapid crack growth and failure. Thus the strength of a brittle material is determined as much be the nature of the flaw within it as by its intrinsic properties. This has in the past been recognized as statistical size effects (118) and attendent development of distributions such as that of Weibull (119) to determine the fracture strength of a material have resulted. More recently fracture mechanics has been applied to ceramic materials and a number of tests using controlled artifical flaws have been introduced to develop a more direct understanding of the fracture behavior of these materials.

It has long been established that the stress at the tip of a sharp crack is given by:

$$\sigma = 2\sigma_{app}\,(a/p)^{\frac{1}{2}} \qquad (2\text{-}6)$$

where σ is the local stress

σ_{app} is the applied stress

a is ½ of the crack length

p is the radius of curvature of the crack tip.

Griffith proposed as a condition of fracture that the strain energy release rate (du/da) must be equal to or greater than the rate of increase in energy due to the creation of new surfaces (dw/da) ie.

$$\frac{du}{da} \geq \frac{dw}{da} \qquad (2\text{-}7)$$

The decrease in stored elastic strain energy U on crack extension is given by:

$$U = \frac{-\pi \sigma_{app}^2\, a^2\, (1 - v^2)}{E} \qquad (2\text{-}8)$$

where v is Poisson's Ratio

E is Young's Modulus,

and the increase in energy due to new surface formation is $4a\gamma_s$ where γ_s is the surface energy.

Substituting these terms into equation 2-7, an expression for the fracture stress σ_f results,

$$\sigma_f = [2E\gamma_s/\pi(1-v^2)a]^{\frac{1}{2}} \qquad (2\text{-}9)$$

In general, the surface energy calculated from fracture studies is much different than thermodynamic surface energy γ_s so the effective surface energy is substituted for γ_s. This is discussed in more detail later in this section.

The stress field at any point at the tip of a crack may be related to its distance from the crack tip, its angle of inclination to the crack plane and a constant K called the stress intensity factor (122).

If the plane strain condition applies at the crack tip the stress field equations can be solved to the form :

$$K_I = Y \sigma_f a^{\frac{1}{2}} \qquad (2\text{-}10)$$

where Y is a dimensionless constant for a given test geometry

K_I is the stress intensity factor for mode 1 fracture (simple tension).

When a critical stress level is reached fracture will occur and the critical stress intensity factor at that point is denoted K_{1C}. This concept of a critical stress intensity for a given flaw size is the basis of modern fracture mechanics.

The effective surface energy γ_I and the stress intensity factor are closely related and it can be shown that :

$$K_{1C}^2 = 2E\gamma_I/(1-\nu^2) \qquad (2\text{-}11)$$

This relation is very important since both γ_I and E have previously been shown to be sensitive functions of the material microstructure (124).

Using the alternative approach of energy balance, a material parameter G_{1C} called the critical strain energy release rate for mode 1 fracture may be defined. G_{1C} is a measure of the energy required to increase the crack length and is related to the effective surface energy γ_I by the following equation:

$$G_{1C} = 2\gamma_I \qquad (2\text{-}12)$$

Substituting this relation into equation 2-11 it is found that:

$$K_{1C}^2 = E\, G_{1C}/(1-\nu^2) \qquad (2\text{-}13)$$

From this latter result it is apparent that the fracture toughness and the more fundamental material property G_{1C} are closely related. Throughout the balance of this work K_{1C} values will be quoted.

2.7.3. Effect of Porosity on Young's Modulus

Knudsen observed a dependence of Young's modulus for Al_2O_3 with up to 20% porosity. This behavior may be represented by the following equation:

$$E = E_0 \exp[-3.95\, P] \qquad (2\text{-}14)$$

where E is the observed Young's modulus

E_0 is the Young's modulus of fully dense material

P is the volume fraction of porosity.

Hasselman and Fulrath (117) showed that this is in good agreement with the effect predicted for cylindrical porosity.

This result is also in good agreement with the observed relation between bend strength and porosity in polycrystaline alumina reported by Bailey and Hill (148).

This effect of porosity upon E will directly affect the K_{1C} values since K_{1C} is directly proportional to the square root of E shown by equation 2-11.

It can be seen from the calculations in Table 2-3 that the effect of porosity on Youngs modulus accounts for a substantial fraction of the variation in toughness between samples of varying porosity. It must be noted that variations do exist between the corrected values and this must be attributed to effects of grain size and porosity on the effective surface energy γ_I.

2.7.4. The Components of Effective Surface Energy

The effective fracture surface energy (γ_I) can be resolved into several components:

1. Thermodynamic surface energy (γ_o).
2. Grain boundary surface energy.
3. Energy due to plastic flow at the crack tip.
4. Energy to form secondary cracks.
5. Other processes causing crack blunting.
6. Effects of the environment.
7. Presence of a second phase.
8. Miscellaneous processes irreversibly absorbing energy

Table 2-3

The Effect of Application of a correction due to the effect of Porosity on Youngs Modulus to K_{1C} values of several Aluminas (Data from Ref. 139).

Density g/cm^3	Grain Size μm	K_{1C} $MN/m^{3/2}$	K_{1C} "Corrected"
2.58 X	2	0.65	2.5
2.73 X	2	0.93	3.0
3.32 X	5	2.8	5.0
2.65	11	3.2	4.1
3.68	7	3.4	4.2
3.78	6	3.6	4.1
3.82	5-20	4.5	4.9
3.83	5	4.3 - 4.5	4.6 - 4.8
3.85	20	4.0	4.2
3.87	12	4.0	4.1
3.80	18	3.7	4.1

X No silica content otherwise 3%.

at the crack tip such as noise and heat.

The thermodynamic surface energy is that energy associated with the fracture of bonds within a crystal and is much lower than the observed values of γ_I. In a ceramic, a mixture of transgranular and intergranular fracture often occurs. The energy required for the fracture of the grain boundary is different than γ_o and the proportion of each type of fracture will influence the γ_I value. The proportion of intergranular fracture is often influenced by the grain size. Large grains are more often observed to fracture transgranularly, however the effects of grain size are amibiguous. Evans (159) points out that results have been obtained showing K_{1C} to increase, decrease and be independent of the grain size. Increases of the proportion of transgranular fracture seems to increase K_{1C} as does reduction of grain size if intergranular fracture predominates.

For MgO, Evans, Gilling and Davidge (157) found that γ_I depended upon crack length only for cracks greater than 10 grain diameters. This is in contrast to the results obtained in Al_2O_3 and UO_2 where γ_I was found to be independent of crack length. These findings were true for both porous and non porous materials prepared by hot pressing and sintering. It is necessary therefore to ensure uniform notch configurations in the testing of MgO.

These authors also noted that γ_I for a 15% porous sintered material (grain size 20 μm) showed no temperature dependence of γ_I (Figure 2-32). This appears to be true only for very pure materials

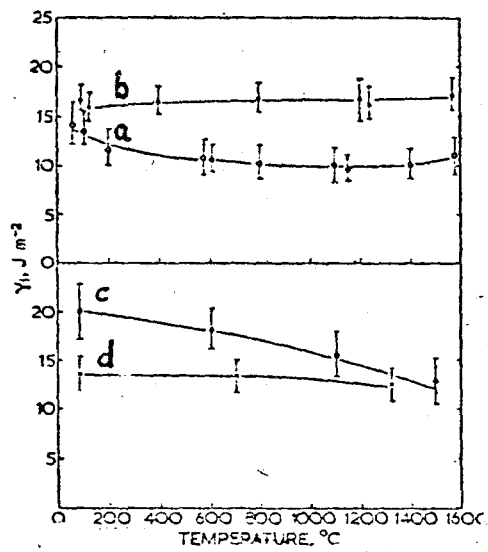

Figure 2-32 Temperature dependence of γ_I for MgO

a) Grain size 25 μm fully dense
b) Grain size 150 μm fully dense
c) Porous - Hot Pressed
d) Porous - Cold Pressed

(after Gillings et al (157)).

as discussed later in Section 2.9.3.

Secondary cracks may occur in the form of crack branching or as microcracks in advance of the crack tip (Figure 2-33). The formation of such a microcrack zone can have an effect similar to that of a plastic zone as previously discussed by Green (121) and Evans et al (161). The presence of microcracks at the crack tip has been confirmed in both dense and porous MgO above 1000°C by Evans et al (157). The possibility of grain boundary cracking is enhanced by the presence of a second phase of differing coefficient of thermal expansion. Large stress would be expected in this case which Green (158) showed to be important in his work in partially stabilized zirconia.

Evans et al (161) cite unpublished work by Clausen et al on the design of ZrO_2 - Al_2O_3 systems exhibiting controlled microcracking due to non isotropic behavior of these oxides. These materials are said to possess good strength and toughness although it was noted that an excessive formation of microcracks could produce a tough material with low strength.

Such microcracking is possible in the doloma systems studied here but since both MgO and CaO possess the isotropic NaCl crystal structure and in view of the smaller differences observed in the coefficient of thermal expansion of these phases (Table 3-4), it is unlikely to be important.

Effects on conditions at the crack tip must also be expected

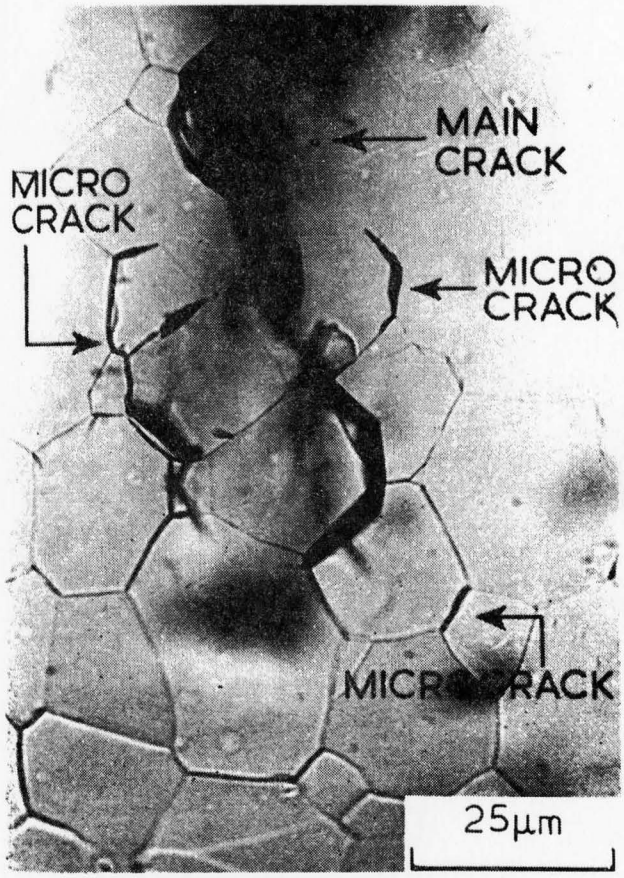

Figure 2-33 Microcracks ahead of a pre-existing crack at 90% of fracture load.
(after Evans (161))

Table 2-4

Table of Thermal Expansion Data (154)

	Coefficient of Thermal Expansion $\alpha \times 10^6$ °K $^{-1}$	Temperature (°K)
CaO	13.7	273 - 1673
MgO	14.0	293 - 1673
Al_2O_3 a axis	7.1	373
	9.7	773
	14.2	1273
	6.0	373
c axis	8.9	773
	13.8	1273
ZrO_2 (average)	5. - 5.6	273 - 1673

when the crack intersects a second phase. Porosity is a very common second phase found in nearly all sintered ceramics. Evans (159) states that coarse intergranular porosity has only a very small effect on K_{1C}. This is in considerable doubt in view of the previous discussion of the effect of the porosity on Youngs Modulus.

The results of Coppola and Bradt (160) are unusual in that their work to fracture studies indicated no effect of porosity on Al_2O_3. This they attributed to the interaction between pores and the crack tip being of the same magnitude as the effect of porosity reducing the total fracture area. This indicates that there is a very large potential effect of porosity upon γ_I.

Pores, like brittle second phase precipitate particles, have been shown by Green (121) to result in bowing of the crack front resulting in limited increases in toughness.

Evans (161) notes that if the second phase encountered by the crack tip is ductile, plastic or viscous deformation of the particle could result in ligament formation across the crack which would increase the toughness. The blunting of a crack by a pore or ductile particle would also contribute to toughening due to the necessity of re-initiating the crack beyon the inclusion.

Another toughening mechanism proposed for silicon nitride (142) involves the pull out of particles coated with a viscous liquid. The possible magnitude of toughening due to this effect is unknown however.

It is apparent that a large number of factors may influence

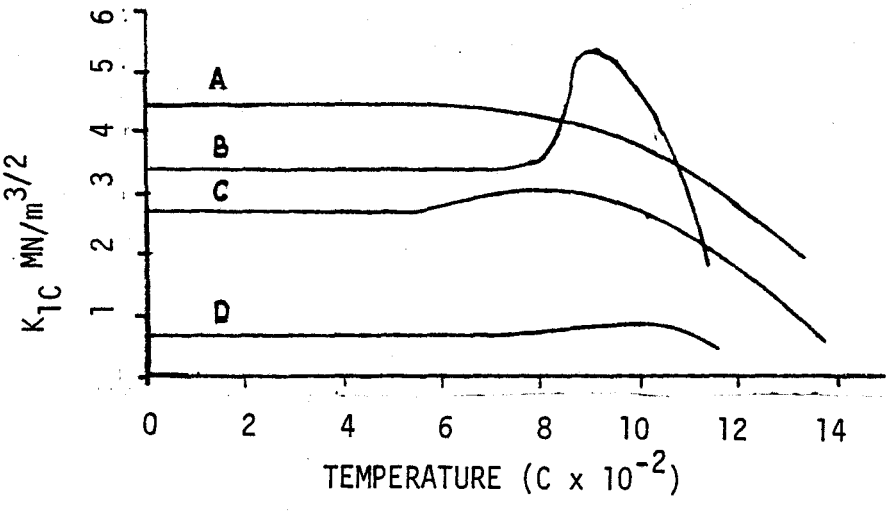

Figure 2-34 Temperature dependence of K_{1C} for different aluminas

A - 98% Dense

B - 93% Dense 3% SiO_2

C - 85% Dense

D - 66% Dense

(After Claussen et al (139)).

K_{1C} through γ_I and that only with great difficulty may the effects be separated.

2.7.5. The Effects of Temperature on K_{1C}

It has been well established that any glassy phase in a refractory material will play an important role in determining its strength at high temperature (139 to 142).

Evans and Wiederhorn (139) studied the effects of temperatures upon the K_{1C} of a number of polycrystaline aluminas. These results, shown in Figure 2-34, indicate the possibility of three types of behavior:

1. A uniform and gradual reduction in toughness with increasing temperature.
2. A slight increase in toughness at an intermediate temperature followed by gradual decrease.
3. A marked increase in toughness followed by a rapid loss of strength.

The first type of behavior is typical of a pure material while the second type of behavior found in relatively low density material was attributed to healing effects at cracks and pores leading to a decrease in stress concentration. This interpretation is supported by Simpson and Merrett (147) who studied crack healing in polycrystaline Al_2O_3 during annealing.

Davage and Tapin (140), Rice (145), and Evans (146), have

also found similar effects on the modulus of rupture of Al_2O_3. The behavior seen in Figure 2-30b was attributed to the presence of a glassy phase which was brittle at low temperatures but became less and less viscous above 700°C so that energy could be dissipated by viscous deformation of this phase. Similar behavior has been reported in silicon nitride (142) with a maximum in toughness near 1400°c and in fusion cast refractories by Chan et al (141) with a maximum occurring at 600°c. Load-deflection and fracture-temperature curves obtained by Davidge (140) are shown in Figures 2-35 and 2-36 and support this interpretation. A significant feature of Davidge and Tapins (140) work on alumina is that a 100 fold change in the strain rates used resulted in only a small change in the temperature of the peak toughness value. This indicates that the significant features of the temperature dependence of K_{1C} can be accurately positioned with simple rapid tests.

From these results it can be seen that the fracture toughness test can be a sensitive tool to determine the effect and the nature of the action of additives on the high temperature mechanical properties of refractories.

2.7.6. Plasticity in MgO and CaO

The fact that MgO and CaO are both NaCl structures which are "semi-brittle", indicates that the possible transition to plastic deformation and failure mechanisms from completely brittle fracture

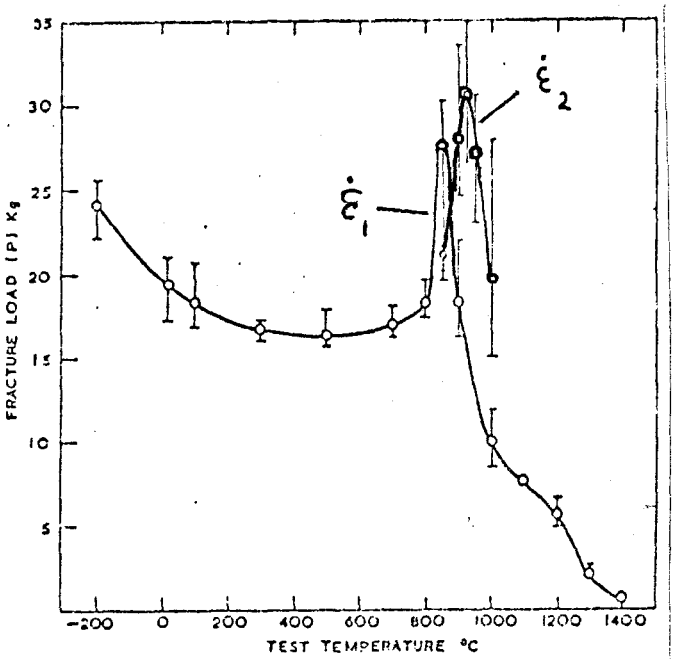

Figure 2-35 Temperature dependance of fracture load for notched bars of impure Al_2O_3 $\dot{\Sigma}_2 = 100\ \dot{\Sigma}$, (after Davadge and Tappin (140)).

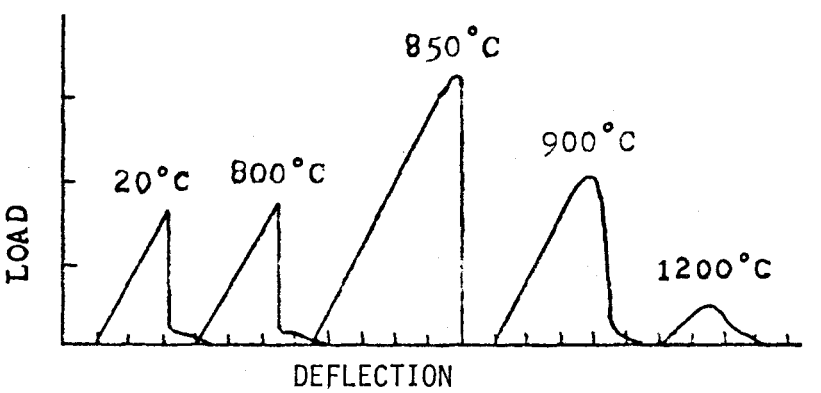

Figure 2-36 Load - deflection curves for impure Al_2O_3 (after Davadge and Tappin (140)).

must be considered.

Evans (159) reports that tensile tests of high purity recrystalized MgO show that this ductile brittle transition occurs at approximately 1700°c (Figure 2-37) and at approximately 1100°C in compression (Figure 2-38). Copley and Pask (114) report for two MgO's containing impurities of unknown nature, that the transition was observed as low as 800°C. Rice (145) also identified possible plastic deformation behavior in his MgO at temperatures above 1300°C. However in a rare study of CaO modulus of rupture he found no evidence of plastic flow even at 1400°C. In magdol compositions the absence of flow in the CaO phase should prevent accomodation of flow by the MgO phase so that it is unlikely that plastic flow will affect γ_I significantly below 1400°C.

2.8. Determination of K_{1C}

2.8.1. Techniques for the Measurement of K_{1C}

There are a wide range of specimen geometrics available for fracture mechanics measurements. All of these specimens must satisfy a thickness (b) constraint in order to ensure accurate experimental results:

$$b > 2.5\ (K_{1C}/\sigma_y)^2 \qquad (2\text{-}15)$$

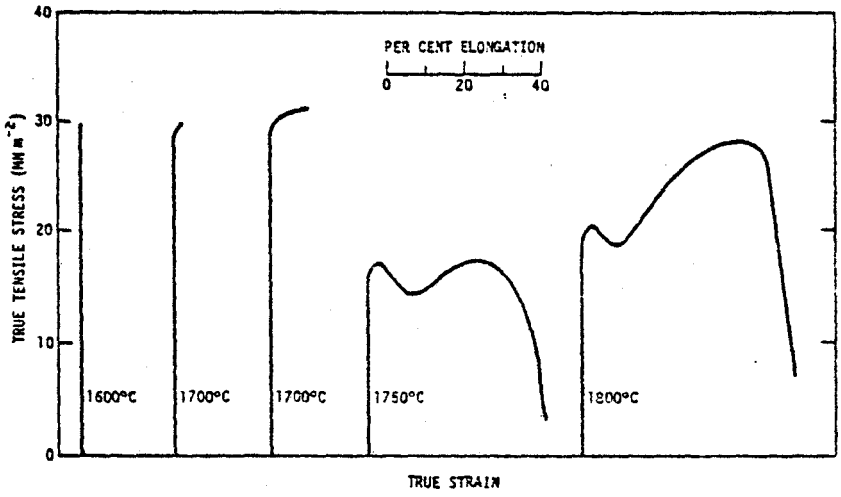

Figure 2-37 Tensile stress strain curves for polycrystaline MgO test at a strain rate of 5×10^{-4} s^{-1} (after Evans (161)).

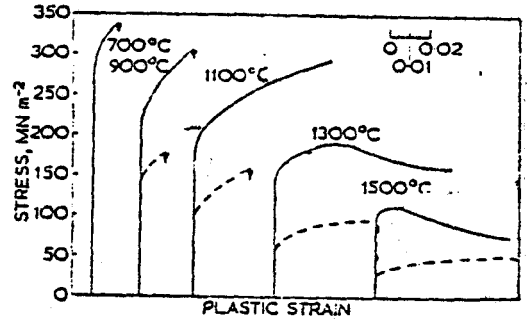

Figure 2-38 Compressive stress strain curves for MgO
——— porous hot pressed
-------- porous cold pressed
(after Evans et al (157)).

Since in a brittle ceramic material the ratio of $K_{1C}/\sqrt{\sigma_y}$ is generally very small this condition is always met. The most common specimens utilized are the notched-beam bend, the double torson beam and double cantilever beam. The latter test is the most accurate since it is practical to initiate a precrack thus ensuring a crack tip.

However this specimen requires considerable material and careful alignment. The notched beam sample in 4 point bending requires less material, is easier to prepare and has been shown by Pabst (160) and other authors (147) to provide accurate estimates of K_{1C} without precracking. These specimens have the added advantage of being easily handled by high temperature test rigs. Accordingly the four point bend geometry was selected in view of the large numbers of samples to be tested and particularly the fact that only a comparison of K_{1C} is desired. This means that fairly large systematic errors can be tolerated.

Errors inherent in the 4 point bend test are due to errors of alignment and friction at the support points. Alignment is considerably less important with the 4 point bend specimens since pure bending exists between the inner knife edges. Such errors may be minimized by ensuring that the ratio of inner to outer spans is greater than 2:1 as pointed out by Brown and Scrawley (143).

Using the load required to cause catastopic failure of the 4 point bend specimens ,the crack dimensions and specimen dimensions,

the K_{1C} value may be calculated from equation 2-16:

$$K_{1C} = 2.964 \times 10^{-2} \, YPK(a)^{\frac{1}{2}}/BW^2 \qquad (2\text{-}16)$$

where K_{1C} has the units of $MN/m^{3/2}$.

Y is the boundary calibration (143).

P is the load in Kg.

K is the distance between the inner and outer knife edges.

a is the notch depth.

B is the depth of the specimen in cm.

W is the width of the specimen in cm.

Further details of the origins of the numerical constant are presented in Appendix I. The 4 point bend specimen and the equation for "Y", the boundary calibration factor, are presented in Figure 2-39.

2.8.2. Use of a Diamond Sawcut to Simulate a Sharp Crack

In the elastic analysis of a fracture specimen is the implicit assumption that the notch has zero volume or zero width. However creation of a sharp crack in a small ceramic specimen is difficult and, in opaque ceramics, difficult to measure. Several workers have shown that the production of a notch with a diamond blade is an adequate way of simulating a sharp notch. Pabst (126) and Davidge (127) have both shown this to be adequate to produce results within 10% of results obtained from zero volume cracks in double cantilever beam specimens,

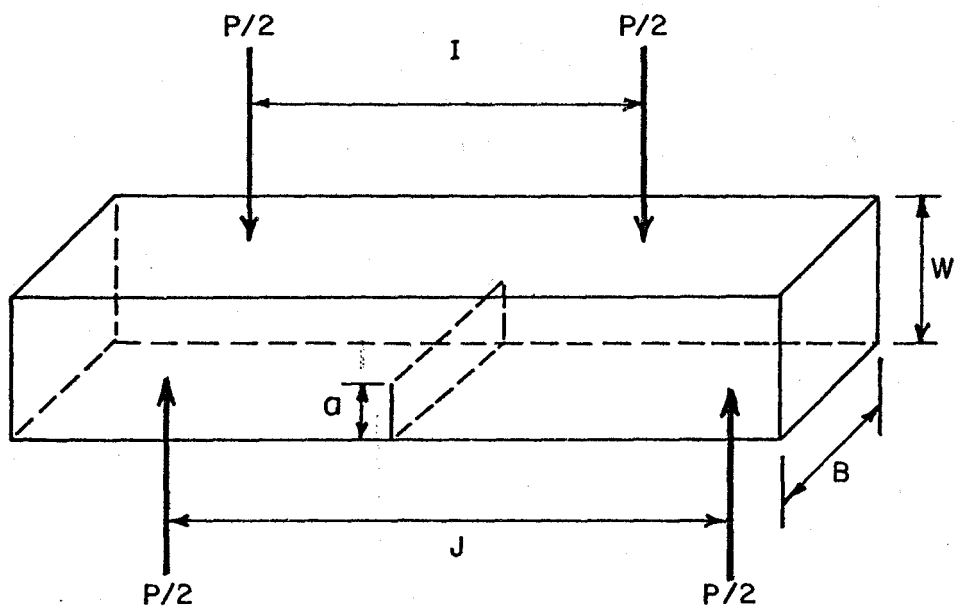

$$K_{1C} = Y \frac{3Pgka^{\frac{1}{2}}}{BW^2}$$

where $Y = 1.99 - 2.47(a/W) + 12.97(a/W)^2 - 23.17(a/W)^3 + 24.80(a/W)^4$

P is the fracture load
g is gravitational constant
k = (J-I)/2
a is notch depth

Figure 2-39 Four point bend fracture toughness specimen and K calibration equation.

provided (128) that the ratio of the crack length to the tip radius is >0.3. Thus a 0.1 mm saw width is adequate if the notch is more than 0.5 mm deep.

The reason for the successful simulation of a sharp crack with a diamond saw has universally been attributed to the creation of an array of microcracks and pullouts in the notch which are effectively a sharp plane crack front.

CHAPTER 3

EXPERIMENTAL AND PRELIMINARY RESULTS

3.1. Raw Materials

3.1.1. Chemical Analysis

In order to avoid problems with the masking of the effects of the experimental additives by native impurities, the purest $MgCO_3$ and $CaCO_3$ commercially available were chosen as raw materials.

The carbonates chosen for the source of CaO and MgO were Baker $CaCO_3 \cdot nH_2O$ (low in alkali) and Baker $MgCO_3 \cdot nH_2O$. The analysis quoted by the manufacturer was relatively incomplete so a number of other elements were analysed for by Martin van Oosten and Baringer Research Limited. The proposed additives were also analysed. In addition an analysis was done upon calcined MgO to detect any pick up of impurities. The results of all these tests are listed in Table 3-1. It can be seen that the level of boron is low in both materials which is particularly important in view of its extremely deleterious effects upon the high temperature strength of refractory bricks (60).

The only significant impurity detected was approximately 0.25% Na in the MgO. Nelson and Cutler showed that Na_2O hindered the sintering of MgO attributing this effect to the volatility of Na_2O and its ability to completely coat the MgO grains. The Na_2O sublimes at 1175°C and analysis following firing to 1700°C for five hours showed

Table 3-1 Chemical Analysis of Raw Materials

	$MgCO_3 \cdot nH_2O$ (Baker) ①	$MgCO_3 \cdot nH_2O$ (Baker) ②	MgO ②	$CaCO_3 \cdot nH_2O$ Low in Alkali (Baker) ①	$CaCO_3 \cdot nH_2O$ Low in Alkali (Baker) ②	$CaCO_3 \cdot nH_2O$ Low in Alkali (Baker)
Assay MgO	41.8 min	--		--	--	
Assay $CaCO_3$	--	--	--	99.1%		
Mg	--	--	--	<.01		
Ca	<.002	--		--	--	
Insol HCl	.003			.003		
Cl	<.001			.001		
SO_4	<.001			.005		
Heavy Metals as Pb	<.001			.0005		
Iron	<.001	.0008	.0021	<.0005	.0006	
Water Soluble	.3			--		
Ammonia ppt.	--			.002		
F	--			.001		
Ba	--			.002		

	$MgCO_3 \cdot nH_2O$ (Baker)[1]	$MgCO_3 \cdot nH_2O$ (Baker)[2]	MgO[2]	$CaCO_3 \cdot nH_2O$ Low in Alkali (Baker)[1]	$CaCO_3 \cdot nH_2O$ Low in Alkai (Baker)[1]	$CaCO_3 \cdot nH_2O$ Low in Alkali (B aker)
K	.004[3]			.008		.0071[3]
Na	.374[3,4]	.1900	.2250	.007	<.001	.0065[3]
St	--	.0005	.0010	.01	.0165	
Al		.0181	.0058		.0060	
Cu		.0003	.0006		.0018	
Mn		.0022	.0040		.0004	
Ni		<.0001	.0013		.0018	
Si		.0367	.0503		.0090	
Ti		<.0001	.0001		.0005	
B		.0005	.0011		.0006	

1. Analysis quoted by manufacturer
2. Analysis by Barringer Research Ltd. (spectrographic)
3. Analysis by Martin Van Oosten (Atomic Absorb)
4. Analysis following firing to 1700°C showed <.0098% Na in the MgO

a residual of less than 0.0098% Na which was considered negligable.

The additives used were quite pure as shown in Table 3-2. Also their presence at less than the 2% level would dilute any impurities in the additives to secondary importance.

3.2. Optimization of Calcination and Pressing

3.2.1. Degree of Decomposition of Carbonates

The carbonates were calcined at a range of temperatures from 500°C to 1200°C for 12 hours in recrystalized Alumina Crucibles and the degree of decomposition as a function of calcination temperature was determined by the weight loss following firing to 1700°C for 5 hours as described in Section 3.7. An analytical balance capable of 0.001 gram reproductibility was used. The results are shown in Figure 3.1 and are generally based on the weight loss of 6 samples giving a small standard deviation.

The results indicate that $MgCO_3$ is completely decomposed by 1000°C as is $CaCO_3$.

3.2.2. Determination of Density

The shrinkage and bulk density measurements were determined by direct measurement of the specimens while the specific gravities were determined by holding the previously weighed samples in a vaccuum system which could be flooded with liquid. The liquid impregnated samples were then weighed syspended in liquid to determine their

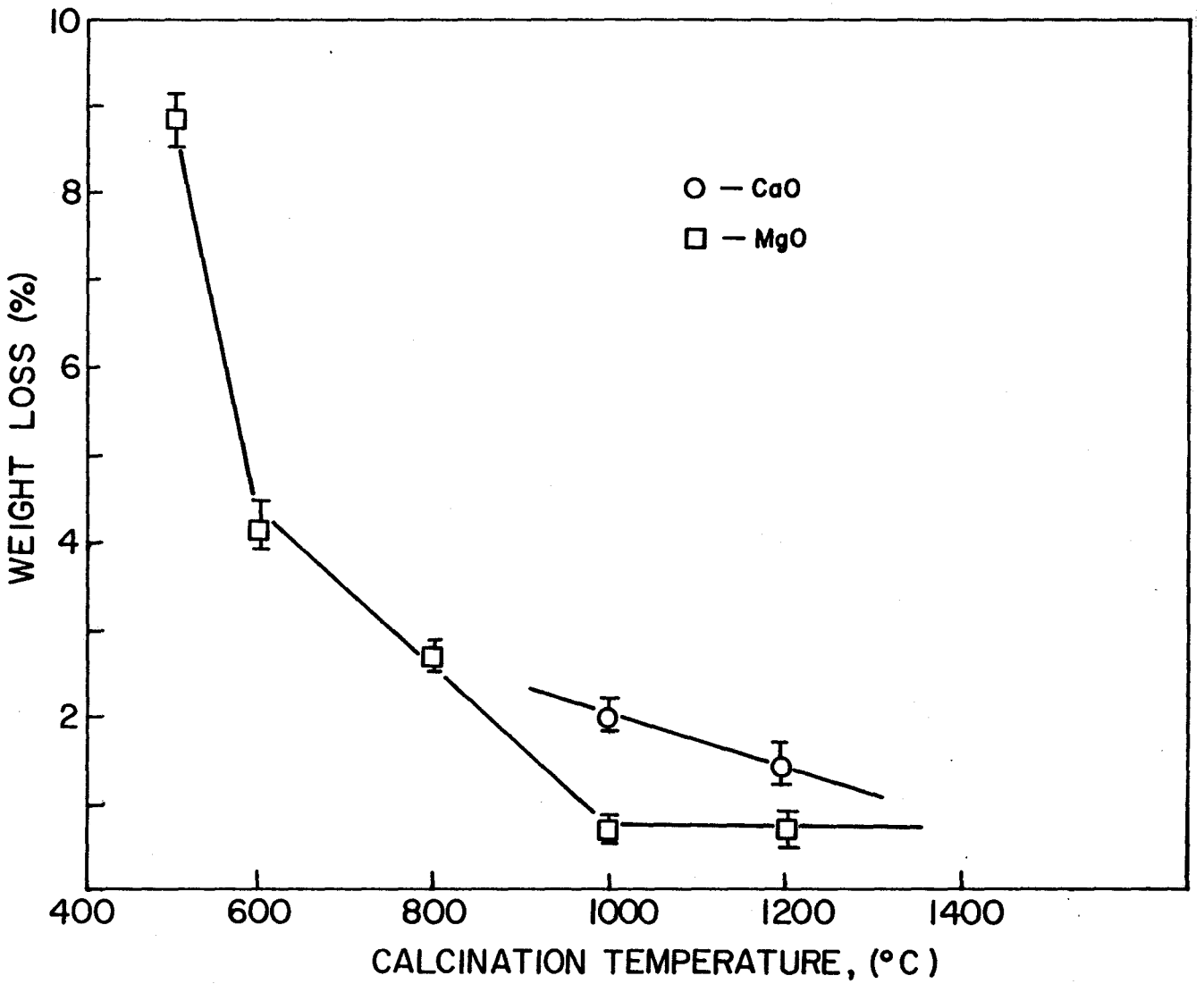

Figure 3-1 Degree of decomposition of carbonates

Table 3-2 Chemical Analysis of Additives in PPM

	Fe_2O_3 [2]	GeO_2 [1]	Ta_2O_5 [1]	TiO_2 [2]	V_2O_5 [1]	WO_3 [1]	SiO_2 [3]
Assay	99.7%	99.999%	99.9%	99.9%	99.9%	99.9%	
B	--	--	<1	--	--	--	
Bi	--	--	<1	--	--	--	
Ca	--	--	<1	--	--	1	
C_o	--	--	<1	--	--	--	
Cr	--	--	<1	--	--	1	
Cu	20	.05	<1	--	--	2	
Mg	--	--	<1	--	--	--	
Mn	100	--	<1	--	--	--	
Ni	--	--	<1	--	--	1	
Pb	--	--	<1	20	--	10	
Fe	--	--	<3	100	105	1	
V	--	--	<3	--	--	--	
Sn	--	--	<3	--	--	--	
Al	--	--	<5	--	--	1	

	Fe_2O_3 [2]	GeO_2 [1]	Ta_2O_5 [1]	TiO_2 [2]	V_2O_5 [1]	WO_3 [1]	SiO_2 [3]
M_o	--	--	5	--	--	6	
Ti	--	--	5	--	--	--	
W	--	--	5	--	--	--	
Zr	--	--	5	--	--	--	
Si	--	0.7	10	--	410	3	
Nb	--	--	50	--	--	--	
As	P.T.	--	--	.4	--	5	
Na	--	--	--	--	185	5	
K	--	--	--	--	--	12	
Cl	--	--	--	--	.70	--	
Zn	30	--	--	30	--	--	
NO_3	100	--	--	--	--	--	
PO_4	100	--	--	--	--	--	
SO_4	1700	--	--	--	--	--	
Other	900	Not PPT by NH_4OH		300	Water Soluble Salts		

[1]) Cerac/ Pure Inc

[2]) Fisher

[3]) Fisher Floated Powder

displacements as described in ASTM 20. The liquid used was isopropl alcohol in order to avoid hydration of the CaO phase

3.2.3. Effects of Calcination, Temperature and Pressing Pressure on the Fired Densities

From Figures 3-2 and 3-3 it can be seen that the calcination temperature has an effect upon both the specific gravity and the bulk density of MgO. It can also be seen that the bulk density of the CaO is also influenced by the calcination temperature. However the specific gravity of the CaO is not appreciably affected by calcination over the range of temperatures studied. (Table 3-3).

From the large differences between the specific gravity and bulk density it can be seen that all of the specimens showed continuous porosity following firing, indicating that second stage sintering was still proceeding. The fact that the MgO pressed at 5000 PSI showed a higher specific gravity and lower bulk density than all other specimens of MgO would indicate either that the porosity had never been reduced enough to allow exaggerated grain growth and attendent pore entrapment or alternatively that sintering proceeded more slowly in these compacts so that fewer pores became isolated in the course of sintering.

Figure 3-4 shows the effect of calcination temperature and pressing parameters on the shrinkage of compacts during firing. It is important to minimize this shrinkage in order to minimize stress and maintain size tolerances on the material. It can be seen that the optimum calcination temperature for MgO is between 800°C and 1000°C

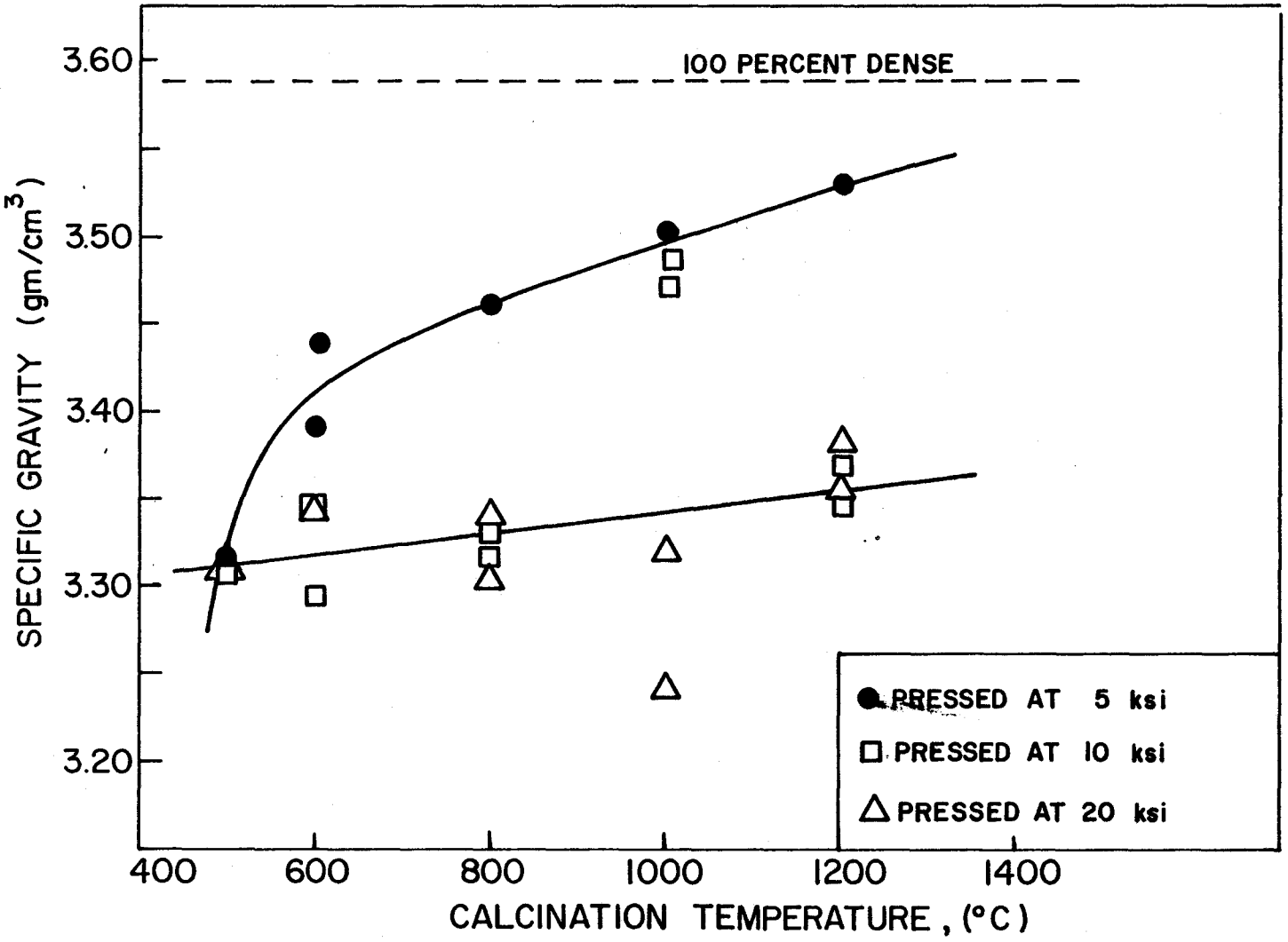

Figure 3-2 Effect of calcination temperature on specific gravity of MgO.

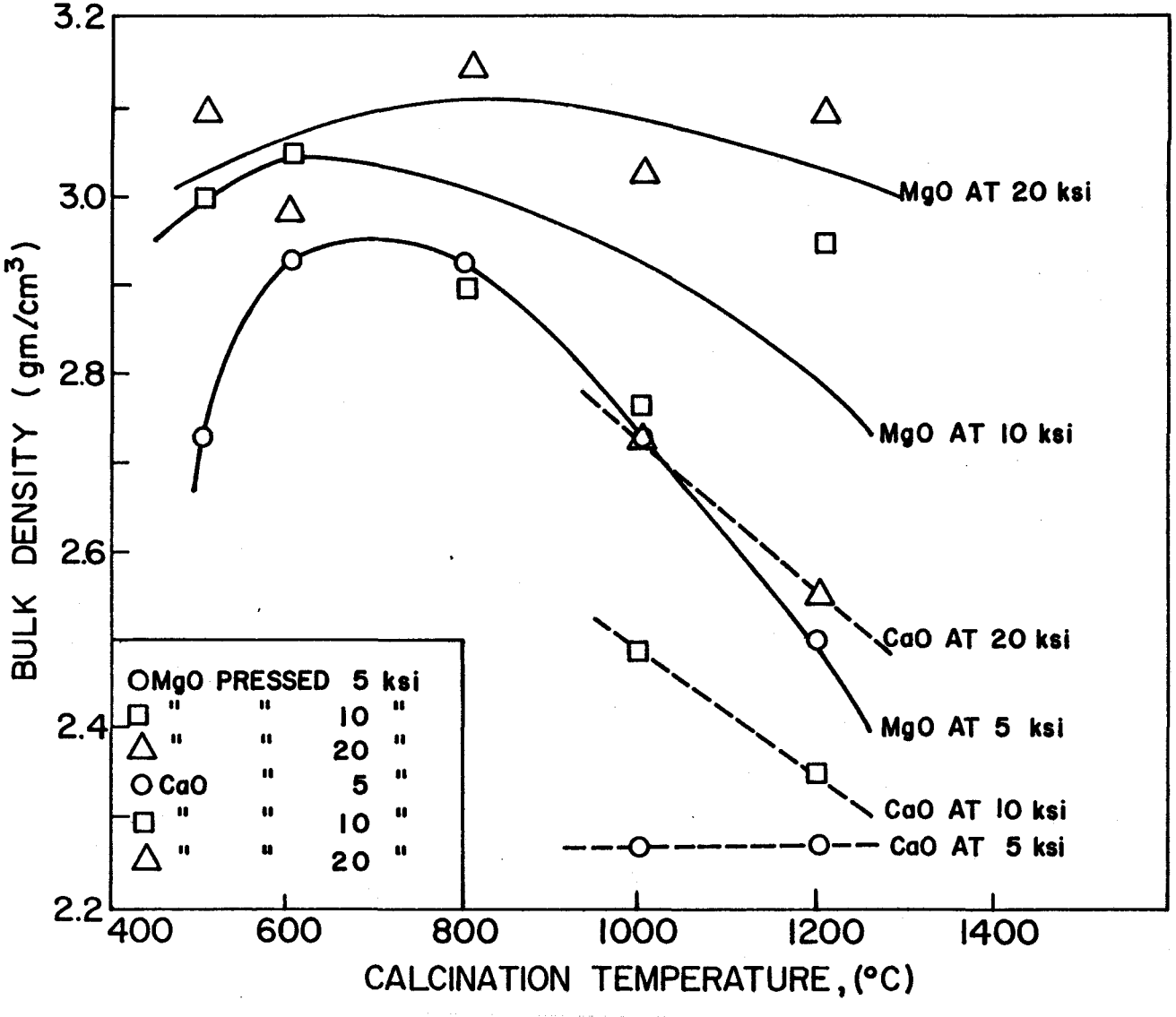

Figure 3-3 Effect of calcination tempeatture on the bulk density of MgO and CaO.

Table 3-3

Effect of Calcination Temperature & Pressing on the Specific Gravity of CaO

Calcination Temperature (°C)	Pressure (KSI)	Specific Gravity (gm/cm^3)	Green Density (gm/cm^3)
1000	5	3.286	1.25
	10	3.296	1.44
	20	3.27	1.64
1200	5	3.298	1.41
	10	3.298	1.56
	20	3.290	1.72

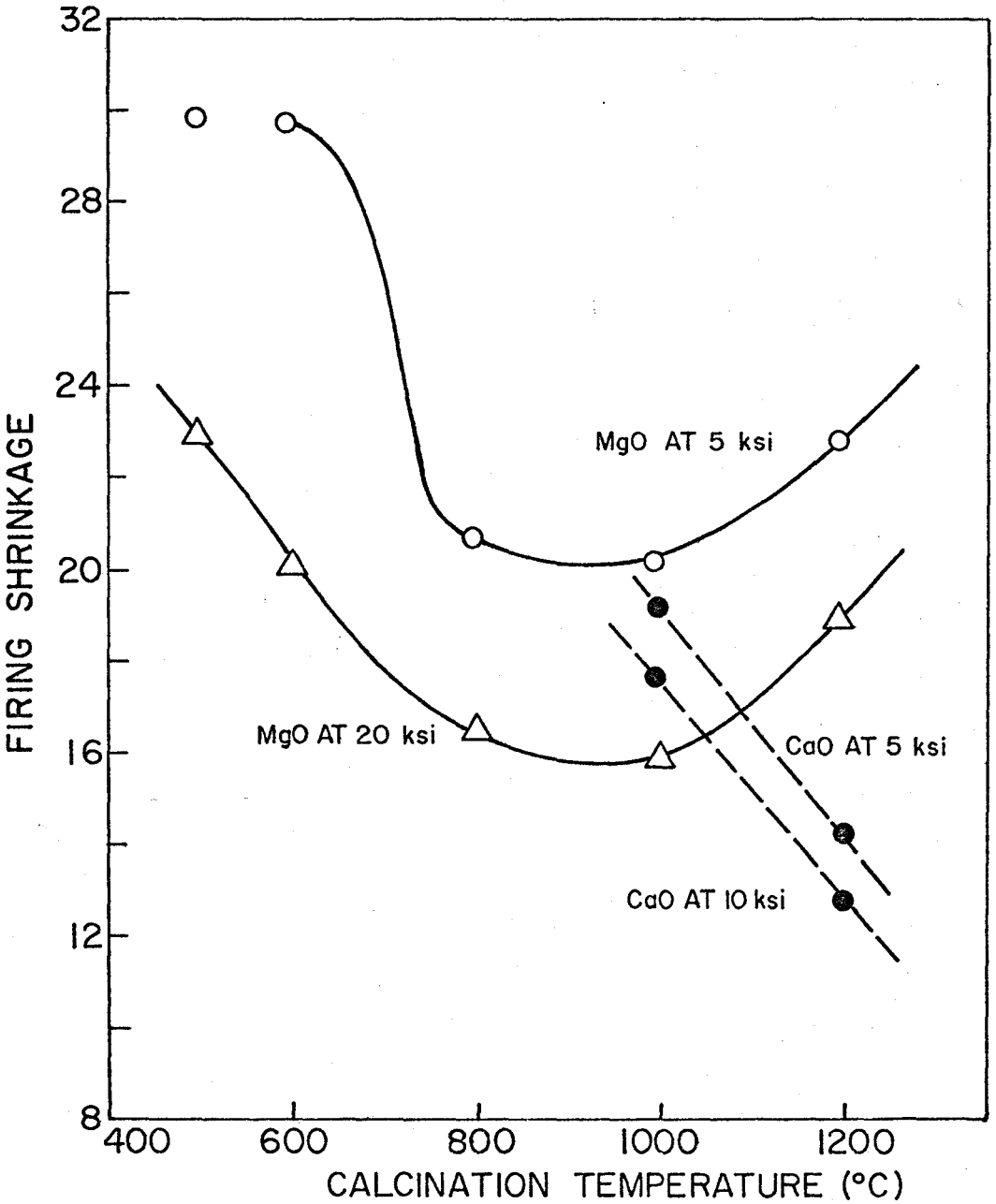

Figure 3-4 Effect of calcination temperature and pressing on firing shrinkage.

and that increasing pressure results in decreased shrinkage. Again the data for CaO shows a similar behavior, although the effect of pressure is less pronounced in CaO.

From Figure 3-5 that an optimum green density for MgO is achieved between 800°C and 1000°C for each pressure tested. Similar results for CaO, presented in Figure 3-6, show that both increased calcination temperature and pressing pressure result in higher green density.

Figures 3-7 and 3-8 show the relation between the green density and fired density for MgO and CaO respectively. The MgO data in Figure 3-7 fits the least squares line with a correlation coefficient of 0.60 which for 15 points yields a 99% probability that the variables are dependent. For CaO, 6 data points yield a 90% probability. In addition from the distribution of points it can be seen that the primary effect of increasing calcination temperature is to increase the green density of the powder compacts.

3.2.4. SEM of Calcined Powders

In order to investigate the effect of calcination temperatures on the morphology of the initial powders and determine the initial particle size in the compact, samples of each calcined oxide were studied on the SEM.

It was found that at 600°C the $MgCO_3$ decomposed to form fine platelets approximately .05 μm in thickness and 5 μm across (Figure 3-9).

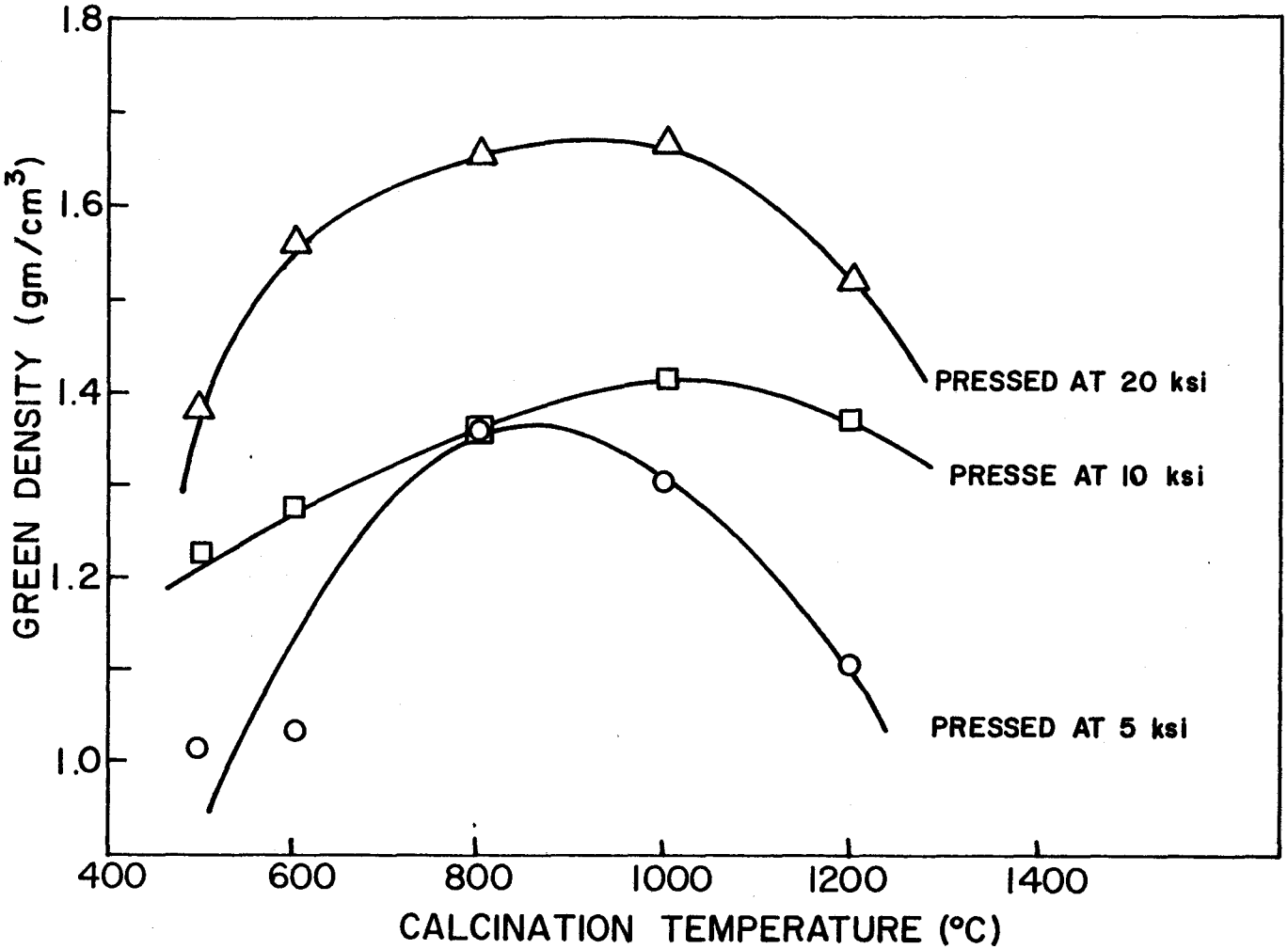

Figure 3-5 Effect of calcination temperature and pressing pressure on the green density of MgO.

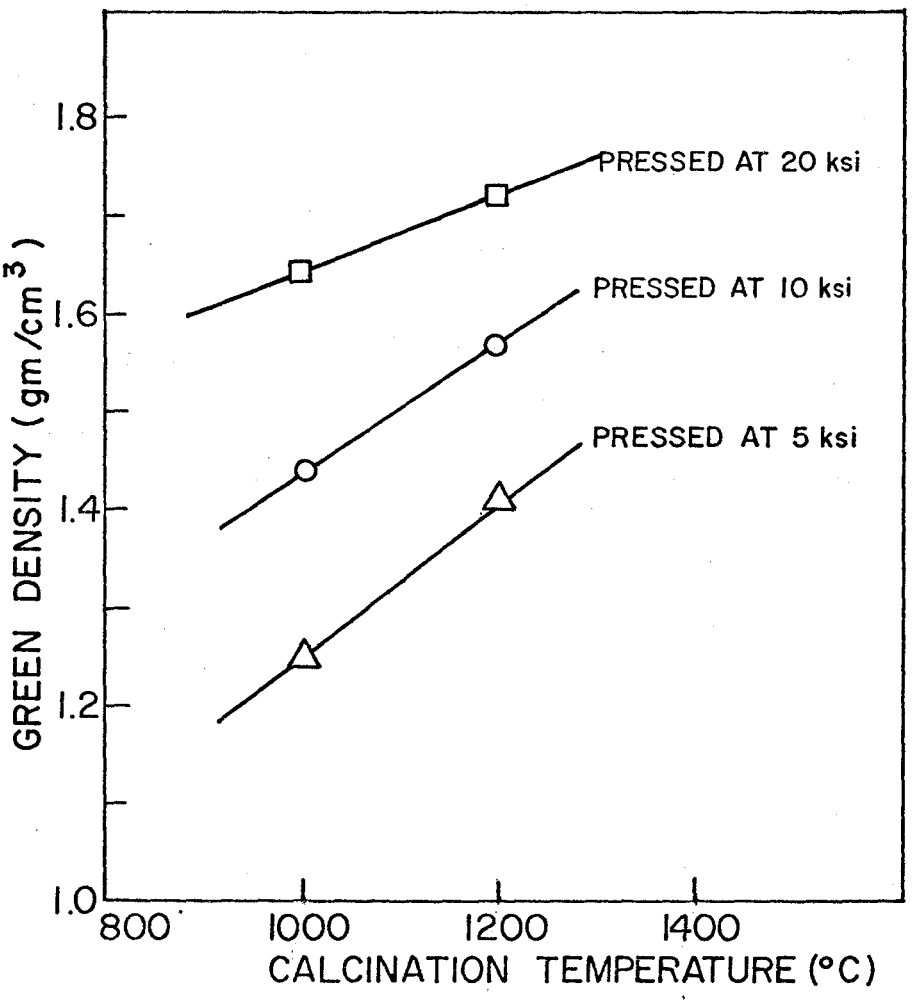

Figure 3-6 The effect of calcination temperature and pressing pressure on the green density of CaO.

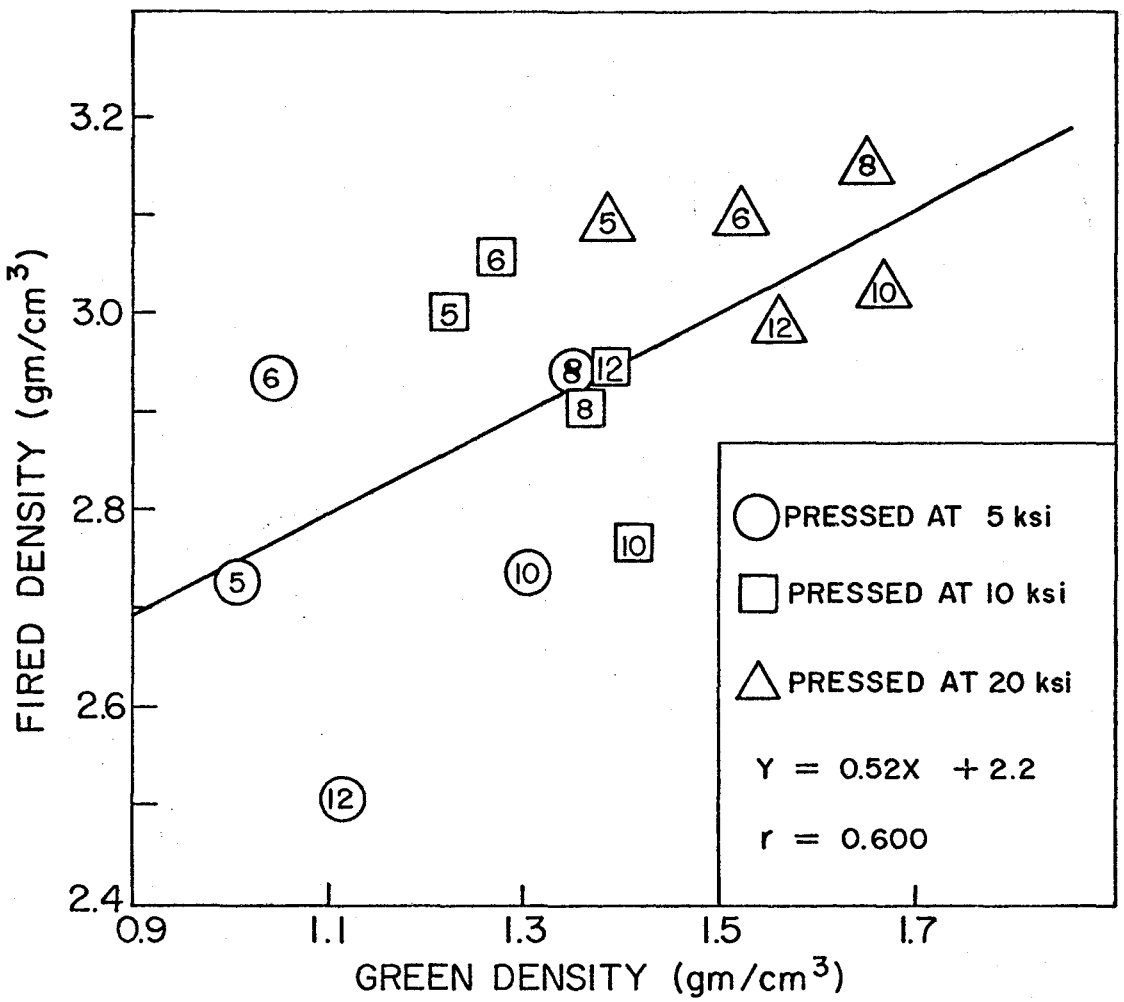

Figure 3-7 Effect of green density on fired density. Number enclosed in the symbols represent calcination temperature in hundred of degrees C. Results for MgO.

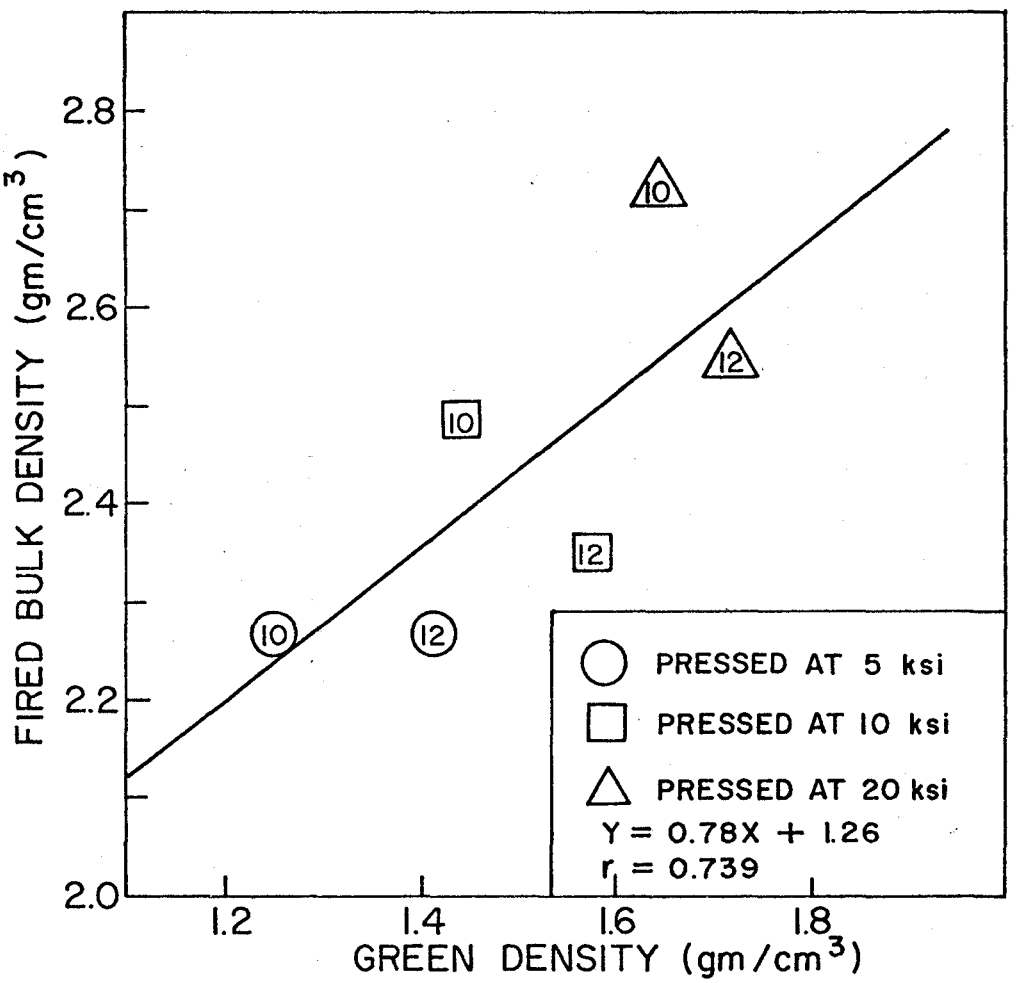

Figure 3-8 Relation between green density and fired density for CaO. Number enclosed in symbols represent the calcination temperature in hundreds of degrees centigrade.

At 800°C the plate structure was subdivided into tiny crystals (Figure 3-10). By 1000°C the structure began to resemble that obtained at 1200°C which is shown in Figure 3-11.

It can be seen that the material calcined at 1200°C is sintered together into large agglomerates. This suggests that the material will have less ability to pack tightly and thus could account for the fall off in green density and fired density for material calcined at 1200°C. It should be noted that these calcines were clumped into loose agglomerates approximately 15 μm in size at all temperatures. This size is close to the final grain sizes obtained in the CaO-MgO compositions indicating the possibility of little or no grain growth in the two phase materials.

Similar results were obtained for CaO although no reproducable micrographs could be taken due to the rapid hydration of the finely divided CaO. The $CaCO_3$ calcined at 1000°C and 1200°C demonstrated considerable agglomeration due to sintering. SEM work showed 0.5 μm cubes of CaO sintered tightly into clumps of approximately 15 μm diameter.

3.3. Powder Preparation

3.3.1. Preparation of Powders following Calcination

Following calcination the MgO powder was loose and was sieved through a 325 mesh screen to remove any foreign material and large clumps of oxide. The CaO was slightly sintered together and it was necessary to grind it before sieving. Difficulty was experienced with

Figure 3-9 $MgCO_3$ calcined at 600°C
Magnification SEM x 9500

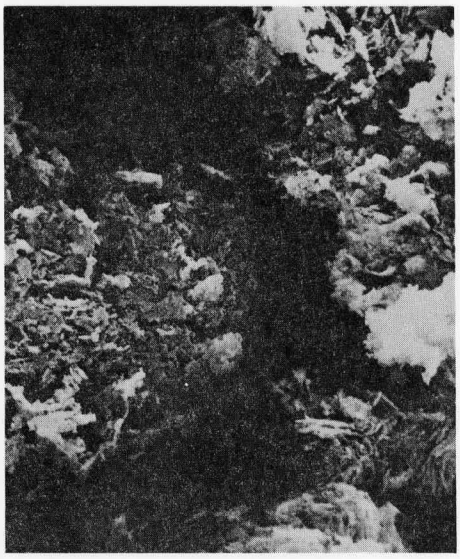

Figure 3-10a

Figure 3-10b

$MgCO_3$ calcined at 800°C

SEM magnification a) 2050x
b) 10000x

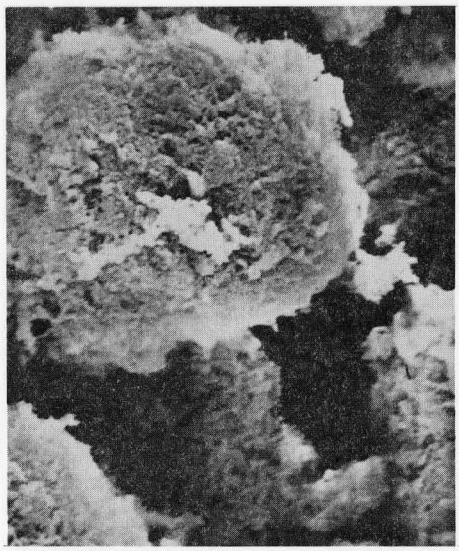

Figure 3-11a

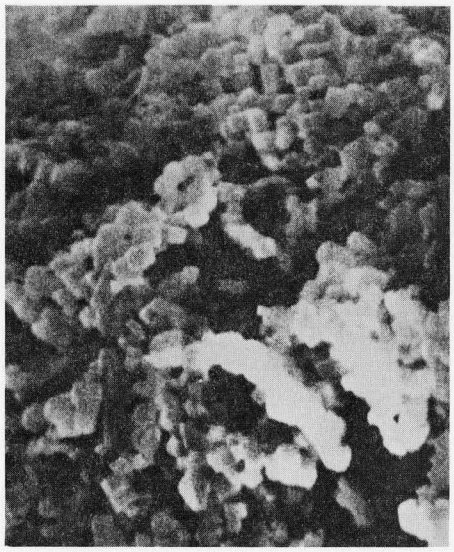

Figure 3-11b

$MgCO_3$ calcined at 1200°C

SEM magnification a) 2000x
b) 10000x

the electrostatic charging of the particles and the clogging of the screens. The 325 mesh screen was used with repeated cleaning necessary.

Following sieving both powders were placed in glass bottles with taped lids. These powders were then used as quickly as possible in order to minimize hydration problems. This technique of storage proved adequate since subsequent weight loss or firing showed little hydration.

3.3.2. The Mixing of Powders and Additives

Measured quantities of the calcined powders and additives were mixed in an isopropl alcohol slurry as described by Rice (50). The slurry was constantly stirred in a pyrex breaker over a hot plate to evaporate the alcohol. The powders were then held at 100°C for 24 hours for final evaporation of the alcohol before pressing.

This technique was found to produce more uniform mixing than several of the dry mixing techniques tried.

3.4. Effects of Additives on MgO and CaO Separately

In order to evaluate the potential effectiveness of the additives chosen in the production of a satisfactory microstructure in magdol, a series of preliminary experiments were carried out utilizing additive levels of between 0.2% and 5% mixed with CaO and MgO individually.

The effects of these additives upon sintering was determined

by measurement of shrinkage, bulk density and weight loss as previously described for the calcination experiments. These results were then compared with pure MgO and CaO as standards.

The specimens were also polished and etched in order to estimate their relative grain sizes by linear intercept techniques. In addition some of the specimens were observed by SEM and X-ray analysis to detect any concentration of the additives.

3.5. Ceramography

Three distinctly different types of samples were prepared for microscopic observation. The first two were the MgO plus additives and the CaO plus additives. These were prepared for initial evaluation of the additives. The third was the mixed compositions typically 60% MgO and 40% CaO.

3.5.1. Magnesium Oxide

These samples had variable densities and grain sizes and as noted elsewhere (149) pullouts of entire grains and parts of grains was a major problem. In order to prevent this the samples were vaccuum impregnated with Epofix epoxy resin in an apparatus similar to that previously described by Green (121). The resin was held at 50°C in order to increase its fluidity.

Polishing was accomplished using water as a lubricant on the coarse papers followed by 6 μm and 1 μm diamond on napless nylon

cloth and 0.3 μm alumina.

Many etching solutions are quoted in the literature (49,54, 93,150,151) but a 50% solution of HNO_3 in water was found to be suitable.

3.5.2. Calcium Oxide

Calcium oxide must be kept isolated from all forms of water for it rapidly hydrates, either destroying the polish or the entire sample depending upon the time of exposure (152).

These samples were vaccuum impregnated with Epofix to prevent pullouts and in an effort to seal them against the atmosphere. The polishing procedure was the same as for MgO except that kerosene was used exclusively as a polishing lubricant.

After Daniels (49), a 4% solution of picric acid in methanol was used as an etchant. It was found necessary to keep drying chips in the etchant to remove the last traces of water.

The samples were stored in desecators containing P_2O_5 dessicant and acceptable quality could be maintained for up to a week.

Exposure to the air resulted in slight surface discolouration which did not hinder observation.

3.5.3. Doloma Mixtures

The same precautions were observed as with CaO.

Due to the differing hardness of the two major phases, a tendency to relief polish was noticed even with nylon cloths. Hence

polishing times were kept as brief as possible.

Since the MgO phase could not be etched without the complete destruction of the CaO phase, giving an extremely rough surface, a thermal etching procedure was developed.

It was found that samples polished to 1 μm on the diamond wheel (with no epoxy) could be etched by heating for ½ hour at 1500°C and the grain structure observed on theSEM. This procedure was also applied to a number of the single oxide samples with good success.

3.6. Pressing of Mechanical Test Specimens

Initially trials were run with 10 x 2.5 x 2 cm bars pressed to 4000 psi in a steel mold (shown in Figure 3-12) on the Tinious Olsen. However since problems developed with shrinkage cracks and warping due to uneven powder packing, a modified technique was developed.

First the powders were uniformly packed into the mold using a Syntron vibrating table and prepressed to approximately 2500 psi to provide a blank of the desired shape.

After this the bars were placed in propolactics and isostatically pressed to 20,000 psi before firing. It was observed that warpage would occasionally occur in the isostatically pressed bars due to uneven packing through the thickness of the prepressed bar. This warpage was often removed by firing, although several warped bars did retain their shape. This however had no deleterious effect upon the fired bars in terms of residual stresses as, during sintering, a great deal of particle rearrangement occurs so relieving any internal stresses.

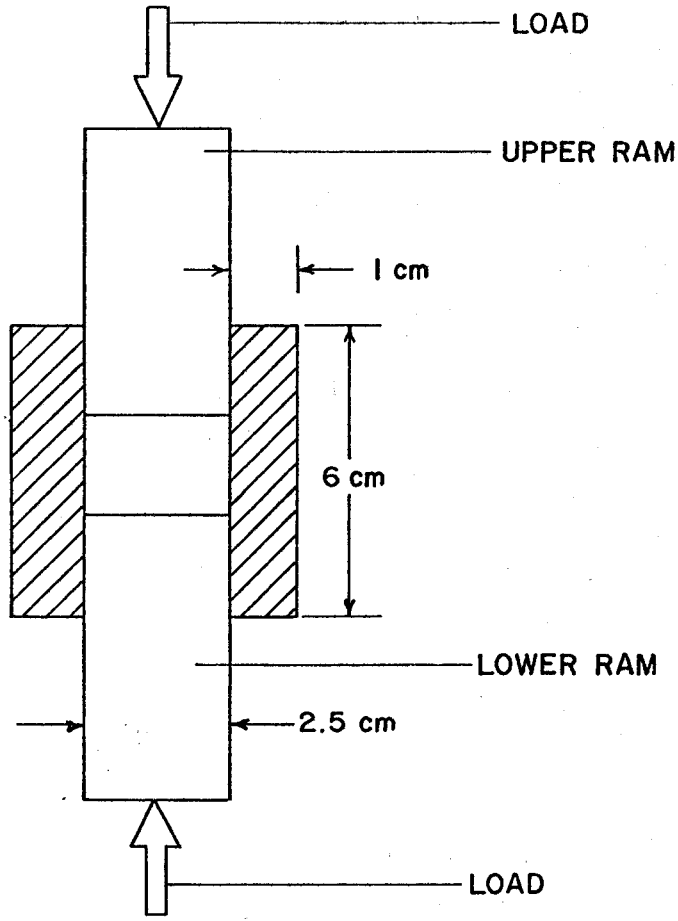

Figure 3-12 Cross-section of mold

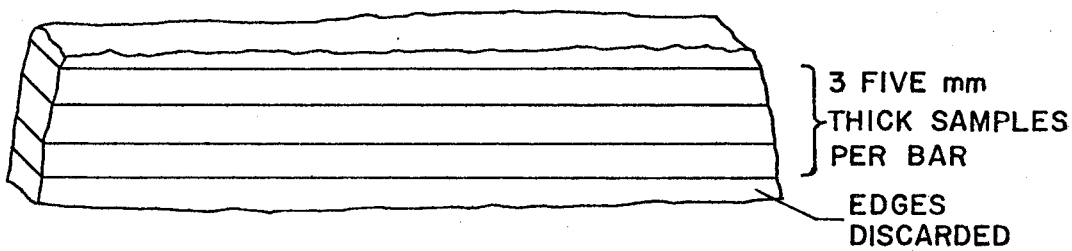

Figure 3-13 Preparation of samples from fired bars with diamond saw (actual size)

3.7. Firing Schedule

Each group of specimens were fired in a C&M High Temperature Furnace according to the program outlined in Table 3-1.

Table 3-1

Firing Program

Initial Temperature	20°C
Heating Rate	5°C/min
Set Point	1700°C
Cooling Rate	2°C/min
Final Temperature	20°C

The low rate of cooling allowed the specimens to cool uniformly throughout thus preventing bulk residual stresses.

3.8. Preparation of Test Bars

The fired bars were cut on a kerosene-cooled diamond waffering saw into rectangular prisms approximately 0.5 cm x 0.7 cm x 8 cm as shown in Figure 3-13. The sides of these bars were closely parallel and smooth to minimize knife edge friction.

Notches were introduced into the freshly cut side of the specimen to a depth of approximately 0.4 of the thickness of the specimen (0.2 cm) using a 4 x .010 inch diamond waffering blade on an Isomet low-speed saw.

The depth of the cut was measured with the aid of a travelling microscope to an accuracy of .001 cm.

A study of the notches produced in this manner indicated that the notch width was less than 0.02 cm.

3.9. Fracture Rig

The notched fracture toughness specimens were broken at a range of temperatures from 20°C to 1500°C using a dead-loading system illustrated in Figure 3-14. The load was applied by pouring quantities of lead-shot into a plastic dish on the loading platform which was weighed following fracture. The transducer was primarily used to monitor the occurence of the fracture. The load was applied to the specimen in the furnace by means of dense MgO knife edges held in recrystallized alumina rods. This entire system was counterbalanced by a system of weights and pulleys. The support for the specimen in the furnace consisted of MgO knife edges upon a block of recrystallized alumina which in turn rested, via a ¼ inch lucalox pivot, upon a heavy alumina rod extending out of the furnace. The presence of the lucalox pivot simplified the alignment problems considerably.

The knife edges were replaced as necessary. The upper knife edges were set with 1 cm spacing and the lower with 3 cm spacing.

The furnace could easily maintain 1500°C and access to the specimen was provided by its clamshell structure.

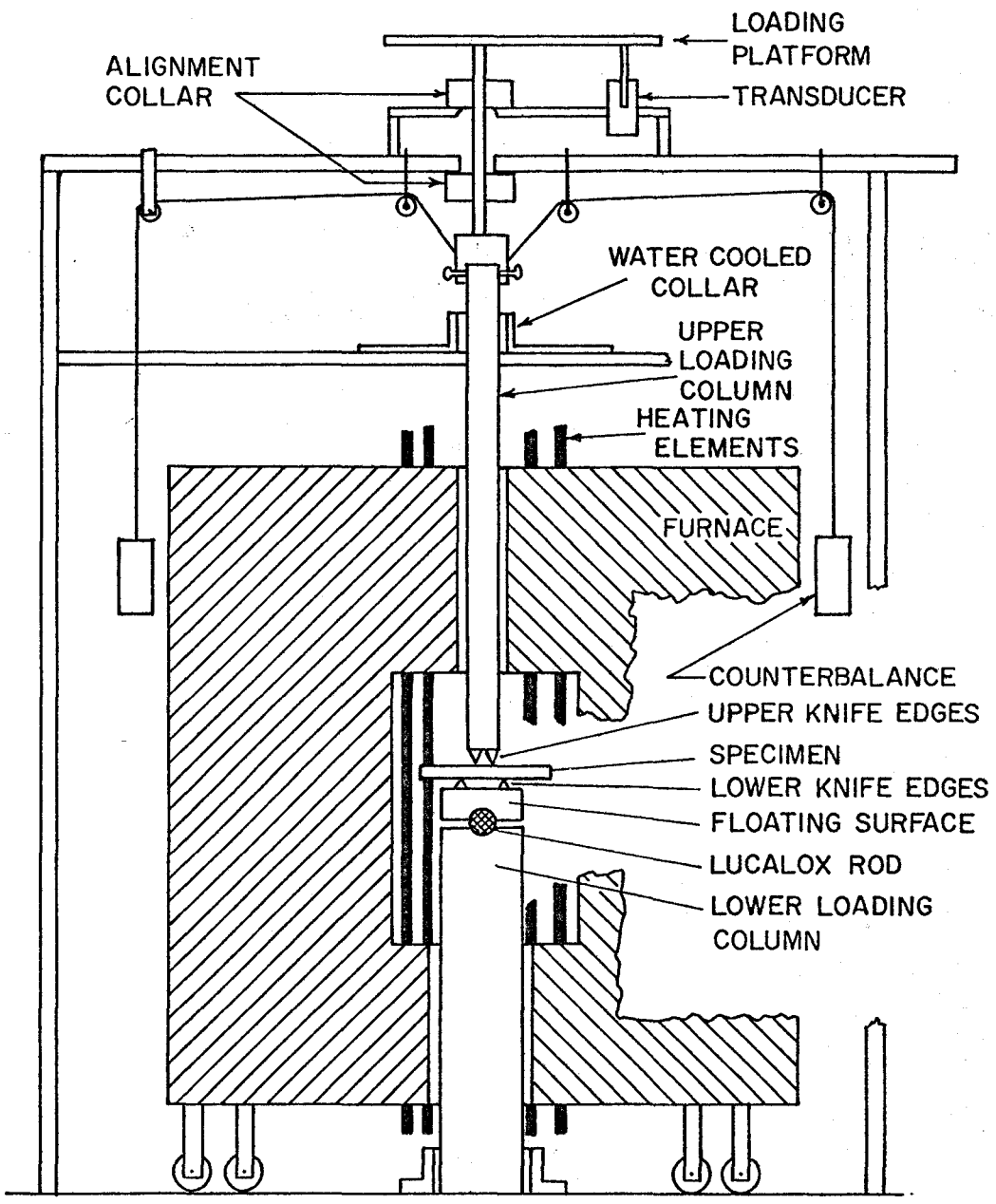

Figure 3-14 High Temperature Fracture Rig

3.10. Calibration of the Fracture Rig

It is important that the K_{1C} values obtained using the dead load system correspond to those in the literature which were obtained using hard machines. Several sets of tests were undertaken using both the rig described and the table model Instron. Four tests were done,

1. Modulus of Rupture of glass slides on both the dead load rig and Instron.
2. Fracture toughness of 5 mm square prisms of soda-lime glass.
3. Fracture toughness of 60% dense alumina on both rigs.
4. Fracture toughness of 95% dense alumina on both rigs.

The results of these tests were analysed by means of the Student's t test (as outlined in Appendix II) and the results shown in Table 3-2. It was concluded that the values obtained from the dead load system were the same as those obtained with the Instron, within experimental error.

3.11. SEM of Fracture Faces

A specimen of the fracture face of each composition-temperature combination was coated with gold and observed in the Cambridge SEM at 20 KEV, to determine the mode of fracture.

In addition a few notches were studied after loading to near fracture loads, to determine any subcritical crack growth.

Table 3-4

Results of Calibration Tests

Material	Test Rig	# of Spec	Mean MN/m3/2	Standard Deviation	Variance	Degrees of Freedom	t	Significance
Modulus of Rupture Glass Slides	Instron	11	72.2*	16.0	681	10	4.2***	99% confidence (***F test that samples are the same)
	Dead+	23	69.8*	16.3	2851	22		
Toughness of Pyrex	Dead+	5	0.762	0.080	--		0.056	No significant difference
Ref. 144 Literature Value	--		0.760	--	--			
60% Dense** Al_2O_3	Instron	9	0.836	0.253		15	1.9	90% confidence that there is a difference. (A very weak significance level)
	Dead	7	0.631	0.143	---			
95% Dense Al_2O_3	Instron	4	2.224	0.303	--	7	0.256	No significant difference
	Dead	4	2.266	0.125	--			

\+ Dead Load ~~Creep~~ Rig

* MN/m^2

** Comparable to values quoted in Ref. 139.

CHAPTER 4

RESULTS & DISCUSSION

4.1. The Effects of Additives on the Microstructure of CaO and MgO Separately

4.1.1. Introduction

The effects of a range of additives on the grain growth and sintering characteristics of MgO and CaO were evaluated in preliminary experiments to determine the possibilities for modification of the more complex magdol microstructures. It was initially hoped that by utilizing additives, the degree of encapsulation of CaO by MgO could be modified. Unfortunately the microstructures of the magdol mixtures produced were such as to preclude any quantitative measure of encapsulation such as undertaken by Kriek et al., since the samples were too porous. Despite this, examination of the component oxides provided useful data for the interpretation of the fracture results.

The grain size and density results obtained are summarised in Table 4-1. These results showed three basic types of behavior. The V_2O_5, GeO_2 and Fe_2O_5 doping resulted in increased grain size with increased levels of addition. Doping with Ta_2O_5, WO_3 and TiO_2, on the other hand, resulted in reduced grain sizes with increased levels of addition. SiO_2 additions showed little effect on grain growth.

It is extremely difficult to draw any quantitative conclusions from these preliminary experiments due to the following reasons:

1. For six of the compounds studied (V_2O_5, Na_2O, TiO_2, Ta_2O_5, WO_3, GeO_2) there is little or no data available in the literature on solubility in MgO and CaO for 1 to 5 percent levels. SiO_2 and Fe_2O_3 are the exceptions.
2. Phase equilibria data is deficient for Ta_2O_5, V_2O_5, GeO_2 and Na_2O in combination with MgO and CaO as indicated by the extensive dotted lines in the former three pairs and the absence of the latter from the literature.

Table 4-1

Microstructure of CaO and MgO with Dopants

Dopant	Mean Grain Size (μm)		Percent Theoretical Bulk Density		Percent Theoretical Specific Gravity	
	MgO	CaO	MgO	CaO	MgO	CaO
None	21	22	88.0	82.7	94.1	99.1
.5% V_2O_5	--	54	--	92.2	--	--
1%	52	65	88.8	90.7	--	--
2%	--	94	--	91.6	--	--
.4% GeO_2	37	20	91.7	89.7	94.4	--
1%	42	32	87.8	90.0	91.3	--
2%	47	34	86.4	90.3	91.6	--
.5% Ta_2O_5	97	(25,3)[1]	93.3	88.3	99.1	--
1%	78	--	93.1	89.0	95.5	--
2%	67	(22,3)[1]	89.9	85.7	95.0	--
.2% WO_3	25	62	90.8	89.8	93.8	--
1%	13	40	87.3	89.3	92.0	--
2%	13	32	86.6	87.6	98.9	--
.5% Fe_2O_3	31	72	94.7	88.9	94.9	89.1
1%	28	99	93.5	90.0	93.5	90.6
2%	35	137	94.6	88.6	94.6	88.7
5%	70	172	93.3	89.4	94.0	89.4
.5% SiO_2	22	17	88.6	65.0	89.8	100
1%	(27,8)[1]	18	90.2	67.3	91.5	100
2%	(26,5)[1]	21	90.7	66.6	91.6	100
5%	19	19	86.7	67.1	89.8	100
1.3% TiO_2	125	78	92.1	92.5	92.2	92.4
2.3%	100	51	93.5	92.5	94.0	94.5
6.6%	73	37	93.1	94.3	93.8	95.6

[1] Duplex grain size distribution

3. The exact distribution of phases and ion concentrations is very uncertain even at room temperature even in carefully investigated systems such as Ludox. Conditions at elevated temperatures (1700°C) are even more speculative at this time.
4. The current theories of grain growth are based upon phenomena observed in high purity metals where intrinsic diffusion may be expected and porosity is not a constantly changing factor. In impure oxide systems which are sintering and grain growing simultaneously in a non-isothermal system no concrete conclusions on kinetics may be drawn.
5. The kinetics of sintering in the presence of a liquid phase are still poorly understood. The presence of very low impurity levels can greatly change the nature of the particle surfaces and interfacial energies, the conventional driving force for sintering. The levels at which this occurs are much below the critical levels in metals. The materials used in the present work do not approach the purity required to avoid these effects. It thus becomes impossible to separate out the influence of the additives.

In the sections which follow frequent reference will be made to Table 4-1 both directly and by inference to compare the effects of the different additives on the sintering and grain growth behavior.

4.1.2. Sintering and Grain Growth in Undoped MgO and CaO

The microstructures of the undoped MgO and CaO were examined to form a basis of comparison for the effects of additives on sintering and grain growth. The data presented in Table 4-1 indicate that the MgO sintered to a higher bulk density than the CaO (88.0 vs. 82.7 percent theoretical) and approximately half of the porosity in the MgO is isolated from the surface. The micrographs (Figures 4-1 and 4-2) show

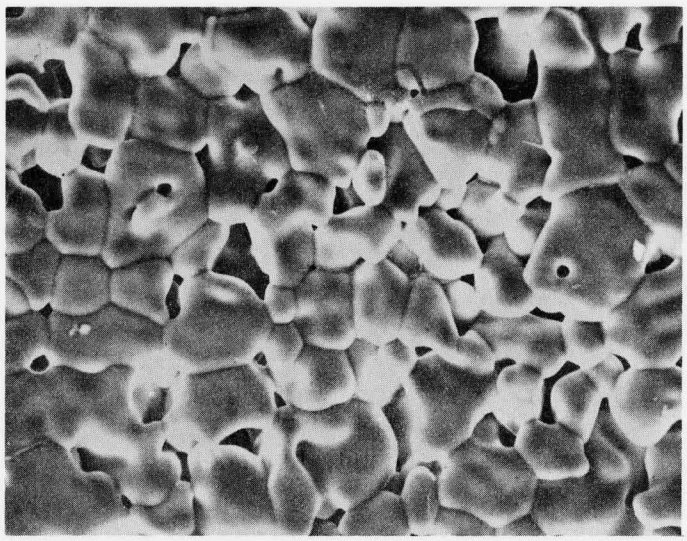

Figure 4-1 CaO calcined at 1000°C
Pressed at 20 KSI Fired 1700°C
Thermally etched (600x)

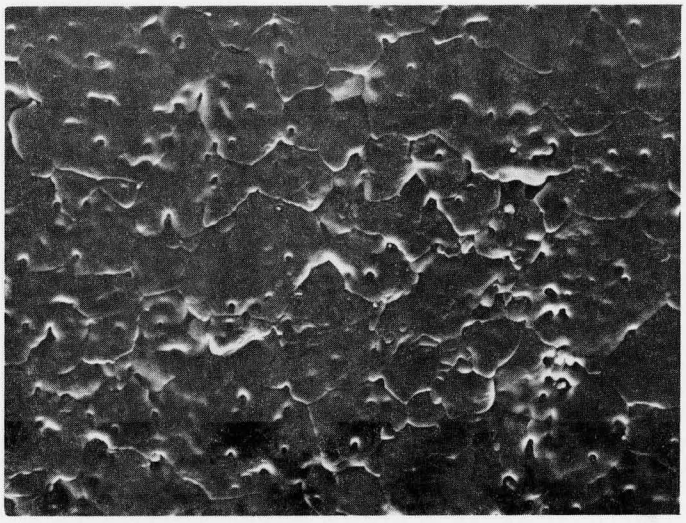

Figure 4-2 MgO calcined at 800°C
Pressed at 20 KSI Fired 1700°C
Thermally etched (600x)

that both oxides have a grain size of about 20 μm, however the intragranular porosity in the MgO indicates that it experienced exaggerated grain growth. This behavior is thought to be due to the presence of 0.0098% Na_2O in the MgO and is similar to behavior observed in Al_2O_3 by others. The mechanism for this effect is unknown at present. Calculations (presented later) indicate that this concentration of Na_2O is enough to form a mono-layer on the MgO grains. Even though Na_2O is expected to flux the MgO, the low density as compared with the V_2O_5 doped samples (which are known to contain considerable liquid phase) indicates that little liquid is formed. An alternative possibility is the solution of Na_2O in the MgO resulting in the creation of vacancies on the oxygen sublattice via

$$Na_2O \rightarrow 2Na^{+} + O^{-2} + V_O$$

The vacancies so produced could change the sintering kinetics, increasing the fired density and providing a mechanism for exaggerated grain growth.

4.1.3. V_2O_5 Doped MgO and CaO

The effects of 0.5%, 1.0% and 2.0% V_2O_5 on the grain size and bulk density of MgO and CaO are listed in Table 4-1. The high bulk densities achieved in both MgO and CaO agree with optical observations that there was no open porosity in these samples. Micrographs of the CaO (Figure 4-3) show that a liquid phase exists at the grain boundaries at the firing temperatures. With a 1% V_2O_5 addition lever rule calculations indicate that 2% liquid is expected at 1380°C with more at higher temperatures (see phase diagram presented earlier). The presence of this liquid at the grain boundaries allows rapid liquid phase diffusion and prevents pinning of the boundaries by solid precipitates. The increased grain size with increased additions is due to the increased liquid contents. The increase in the sintered density and grain size

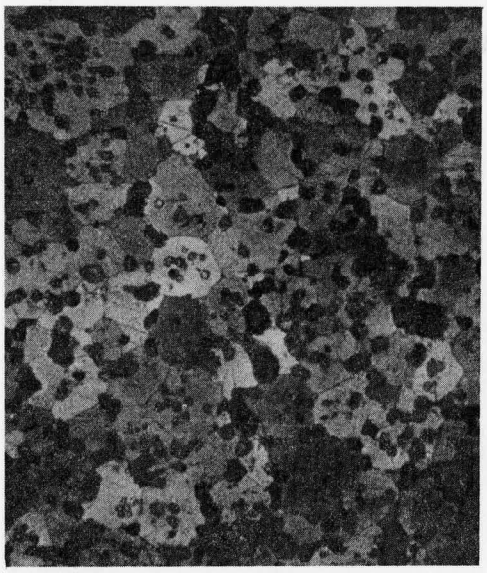

Figure 4-3a

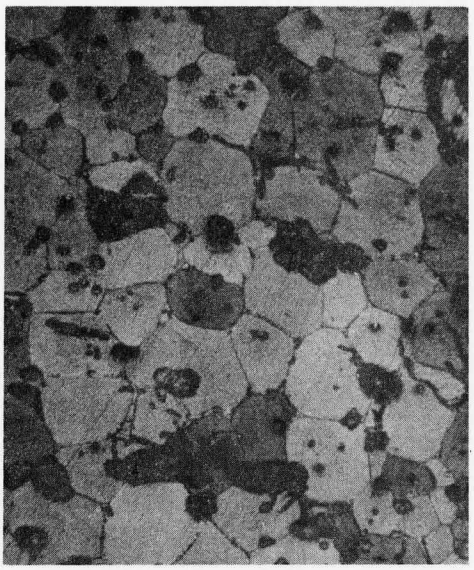

Figure 4-3b

Grain sizes of CaO doped with a)0.5%, b) 2% V_2O_5
Evidence of second phase at grain boundaries and triple points can be seen. (Etched with Picric Acid, 125x)

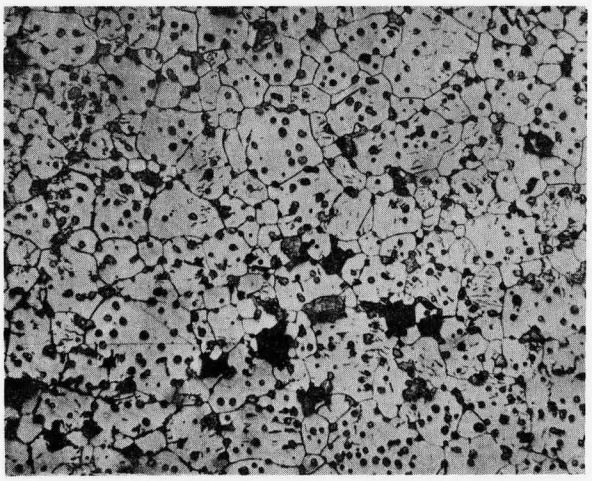

Figure 4-4 Grain size of MgO doped with 1% V_2O_5
Etched with 50% Nitric Acid (125x).

over the undoped CaO may be attributed particularly to the ease of particle rearrangement early in the sintering process allowing grain growth in the early stages to be boundary mobility rather than pore removal limited.

In the MgO samples (Figure 4-4) no direct evidence of liquid formation is seen, however, in view of the MgO-V_2O_5 phase diagram (Section 2.6.6.) with 1% V_2O_5 present, 4% liquid is expected at 1200°C. Brown and Nicholson found that V_2O_5 increased the grain size with levels as low as 0.01%. They also found increasing grain size with increased additions which is consitent with the formation of a liquid film at the grain boundaries as discussed above.

4.1.4. Ta_2O_5 Doped MgO and CaO

The effects of 0.5%, 1.0% and 2.0% additions of Ta_2O_5 on the sintered grain size and density of MgO and CaO are reported in Table 4-1. These additions increased the grain size of the MgO giving grain sizes up to five times that of the undoped materials. Increased Ta_2O_5 however, resulted in decreased grain sizes (Figures 4-5a, b, Table 4-1). This effect is characteristic of a reduction in grain boundary mobility due to precipitate particles pinning of the boundaries. The micrographs used for gain size determination revealed the presence of a highly reflective second phase (Figure 4-5). This second phase was analysed using the x-ray dispersive analyser on the SEM which indicated a high concentration of Ta (Figure 4-6). These precipitates are most likely refractory magnesium tantalate compounds.

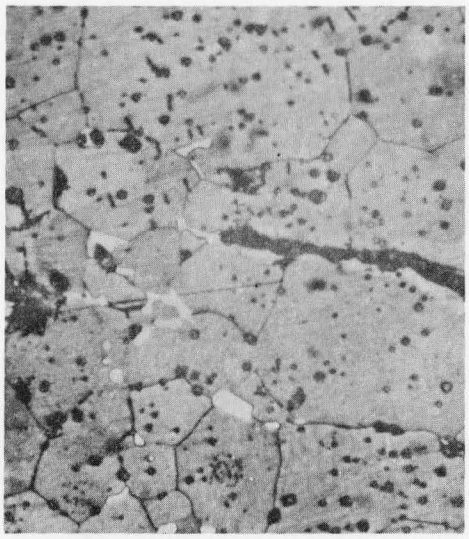

Figure 4-5a

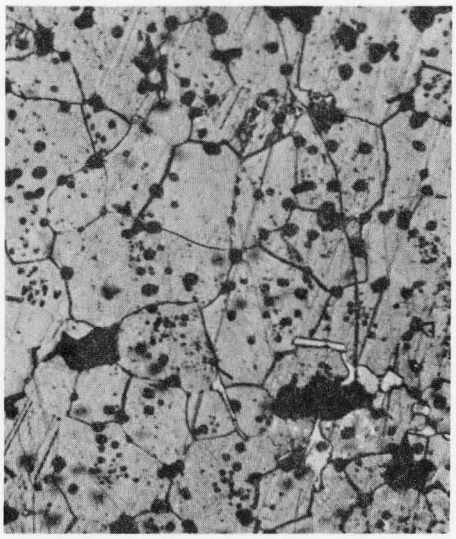

Figure 4-5b

Grain size of MgO doped with a) 0.5%, b) 2% Ta_2O_5. Evidence of highly reflective second phase can be seen in both. (Etched 50% HNO_3, 250x)

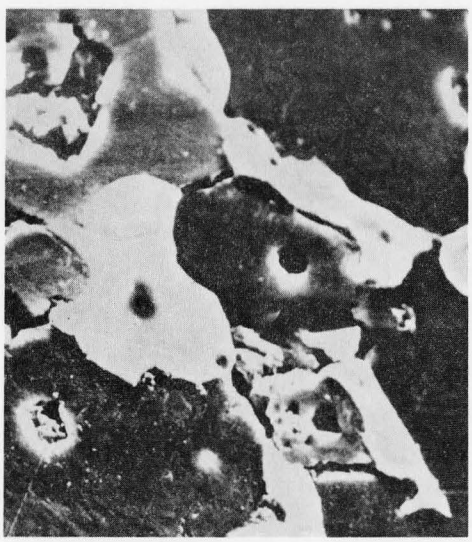

Figure 4-6a

Figure 4-6b

SEM photo a) and Ta X-ray map b) of precipitates in Mgo doped with 2% Ta_2O_5 (1340x).

The addition of 0.5% Ta_2O_5 to MgO resulted in a 5.0% increase in fired bulk density due to restriction of grain boundary mobility thus preventing early exaggerated growth and accompaning pore entrapment. Increasing additions result in more precipitates thus restricting the ultimate grain size by pinning of the boundaries. The specific gravity fell from 99.1% to 95.0% theoretical , indicating that more pores were entrapped within the grains due to fewer grain boundaries sweeping a given grain.

Grain growth in CaO doped with Ta_2O_5 exhibited a duplex structure typical of exaggerated grain growth. The progress of the exaggerated grain growth process was more advanced in the 0.5% Ta_2O_5 material (compare Figures 4-7a and b). This indicates that the grain boundary mobility is slowed with increased Ta_2O_5. No extensive Ta rich precipitates were found in the CaO specimens indicating that, at the additive levels investigated, the Ta_2O_5 is soluble in the CaO. Thus in CaO the grain growth is controlled by soluble impurity "atmospheres" at the grain boundaries.

4.1.5. TiO_2 Doped MgO and CaO

Phase equilibria data indicates that no liquid would be expected in either of these systems below 1740°C. Titanate compound formation is possible in both systems, however, the solubility limits are unknown.

TiO_2 additions up to 6.6% resulted in increased grain sizes in both MgO and CaO (Table 4-1). Both oxides exhibited decreasing grain sizes with increased additions (Figure 4-8). Pinning of grain boundaries by titanate compounds could account for the latter effect as increased precipitation will result from increased additions.

Detailed study of the CaO and MgO microstructures produced reveals extensive second phase particles at the grain boundaries.

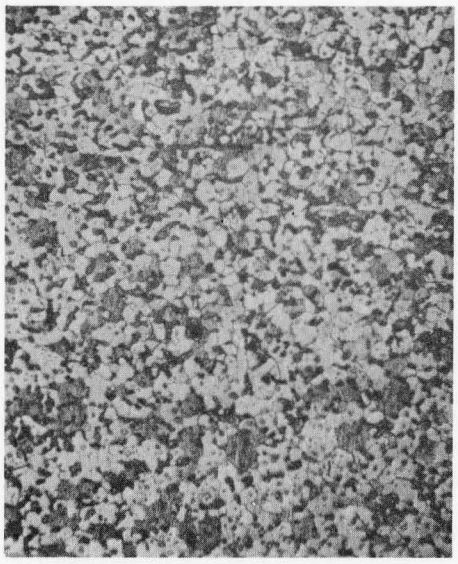

Figure 4-7a

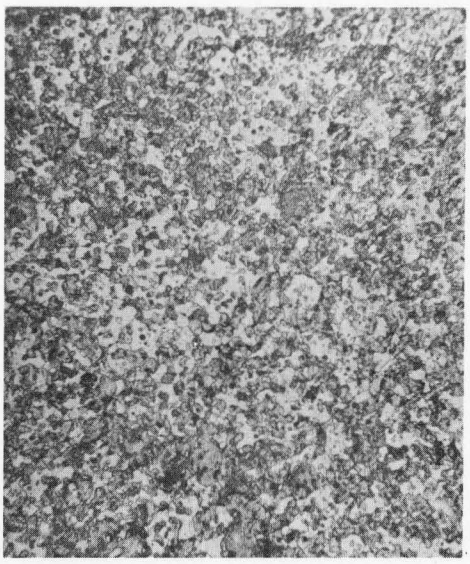

Figure 4-7b

Grain size of CaO doped with a) 0.5%, b) 2% Ta_2O_5.
(Etched 4% Picric Acid in Ethanol, 125x)

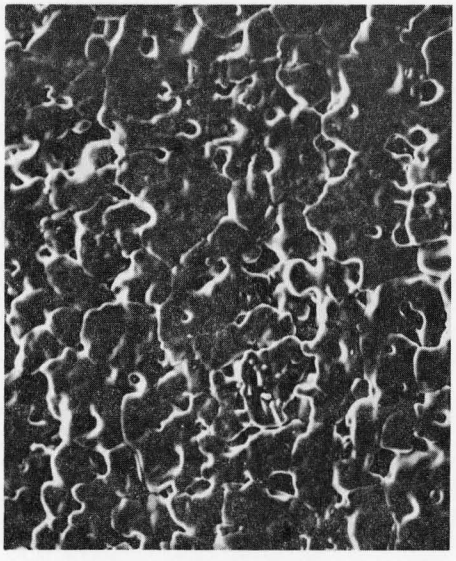

Figure 4-8a

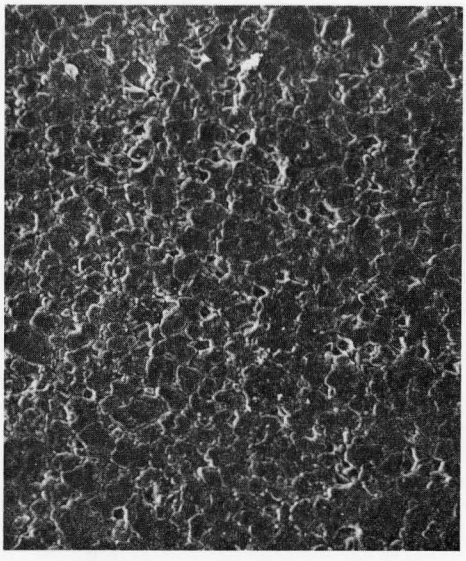

Figure 4-8b

Grain size of CaO doped with a) 1%, b) 5% TiO_2.
(Thermally etched a) 220x, b) 120x)

Examination of these with the Xray dispersive analyser on the SEM indicated that these precipitates were high in titanium in both MgO and CaO (Figures 4-9a and 4-10).

From Table 4-1 it is evident that the addition of TiO_2 resulted in high sintered densities for both oxides. This enhanced sintering in the TiO_2 - MgO system has been previously noted (Section 2.6.4.). Both this and the increased grain size could be due to the solution of Ti^{+4} ions in the oxides forming a defect structure via:

$$TiO_2 \rightarrow Ti^{+4} + V'_{Mg} + O^{-2}$$

$$TiO_2 \rightarrow Ti^{+4} + V_{Ca} + O^{-2}$$

This would increase the rate of cation diffusion, which is the slow moving species in MgO (the oxygen anions are transported on the grain boundaries while the cations migrate by volume diffusion). If the defect solution formed by titania is extensive then the precipitates will appear only during cooling and the reduction of grain size with increased addition must be due to the grain boundary atmosphere drag effect. The discrete nature of the precipitates implies nothing about the distribution at high temperatures for the reasons previously discussed. Again here the CaO-TiO_2 phase diagram provides no information below 30% CaO so that no definite conclusions may be drawn from it.

4.1.6. SiO_2 Doped MgO and CaO

Additions of 0.5% SiO_2 to MgO produced exaggerated growth and no improvement in sintered density. Similar additions to CaO resulted in poor sintered densities.

The SiO_2 had very little effect on the grain size of the MgO at all addition levels. It is noteable that two of the specimens (1.0% and 2.0% SiO_2) exhibited a duplex grain size distribution (Figure 4-12) indicating that exaggerated growth was in progress.

Micrographs and X-ray maps obtained on the SEM showed (Figures 4-13a, b) that the silica was concentrated around pores in the MgO.

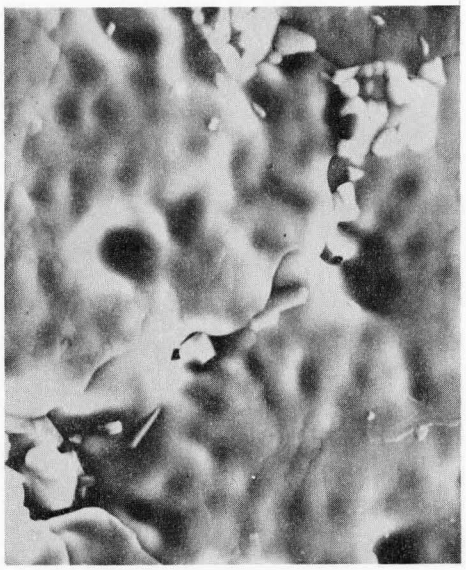

Figure 4-9a

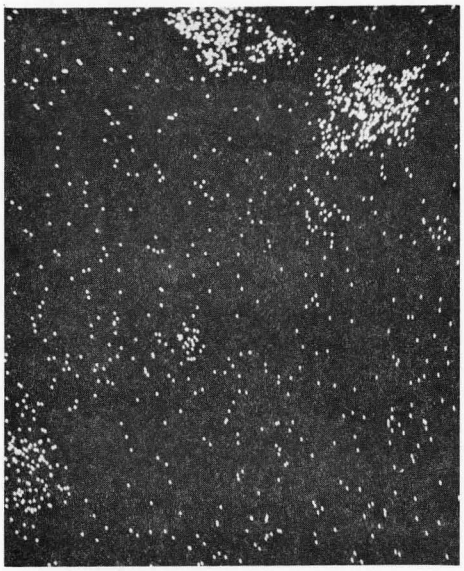

Figure 4-9b

SEM photo (a) and Ti X-ray map (b) of MgO doped with 1% TiO_2 showing Ti rich precipitates. (1380x)

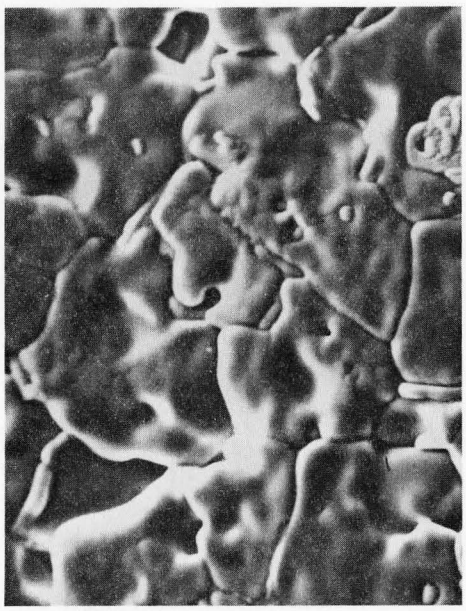

Figure 4-10a

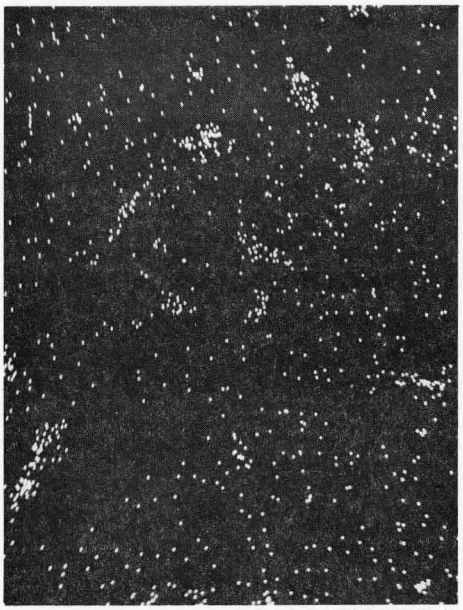

Figure 4-10b

SEM photo (a) and Ti X-ray map (b) of CaO doped with 2% TiO_2 showing Ti rich second phase. (600x)

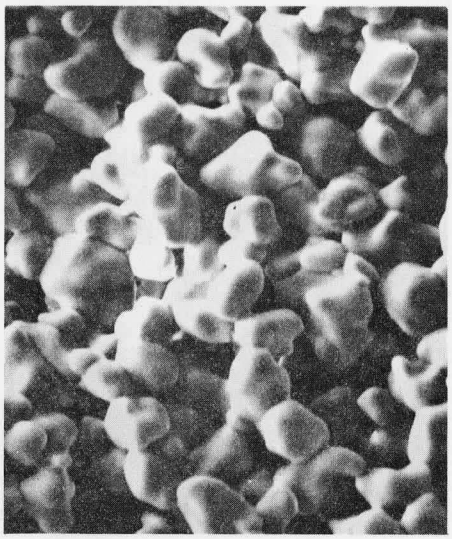

Figure 4-11a

CaO doped with .5% SiO_2
Thermally etched (600x)

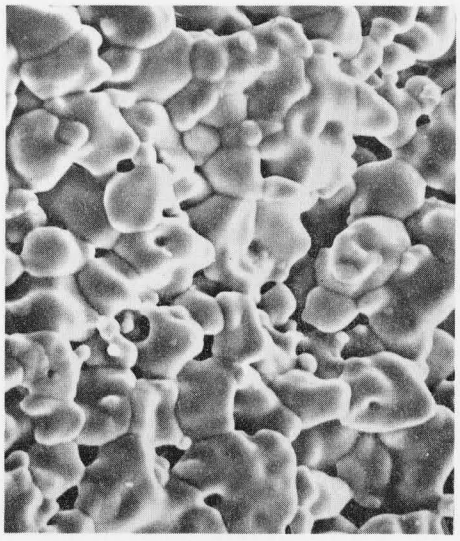

Figure 4-11b

CaO doped with 5% SiO_2
Thermally etched (560x)

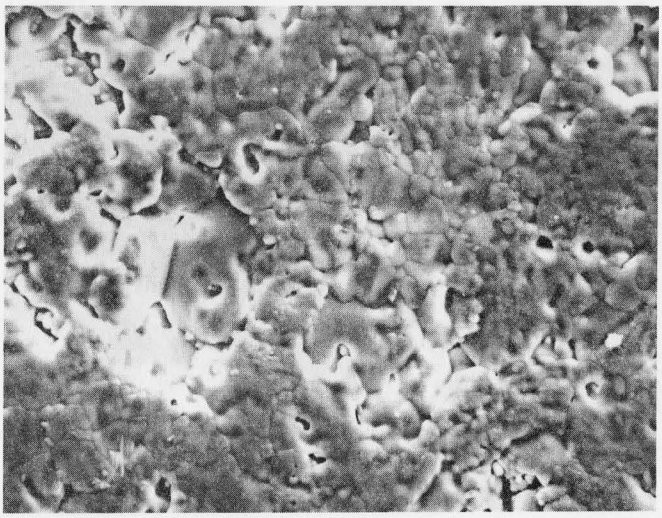

Figure 4-12 MgO doped with 1% SiO_2
Thermally etched (610x)
Showing duplex grain size.

This is due to the reaction between MgO and SiO_2 to form forsterite (Mg_2SiO_4). At sintering temperatures this phase is slightly soluble in MgO, (Figure 2-12). The reaction between MgO and SiO_2 is known to proceed slowly so the MgO particles will have sintered considerably around these inclusions. Hence the solution process leaves a void as observed. The 6.0% solubility of forsterite in MgO at 1600°C allows sintering to proceed to normal levels. Thus silica additions result in little change in the sintered density and grain size obtained.

Silica additions to CaO resulted in extremely low sintered densities (Table 4-1, Figure 4-11). Density and specific gravity measurement indicate that all the porosity is connected to the surface at all silica levels. Micrographs and X-ray maps (Figure 4-14) show the presence of Si concentrations in the CaO. From the phase diagram (Figure 2-11) 1.0% SiO_2 results in 4.3% $3CaOSiO_2$ formation at inter-oxide contact points (upon cooling this reverts to Ca_2SiO_2 + CaO at 1250°C). This process is analogous to that occuring in MgO, however the interoxide compounds appear more stable in the CaO-SiO_2 system and, rather than dissolving and allowing sintering to proceed, diffusion is much redueed at the interoxide contact points and normal shrinkage and densification prevented.

4.1.7. WO_3 Doped CaO and MgO

Addition of 0.2% and 2.0% WO_3 to MgO produced a marked inhibition of grain growth. The increased additions resulted in a refinement of the grain size with 0.2% addition yielding a grain size of 25 μm and a 1% addition 13 μm (Figure 4-15). Specific gravity measurements confirmed previous work (Section 2.6.7.) that WO_3 is not an effective sintering aid for MgO. Due to the fine grain size, the absence of optical evidence of liquid phase is not conclusive proof of its absence. Phase equilibria indicates that 2.0% liquid may form, however no data on solubility below 10% WO_3 is available in the literature. It is probable that considerable

Figure 4-13a

MgO doped with 5% SiO_2
Thermally etched (1300x)

Figure 4-13b

Si x-ray map shows concentration of Si about pore.

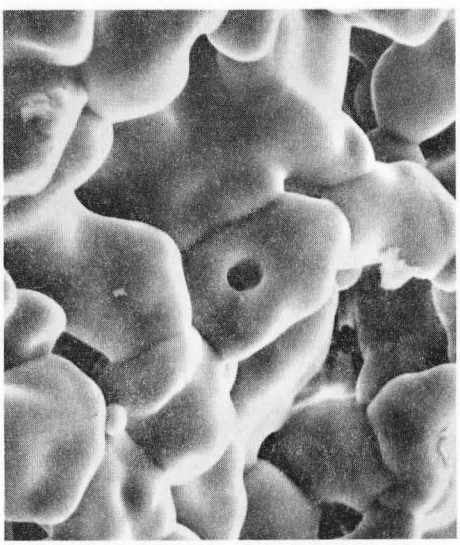

Figure 4-14a

CaO doped with 5% SiO_2
Thermally etched (1120x)

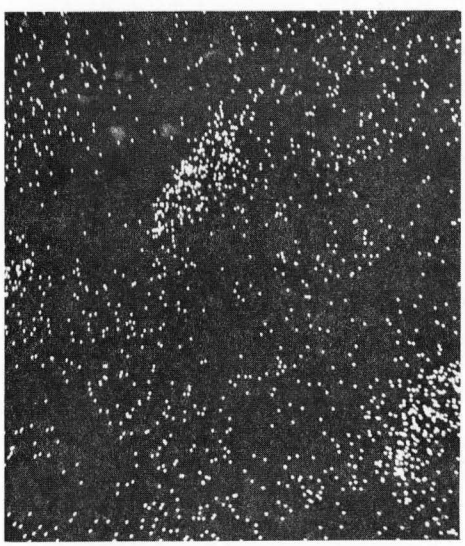

Figure 4-14b

Si x-ray may shows Si concentration.

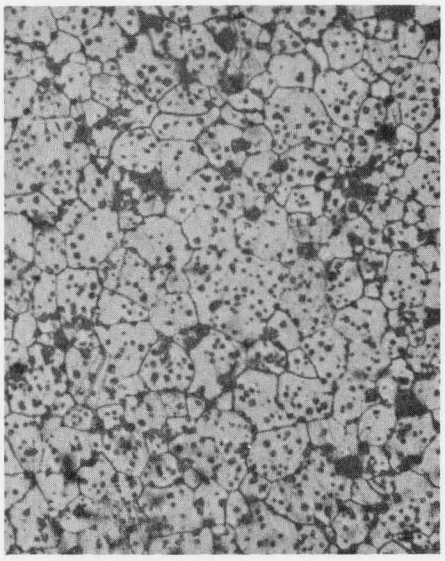

Figure 4-15a

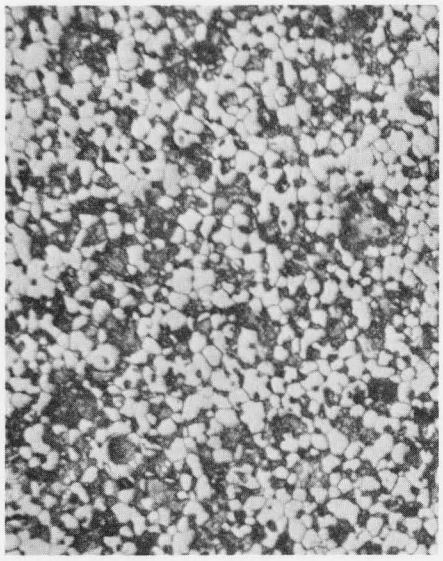

Figure 4-15b

MgO doped with a) 0.5% WO_3, b) 2% WO_3 showing reduced grain size with increased addition. (Etched in 50% HNO_3, 250x)

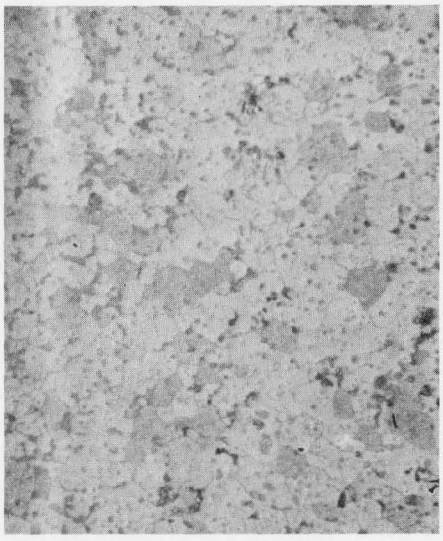

Figure 4-16a

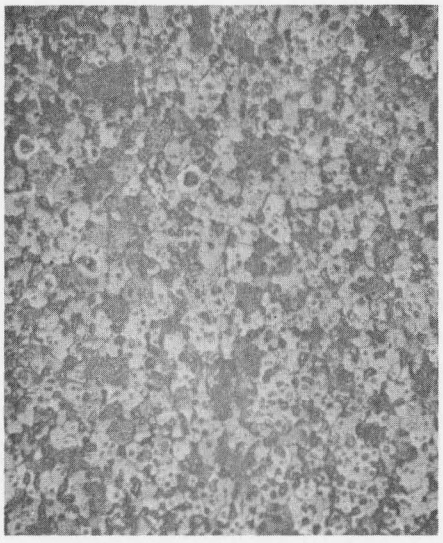

Figure 4-16b

CaO doped with a) 0.5% WO_3, b) 2% WO_3 showing reduced grain size with increased addition. (Etched 4% Picric Acid in Ethanol 125x)

WO_3 was lost by vapourization during the soak at 1700°C which is 343°C above the sublimation temperature quoted by G.V. Samsonov in "The Oxide Handbook"*. The volatility of the oxide would allow coating of the MgO particles with WO_3 and the inhibition of sintering by blocking of diffusion paths.

In CaO additions of WO_3 resulted in increased sintered density and grain size (Table 4-1, Figure 4-16). The presence of entrapped porosity indicates that exaggerated grain growth occurred. However increased additions resulted in decreased grain sizes suggesting the presence of insoluble grain boudnary precipitates.

4.1.8. GeO_2 Doped MgO and CaO

Addition of GeO_2 to CaO and MgO resulted in increasing grain growth with increased additions (Table 4-1, Figures 4-17, 18). Both the micrographs showed intragranular porosity indicating exaggerated grain growth. In the MgO there was a significant fraction open porosity and no increase in bulk density over the undoped material.

The increase in grain size with increased addition in both oxides cannot be attributed to the formation of a liquid phase as for the V_2O_5 doped material as the phase equilibrium indicates (Section 2.6.8.) refractory phases. This is in agreement with the lack of microscopic evidence of a liquid phase.

It is possible that this indicates that the GeO_2 dissolves in the MgO and CaO creating cation vacancies which increase the sintering and grain growth rates.

4.1.9. Fe_2O_3 Doped MgO and CaO

Both MgO and CaO exhibited increasing grain growth with increased additions of Fe_2O_3 (Table 4-1). The behavior of CaO can be interpreted as the result of liquid formation at the grain boundaries.

* Plenum Press, N.Y., 1973.

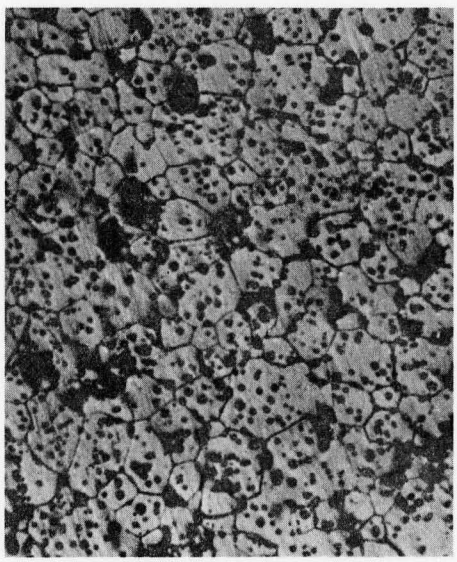

Figure 4-17a

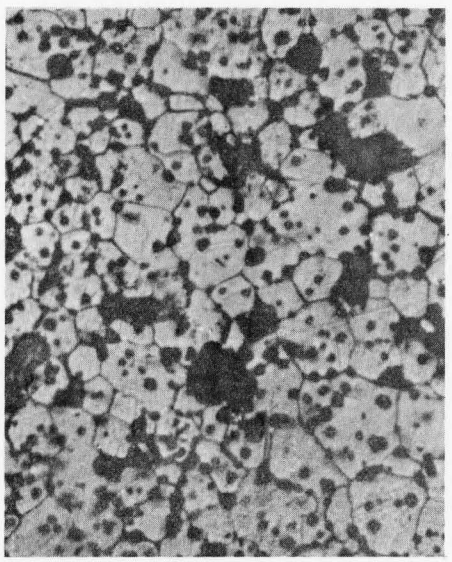

Figure 4-17b

MgO doped with a) 0.4%, b) 2% GeO_2.
(Etched 50% HNO_3, 250x)

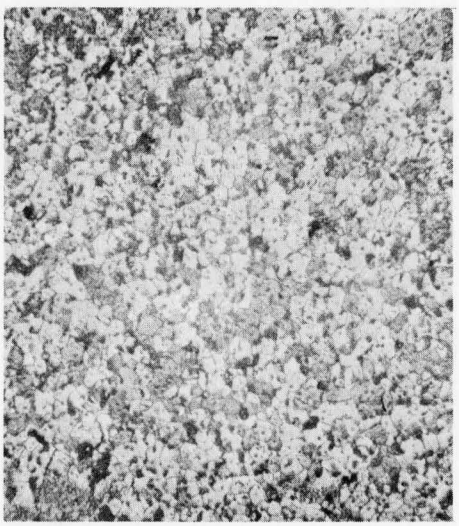

Figure 4-18a

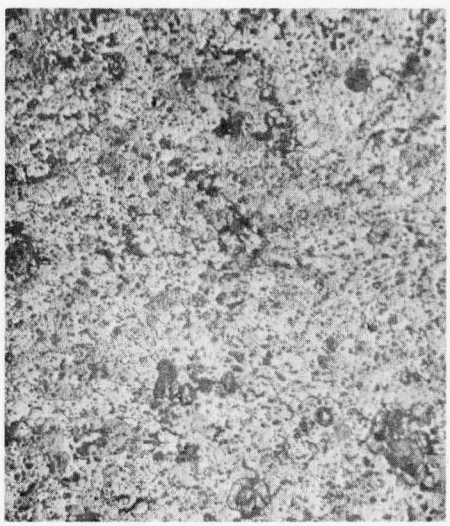

Figure 4-18b

CaO doped with a) 0.4%, b) 2% GeO_2.
(Etched with 4% Picric Acid in Ethanol, 125x.)

Evidence of the existence of liquid at the sintering temperatures may be seen in Figures 4-19a and b. This liquid would not be present if the iron ions were reduced to the divalent state as a defectless solid solution would be expected (Figure 2-15a). Thus in the oxidizing atmosphere in which sintering was carried out some fraction of trivalent iron ions was retained. If all of the iron was trivalent then a 1.0% addition of Fe_2O_3 would result in 1.6% liquid content at 1700°C from phase diagram (Figure 2-15b). Such liquid content uniformly distributed would allow the attainment of high sintered density by the mechanisms of liquid phase sintering described previously. Increased grain growth is also to be expected.

$MgO.Fe_2O_3$ phase equilibria consideration indicate that if the iron ions are entirely divalent a defectless magnesiowustite solid solution would form. However in an oxidizing atmosphere this is again not likely and the fraction trivalent iron formed will promote sintering. In this case no liquid formation is expected, rather the trivalent iron ions will disolve in the MgO and create cation vacancies via:

$$Fe_2O_3 = 2Fe^{+3} + 3O^{-2} + V_{Mg}$$

Examination of the microstructures produced in this series of firings showed the presence of a grain boundary phase (Figure 4-21). X-ray analysis of this phase on the SEM showed a surprisingly high Ca content. This indicates that the low levels of CaO native to the MgO was strongly segregated to the grain boundaries where it formed a low melting liquid. This segregation is in agreement with results reported previously by Leipold (12,13).

It is unlikely however that the liquid so formed could account for the increased grain growth observed in the MgO and the phenomenon must therefore be attributed to the magnesioferrite defect structure produced by the trivalent iron.

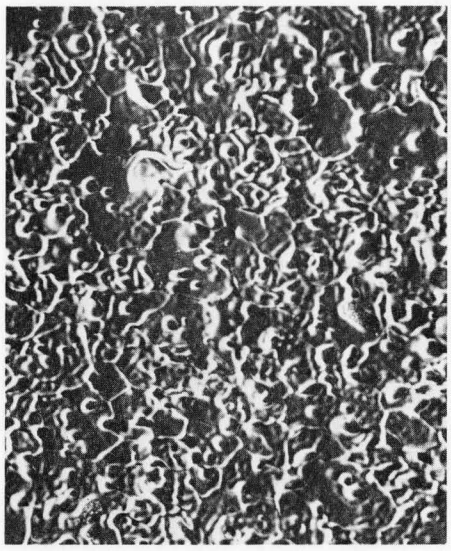

Figure 4-19a

Figure 4-19b

CaO grain size doped with a) 0.5% Fe_2O_3 b) 5% Fe_2O_3.
Evidence of crystaline grain boundary phase in b.
(Thermally etched. a) 120x, b) 88x)

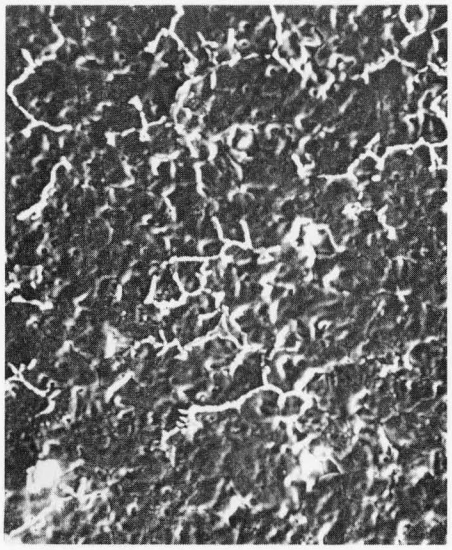

Figure 4-20a

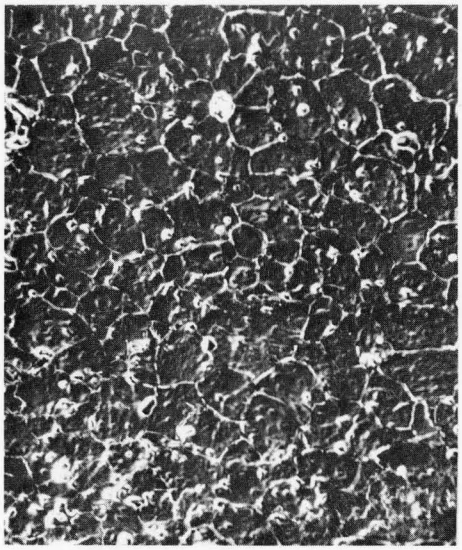

Figure 4-20b

MgO grain size when doped with a) 0.5% Fe_2O_3 b) 5% Fe_2O_3.
Evidence of grain boundary $MgO \cdot Fe_2O_3$ can be seen in both.
(Thermally etched. a) 280x, b) 150x)

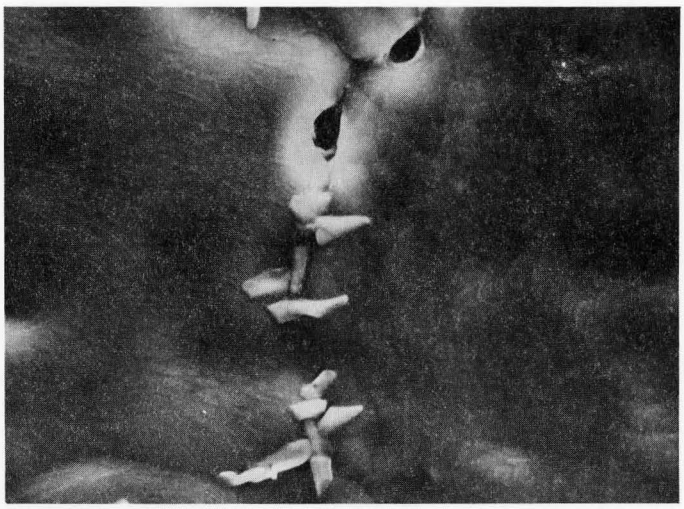

Figure 4-21 MgO doped with 2% Fe_2O_3 showing grain boundary phase.
Thermally etched. (7000x)

X-ray analysis of the matrix and grain boundary phase were done in the SEM with these results:

Phase	Element	Centroid	Area
Matrix MgO	Mg	1.21	35768
	Fe	6.35	3342
Precipitate	Mg	1.21	19649
	Ca	3.65	6119
	Fe	6.35	5119

4.2. Microstructures of Magdols

4.2.1. Introduction

Throughout the following discussion a short form notation will be used to identify the MgO content, dopant and test temperature (where relevant). For example, "4MTi13" refers to a 40 percent MgO magdol containing 1% TiO_2 (only 1% additions were made in each case) tested at 1300°C.

The symbols identifying the dopants have the following meanings:

P	no dopants intentionally added
Ti	1.0 weight percent TiO_2
Ta	1.0 weight percent Ta_2O_5
Fe	1.0 weight percent Fe_2O_3
V	1.0 weight percent V_2O_5
Si	1.0 weight percent SiO_2
W	1.0 weight percent WO_3
Ge	1.0 weight percent GeO_2

The density and grain size measurements are summarized in Table 4-2. It can be seen that the additives fall into two groups, those that increase the bulk density and grain size (TiO_2, Fe_2O_3) and those which have little effect (SiO_2, Ta_2O_5, GeO_2). However detailed examination indicates that different mechanisms may operate in these systems. Common characteristics are, the increase in density with increased MgO content (undoped, SiO_2,

Table 4-2

Microstructure of Magdols

Sample	Grain Size MgO (μm)	Grain Size CaO (μm)	% Theoretical Bulk Density	% Theoretical Specific Gravity
4MP	8	19	83.9	97.3
6MP	14+	33+	83.0	98.6
8MP	9	--*	89.8	95.9
4MSi	15	16	84.1	98.2
6MSi	17	18	88.2	97.2
8MSi	16	16	87.7	98.3
4MTi	14	24	90.3	94.7
6MTi	10	14	90.2	94.0
8MTi	17	29	88.4	93.6
4MTa**	7+	18+	80.3	98.8
6MTa**	11+	16+	83.0	98.8
8MTa**	7	10	87.5	96.5
4MFe	19	22	96.4	96.5
6MFe	18	15	95.7	96.7
6MGe**	22	20	80.1	--
8MGe**	--	--	84.7	--
6MV**	12	17	90.0	--

* Not determined but larger than MgO.

** Determined from polished and chemically etched sections, others thermally etched.

\+ Relatively poorer estimate.

Ta_2O_5 and GeO_2 doped materials) and the general reduction of bulk density for the mixed oxides compared to the separate oxides. This latter effect can be attributed (Section 2.3.3.) to the low solubility of CaO and MgO inhibiting sintering at mixed oxide contacts.

The results of microstructural analysis of all dopants are presented in Table 4-2 and discussed in the subsequent sections.

4.2.2. Microstructure of the Undoped Materials

The microstructure of the pure materials as revealed by polishing and thermally etching at 1500°C are shown for 40%, 60% and 80% MgO in Figures 4-22, 4-23 and 4-24 respectively. The fact that the CaO grain size is much larger than that of the MgO is readily apparent. Measurements of the grain sizes of each phase are presented in Table 4-2 along with the bulk density and specific gravity data. The density values presented are usually based upon at least two measurements or different samples.

It is interesting that the topology of the MgO and CaO are different following thermal etching. The MgO grains retain a flat face from the polishing wheel while the CaO is more rounded. The hollows and crevices about the CaO grains are artifacts of the thermal etching process rather than a significant feature of the microstructure as determined by comparison of polished sections before and after etching.

The CaO and MgO grains are both gathered into clusters of individual grains as can be seen in Figures 4-22,4-23. Often in the literature

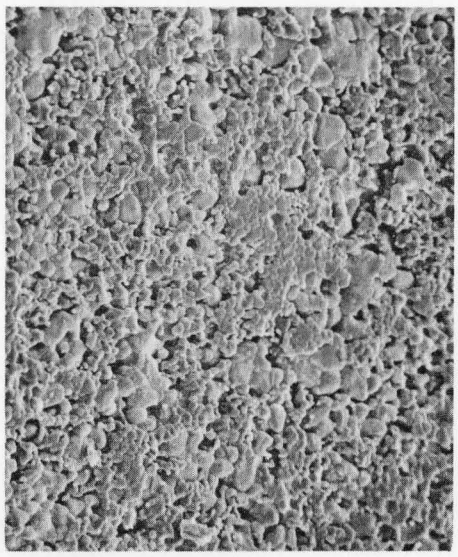

Figure 4-22a

Microstructure of 40% MgO undoped (260x, thermally etched at 1500°C).

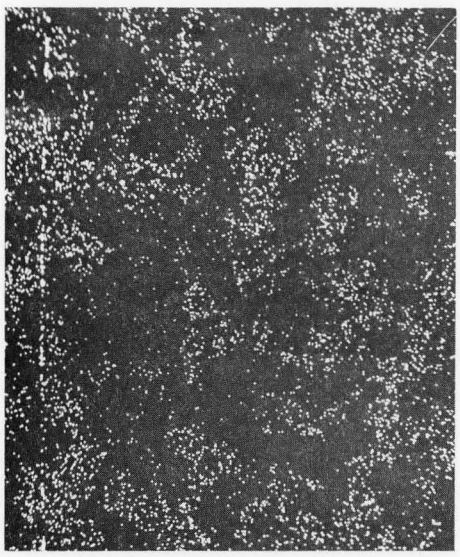

Figure 4-22b

Ca x-ray map.

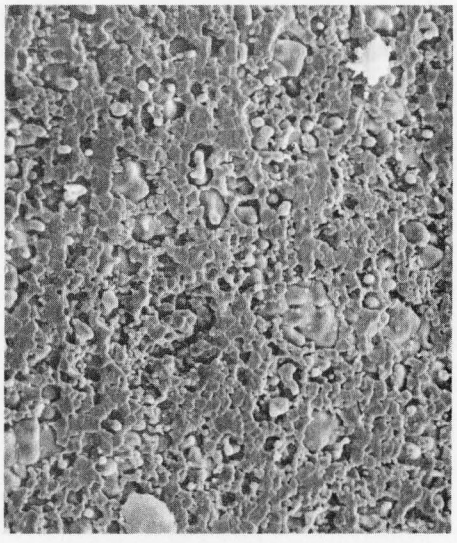

Figure 4-23a

Microstructure of 60% MgO undoped (235x, thermally etched at 1500°C).

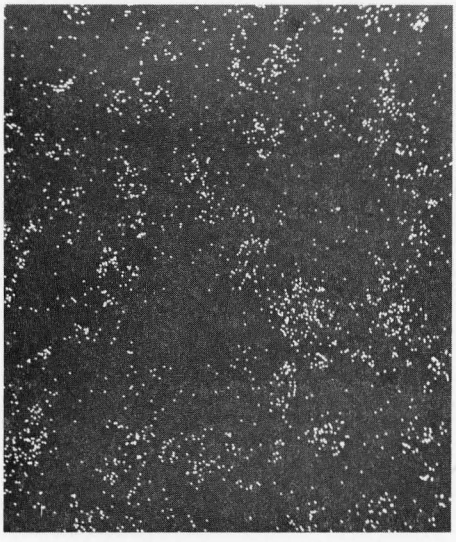

Figure 4-23b

Ca map showing encapsulation of CaO phase by continuous MgO.

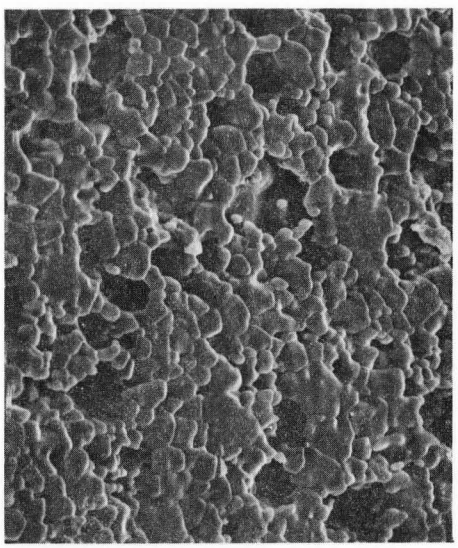

Figure 4-24

Microstructure of 8 MP
(560x - thermally etched)
Note clusters of MgO grains.

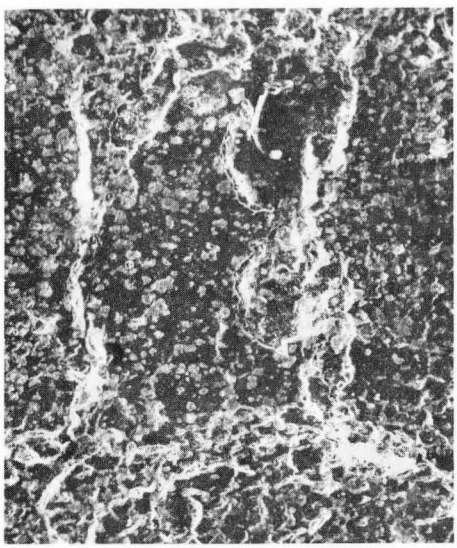

Figure 4-26

Microstructure of 8 MSi showing network of fine cracks due to $3CaO \cdot SiO_2$ reversion. (63x - thermally etched)

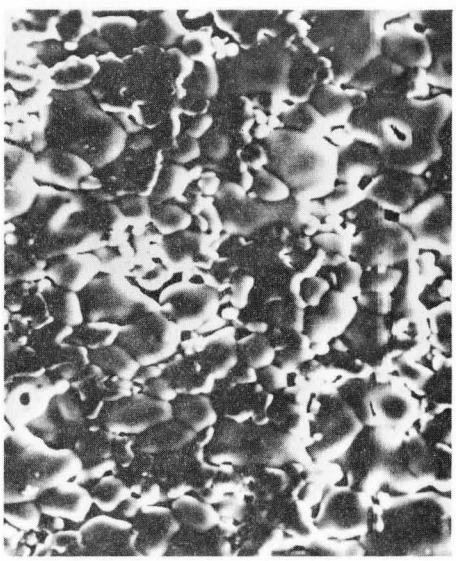

Figure 4-25a

4MSi microstructure light phase is CaO, dark MgO.
(570x - thermally etched)

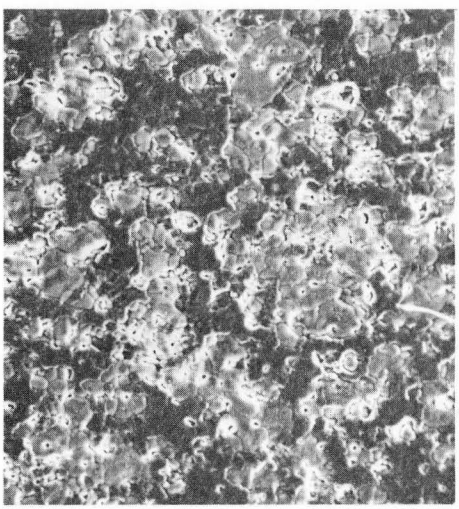

Figure 4-25b

6MSi microstructure.
Note clustering of MgO and CaO grains. (240x - thermally etched)

it is the size of this cluster which is reported as grain size, since polishing and etching procedures do not easily reveal the individual grain boundaries.

Examination of the microstructure also shows no indication of any non equiaxed structure as is expected since both MgO and CaO are cubic structures.

The density data presented in Table 4-2 indicates that sintering is not past the intermediate stage as in the case of the 4MP and 6MP compositions, over 80% of the porosity is connected to the surface and for the 8MP, over 50% is connected. It is interesting to note that the bulk density and specific gravity data for the former compositons are close to those of pure CaO while the 8MP data resembles that of pure MgO.

The trends of sintered densities are similar to those obtained by Kriek et al. (19) at 1550°C (Figure 2-4, Section 2.3.3.), however the purities of their materials were not specified so comparison is difficult.

Due to the distributions of grain sizes between the CaO and MgO the CaO cannot be considered continuous even at the 60% level. Unfortunately due to the highly porous structure it was not practical to follow Busit's procedure and quantitatively measure the relative extent of mixed phase interfaces.

4.2.3. Effect of SiO_2 on Magdol Microstructure

This set of microstructures is remarkable for their uniformity of grain sizes of CaO and MgO in all three compositions. From the bulk density data it is evident that sintering was not highly advanced and a large proportion of open porosity was present. This pore distribution is similar to that of the undoped magdols.

CaO has probably prevented the sintering of the MgO due to its low solubility as discussed previously in Section 2.3.3.

The polished and thermally etched microstructures of 4MS and 6MS are presented in Figure 4-25. X-ray mapping on the SEM failed to show any concentration of silica as were found in the separate oxides, however this is most likely due to the low concentration and atomic number rather than the absence of such concentrations. It would be expected that a refractory calcium silicate would form rather than magnesium silicates based on the bonding phases observed in basic refractories (Gilpin (2)).

In all of these samples a number of fine cracks were observed following polishing. The surface of the 8MS sample is shown in Figure 4-26 where it can be seen that the cracks are closely spaced. It is likely that these cracks are a result of the decomposition of $3CaO{\cdot}SiO_2$ to $2CaO{\cdot}SiO_2$ and CaO at 1250°C and the structural change of the $2CaO{\cdot}SiO_2$ during cooling (Section 2.6.2.). Such a network of cracks might be expected to substantially reduce the fracture strength of the material. However the cracking may also provide a toughening mechanism in the form

of a microcrack zone capable of dissipating energy at the crack tip (see Section 2.7.4.).

4.2.4. Effects of 1% TiO_2 on Magdol Microstructures

The grain sizes and fired densities of 4MTi, 6MTi and 8MTi are presented in Table 4-2. The most striking features of these results are first that the grain size spread between the MgO and CaO phases is much reduced and the bulk density is much higher in the 40% and 60% MgO compositions, with a higher degree of closed porosity.

The undoped mixtures show a maximum grain size for both MgO and CaO at 60% MgO while the opposite is the case for the TiO_2 doped material. This would seem to indicate that the TiO_2 has a greater influence on the contact points between unlike particles than on those between like particles in view of the fact that a maximum in the number of unlike contacts will occur at 54 wt% MgO (assuming uniform particle size).

Observations of the microstructures (Figures 4-27 to 4-29) indicate that the morphology of the MgO and CaO was essentially the same as that found in the undoped material as the CaO grains were again more rounded than the MgO.

The more uniform grain size of the MgO and CaO results in a more nearly continuous CaO phase in 4MTi than 4MP.

Unlike the preliminary experiments with CaO and MgO individually, no evidence of a TiO_2 rich phase was found using the x-ray analyser on the SEM. This may, however, be due to the roughness of the etched surface

Figure 4-27a

4 MTi microstructure
(250x - thermally etched
at 1500°C).

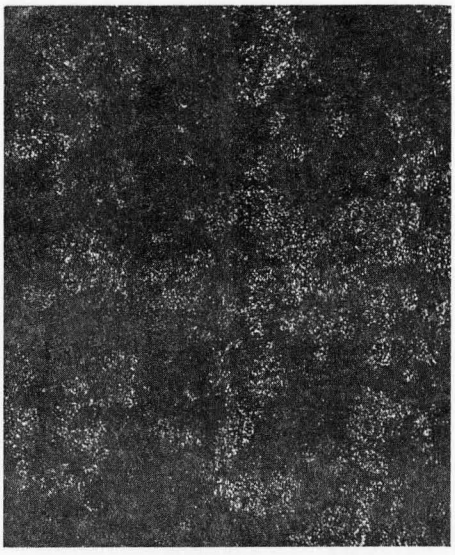

Figure 4-27b

4 MTi Ca x-ray map.

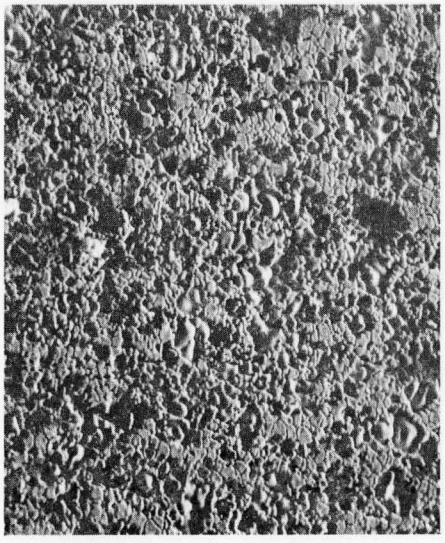

Figure 4-28a

6 MTi microstructure
(200x - thermally etched)
CaO phase is well encapsellated

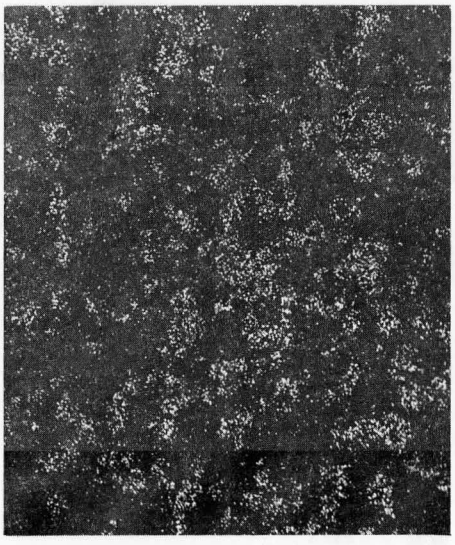

Figure 4-28b

Ca x-ray map.

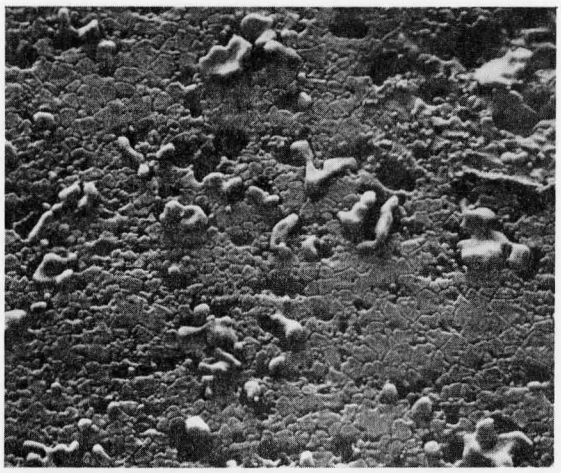

Figure 4-29

8 MTi microstructure
Flat grains are MgO.
Rounded grains are CaO.
(225x - thermally etched)

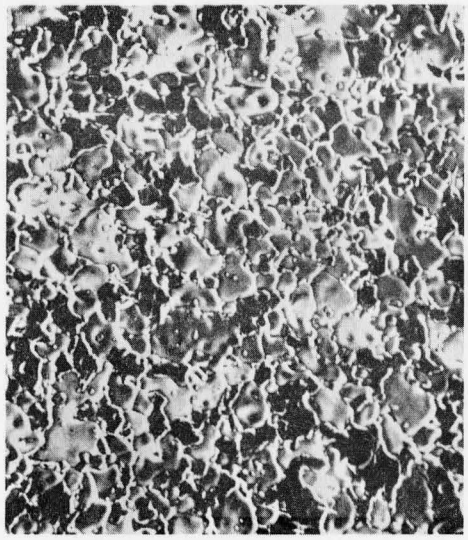

Figure 4-30

4MFe microstructure.
Light grey CaO, dark grey MgO.
(230x - thermally etched)

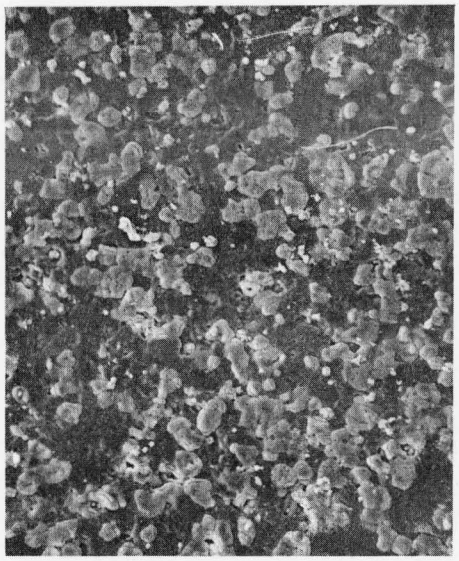

Figure 4-32

6MFe microstructure.
(230x - thermally etched)

which reduces the sensitivity of the analyser. It is also apparent that the grain sizesin the 40MTi and 80MTi material were increased over the undoped 40MP and 80MP, although not nearly to the extent found in the two phase system where the second major phase inhibits grain growth.

4.2.5. Effect of Fe_2O_3 on Microstructure of Magdols

Magdol compositions of 40% and 80% MgO with 1% addition of Fe_2O_3 were the only compositions examined. These materials exhibited a very high degree of densification and revealed, upon polishing and etching, CaO and MgO grain sizes which were virtually identical. The distribution of the MgO and CaO can be seen in Figures 4-30 to 4-32. A nearly continuous MgO matrix exists in the 6MFe with the morphology of the thermally etched CaO and MgO grains being quite different from the undoped material. This can be attributed to the formation of a small amount of a wetting liquid at the grain boundaries during firing to 1700°C as would be expected from the phase diagrams (Section 2.6.3.).

Detailed examination of the thermally etched 4MFe material revealed pockets of a third phase located at triple points and between the CaO grains but not between the MgO grains (Figure 4-31). X-ray analysis indicated concentrations of Mg, Ca and Fe. The presence of these pockets of low melting materials is expected to have a catastrophic effect on the hot strength of these materials.

It is possible that the melting point is as low as 1200°C (in the $CaO{\cdot}Fe_2O_3$ system) and native Na_2O may well act as a further flux.

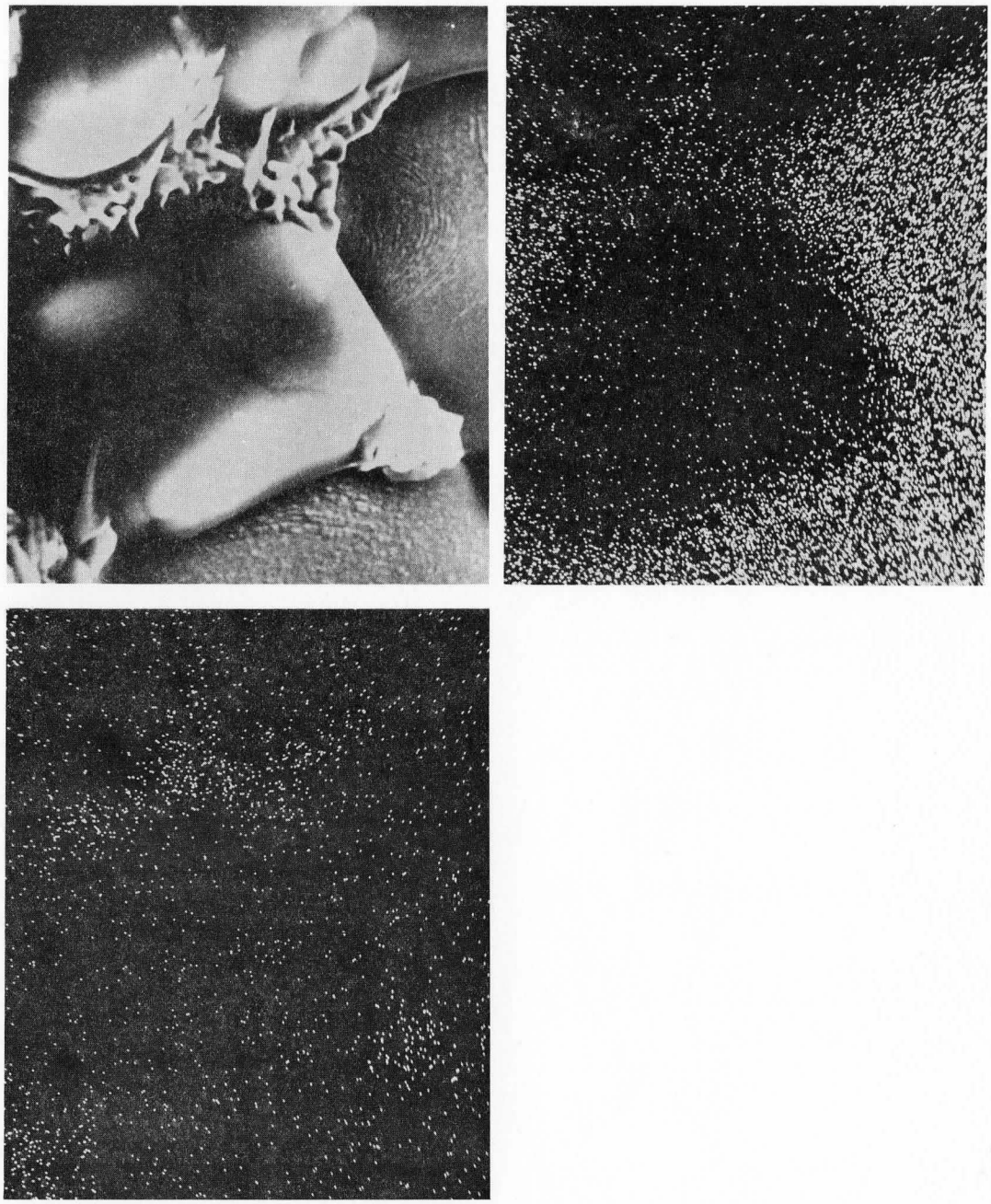

Figure 4-31 a) 4MFe showing intergranular phase.
(5800x - thermally etched)
b) Ca x-ray map.
c) Fe x-ray map.

4.2.6. Effect of Ta_2O_5 on Magdol Microstructure

The microstructure and density characteristics of this material are remarkable in their close similarity to those of the undoped material. The 4MTa (Figure 4-33) in particular is virtually identical to 4MP. With increasing MgO, both the Ta_2O_5 doped and undoped magdols exhibit larger grain sizes at 60% MgO and a diminished grain sizes at 80% MgO. These results are disappointing in view of the large difference in behavior observed in the CaO and MgO doped separately (Section 4.1.4). As found in the previously discussed work, Ta_2O_5 doping did not result in increased density and is not an effective sintering agent for the mixed oxides. The reasons for this may involve the formation of refractory tantalate phases with the CaO.

Since the CaO cannot then densify, the MgO dispersed in the magdol is also prevented from densifying.

4.2.7. Effect of GeO_2 on Magdol Microstructure

The magdols doped with 1% GeO_2 showed exceptionally poor sintered densities of 80% theoretical for 6MGe and 85% for 8MGe. This is likely due to the formation of refractory interoxide compounds which prevent sintering. In view of these results and those previously discussed in the grain growth and sintering of the single oxides work on this additive was terminated. Two samples of the 8MGe material were fracture tested inadvertently and the results are recorded in Tables 4-3 and 4-4 but not discussed.

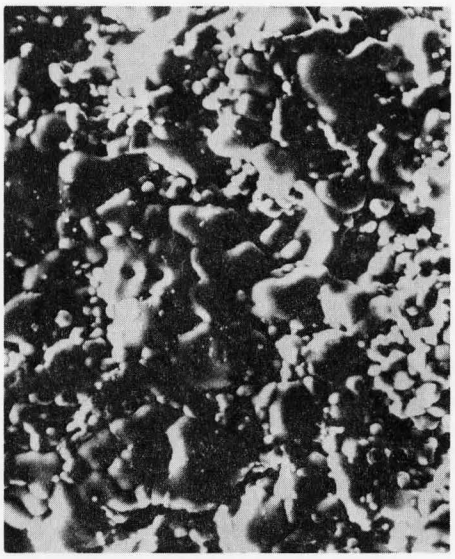

Figure 4-33a

4 MTa microstructure
(570x - thermally etched)

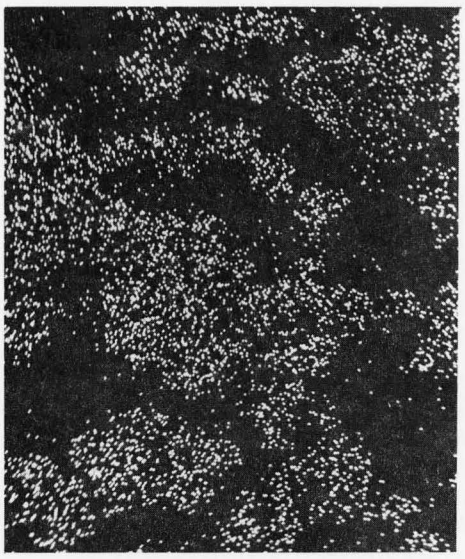

Figure 4-33b

4 MTa Ca x-ray map.

4.3. Fracture Toughness Measurements

4.3.1. Summary of Results

The fracture tests completed are listed in Table 4-3. The K_{1C} values calculated for these tests are presented in Table 4-4. Statistical analysis of the differences due to testing temperature were done for each additive using the Students t test (Appendix II) at the 90, 95, 98, 99 and 99.9 confidence level. The highest confidence level is reported in Table 4-5. A table of estimates of the fraction intergranular fracture for each temperature dopant combination is presented in Table 4-6. Additional significance tests between each dopant-temperature combination and the corresponding undoped results are presented in Table 4-7.

In this section each additive is first discussed in detail followed by a discussion of features common to several dopants.

4.3.2. Fracture Behavior of Undoped Magdols

The temperature dependence of K_{1C} of the 40%, 60% and 80% MgO compositions is shown in Figures 4-34 to 4-36. It is apparent that there is a large difference between the 4MP and the magdols with higher MgO content.

The 4MP shows a K_{1C}-temperature dependence similar to that of porous Al_2O_3 (Figure 2-34) and to that of high density MgO (Figure 2-32). It is interesting to note that there is a statistically significant increase in K_{1C} at 600°C which was not observed in dense MgO. This may reflect an increase in the fraction of intergranular fracture.

Table 4-3

Summary of Fracture Tests

MgO Content	Temp. °C	1% Additive				
		None	Fe_2O_3	SiO_2	TiO_2	Ta_2O_5
40%	20	4*				
	600	3				
	1100	3			3	
	1300	8	4	4	7	3
	1500	4				
60%	20	3	3	3		2
	600	3	3	3		3
	1100	5	6	6	4	6
	1300	6	6	7	6	4
	1500	5	3	6	2	6
80%	1100	2				
	1300	5		1	6	3
	1500	3				1
Others	80% MgO 1% GeO_2 1300°C (2)					

* Numerals are the numbers of tests done for the temperature–dopant combinations and which meet the conditions outlined in Appendix II.

Table 4-4

Summary of K_{1C} Results *** ($MN/m^{3/2}$)

Specimen	Test Temperature °C				
	20	600	1100	1300	1500
4MP	$.560^{+}_{-}.092$	$.715^{+}_{-}.040$	$.657^{+}_{-}.083$	$.542^{+}_{-}.130$	$.398^{+}_{-}.139$
6MP	$.734^{+}_{-}.274$	$.600^{+}_{-}.317$	$.625^{+}_{-}.057$	$1.194^{+}_{-}.147$	$.329^{+}_{-}.083$
8MP			$1.076^{+}_{-}.003$	$1.393^{+}_{-}.313$	$.204^{+}_{-}.079$
4MSi				$.674^{+}_{-}.129$	
6MSi	$.717^{+}_{-}.081$	$.732^{+}_{-}.105$	$.684^{+}_{-}.104$	$.884^{+}_{-}.151$	$.829^{+}_{-}.082$
8MSi				$.789^{*}$	
4MTi			$1.155^{+}_{-}.172$	$1.239^{+}_{-}.276$	
6MTi			$1.322^{+}_{-}.326$	$1.038^{+}_{-}.201$	$.472^{+}_{-}.186$
8MTi				$1.041^{+}_{-}.067$	
4MTa				$.936^{+}_{-}.172$	
6MTa	$.773^{+}_{-}.025$	$.940^{+}_{-}.168$	$1.021^{+}_{-}.217$	$1.117^{+}_{-}.044$	$.801^{+}_{-}.101$
8MTa				$1.014^{+}_{-}.218$	$.785^{*}$
4MFe				$.641^{+}_{-}.106$	
6MFe	$.873^{+}_{-}.103$	$.948^{+}_{-}.065$	$.677^{+}_{-}.219$	$.780^{+}_{-}.113$	$.374^{+}_{-}.251$
8MGe				$.948^{+}_{-}.173$	
6MV				$\sim 0.0^{**}$	

* 1 sample

** 2 samples

*** As discussed in Appendix II more digits are carried for purposes of statistical analysis than are experimentally significant.

Table 4-5

Significance of the differences between room temperature and elevated temperature results by additive for magdols.*

Standard	Test Temperature °C			
	600	1100	1300	1500
4MPRm	95+	NSD	NSD	90-
6MPRm	NSD	NSD	95+	95-
6MFeRm	NSD	NSD	NSD	98-
6MSiRm	NSD	NSD	95+	NSD
6MTaRm	NSD	95+	99+	NSD

* The symbols in the table have the following significance:

NSD — No significant difference.

95± — 95 percent confidence that the high temperature value is higher (+) or lower (-) than the room temperature value.

Table 4-6

Estimate of Percentage Intergranular Fracture
Based on SEM Observations

Composition		Test Temperature				
%MgO	1% Additive	20°C	600°C	1100°C	1300°C	1500°C
40	None	20	10	70	50	100
60	None	10	40	90	70	100
80	None	--	--	90	80	100
60	SiO_2	10	10	30	50	50
40	TiO_2	0	--	(75)	100	--
60	TiO_2	0	--	100	100	--
80	TiO_2	--	--	--	100	--
40	Ta_2O_5	--	--	--	50	--
60	Ta_2O_5	20	20	50	100	100
80	Ta_2O_5	--	--	--	100	--
40	Fe_2O_3	0	--	--	100	--
60	Fe_2O_3	0	0	50	100	100
80	GeO_2	40	--	--	100	--
60	V_2O_5	10	--	--	100	--

Table 4-7

Students t test results of comparisons between doped magdols and equivalent undoped results.

Standard Results	Dopants			
	SiO_2	Fe_2O_3	TiO_2	Ta_2O_5
4MP11	--	--	NSD	--
4MP13	95+	NSD	99.9+	99+
6MPRm	NSD	NSD	--	NSD
6	NSD	NSD	--	NSD
11	99+	NSD	99+	99+
13	99-	99.9-	NSD	NSD
15	99+	NSD	NSD	99.9+
8MP13	--	--	95-	90-

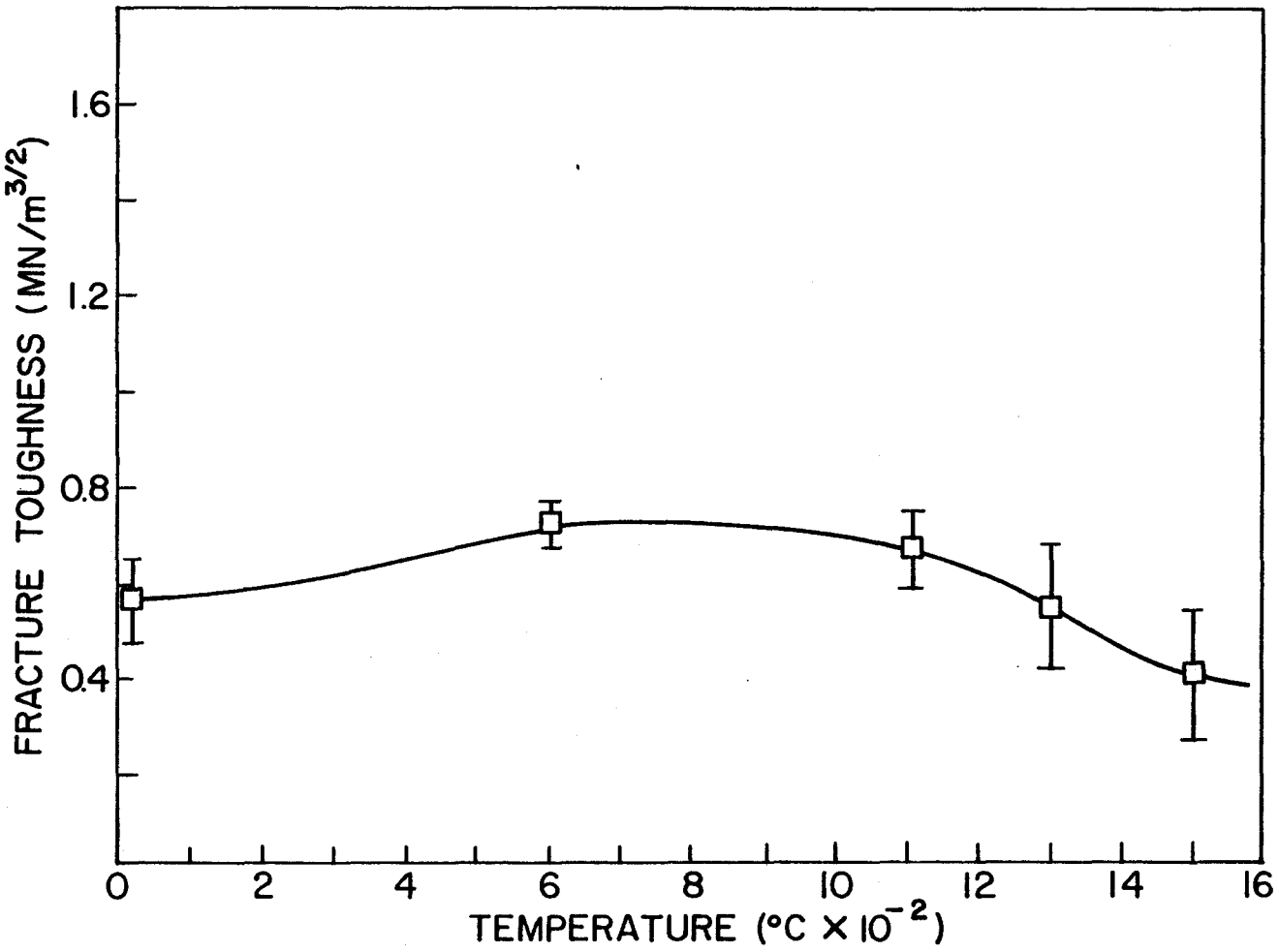

Figure 4-34 Temperature dependence of K_{1C} for 40% MgO without dopants (4MP)

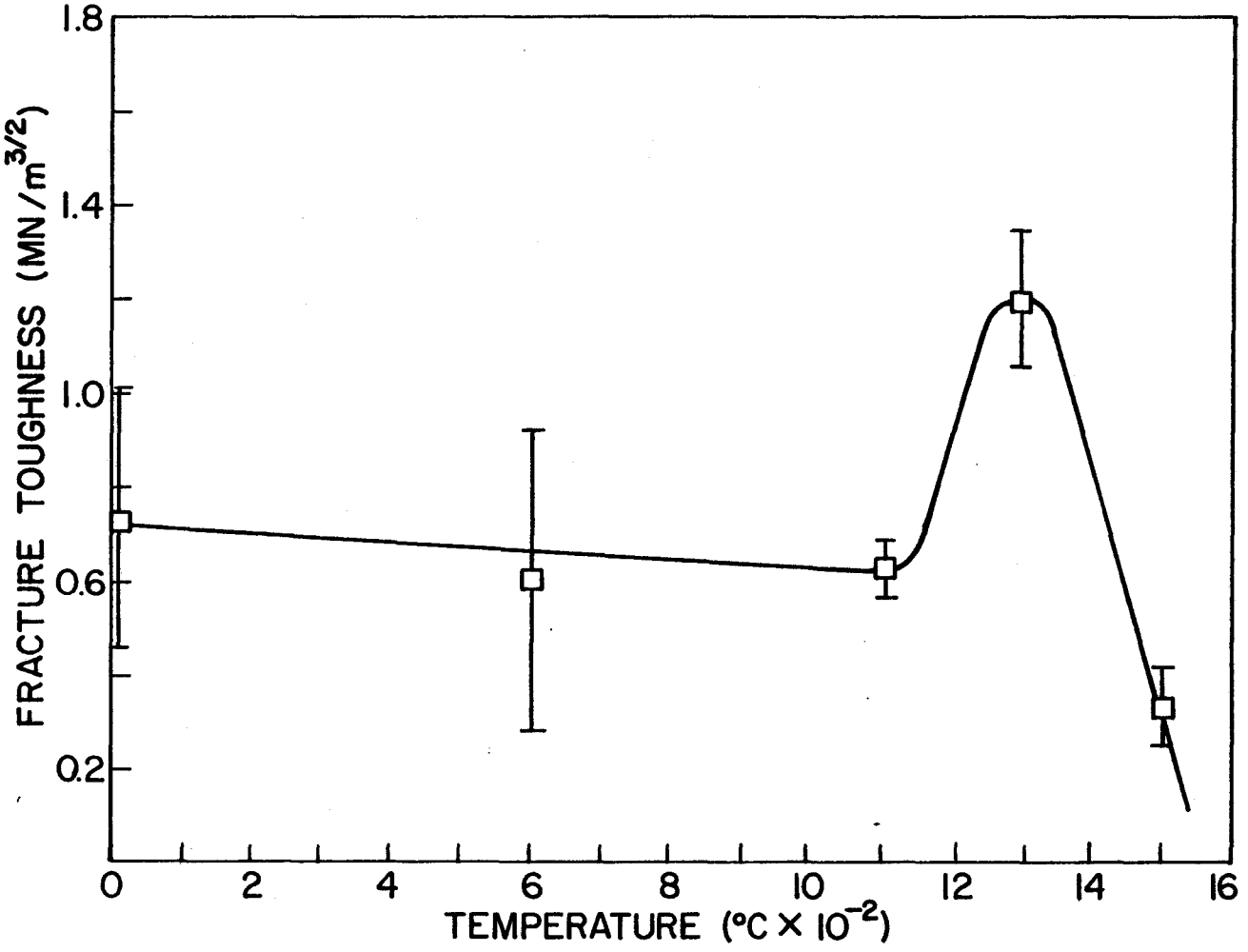

Figure 4-35 Temperature dependence of K_{1C} for 60% MgO without dopants (6MP)

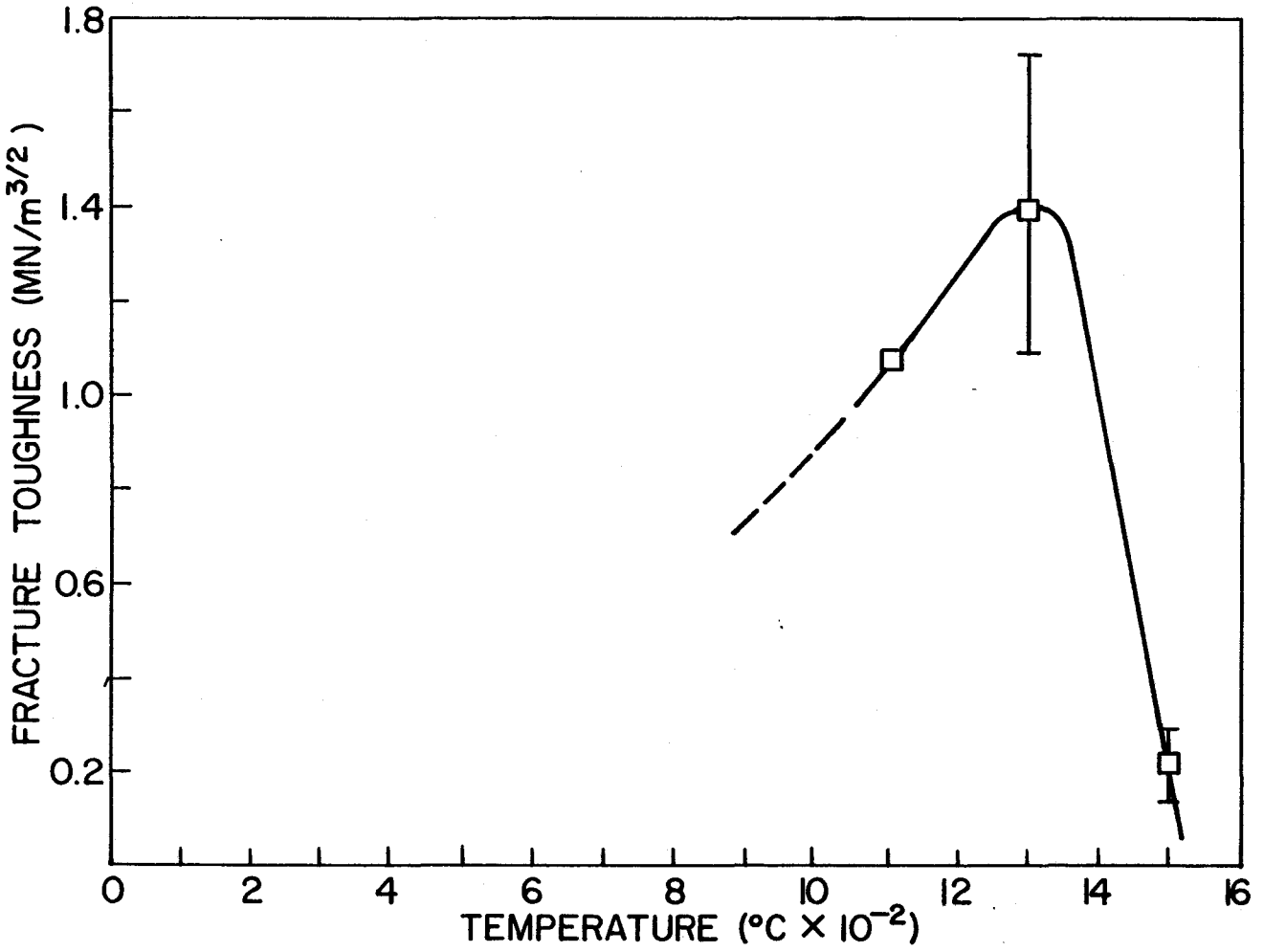

Figure 4-36 Temperature dependence of K_{1C} for 80% MgO undoped (8MP)

In contrast, the 6MP and 8MP materials show a significant K_{1C} peak at approximately 1300°C followed by a rapid fall to 1500°C.

The difference in behavior between the 4MP and 6MP compositions must be related to the microstructures of these materials. The most important microstructural characteristic is the presence of a continuous MgO phase in the 6MP and 8MP while the 4MP shows a nearly continuous CaO phase. Thus the pronounced K_{1C} peak in the former compositions most likely reflects the difference in the behavior of the CaO and MgO. As discussed in Section 2.7.6., both are semi-brittle solids which show a ductile-brittle transition at an elevated temperature.

Single crystals of MgO exhibit plasticity at 1300°C and poly-crystaline MgO shows grain boundary sliding in creep studies at 1300°C. However as previously noted, no transition from brittle to ductile behavior occurs until 1700°C for MgO tensile tests. The lack of plasticity in CaO below 1400°C reported by Rice (50) makes plastic deformation of pure materials unlikely as plasticity in the MgO could not be accomodated by the CaO.

The transducer output showed the deflection of the loading column to be a linear function of time (with constant loading rate) at temperatures up to 1300°C. Thus little inelastic deformation occurs during loading. However a single test done on the 60% MgO composition with a constant 1.5 Kg load inidcated considerable yielding on slow heating to 1300°C. Plastic deformation was initiated at about 1250°C and increased rapidly

with increased temperature.

The fracture surfaces of the undoped magdols (Figures 4-37 to 4-48) show a number of interesting features. In each case there is a transition from transgranular fracture at low temperature (Figure 4-37) to intergranular fracture at 1500°C (Figure 4-40). Estimates of the fraction intergranular fracture are presented in Table 4-6.

It can be seen that at 600°C, 1100°C and 1300°C the fraction of intergranular fracture increases with the MgO content. For all three compositions the degree of intergranular fracture is greater at 1100°C than at 1300°C (see Figures 4-38, 4-39, 4-42, 4-43, 4-45 and 4-46).

This behavior may be a result of slightly non-elastic behavior of the MgO phase. It is well known that the grain boundary strength of most ceramic materials decreases more rapidly than the bulk strength of the crystal with an increase in temperature. Thus the increase in intergranular fracture from 20°C to .1100°C can be attributed to this alone However by 1300°C the MgO phase deforms slightly and the larger grains (possible only CaO) fracture transgranularly. Unfortunately the chemical nature of the transgranularly fractured grains could not be verified using the x-ray dispersive analyser on the SEM due to the excessive roughness of the fracture face. Finally by 1500°C the bond strength of the MgO phase in the 60% and 80% MgO magdol has been radically reduced and virtually no toughness remains.

As can be seen in Figures 4-40, 4-44 and 4-47, the grains exposed

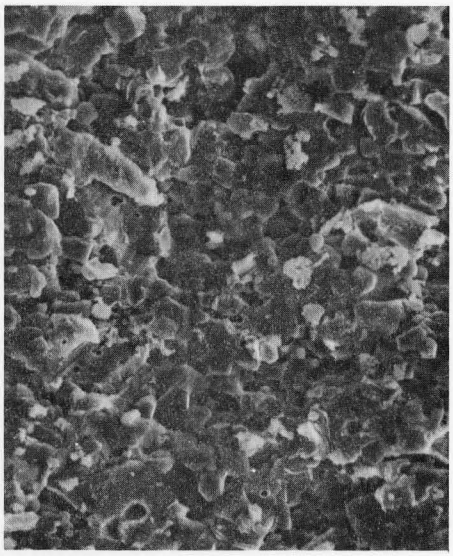

Figure 4-37

4 MP6 fracture surface.
(Tested at 600°C)
(580x)
Transgranular fracture common.

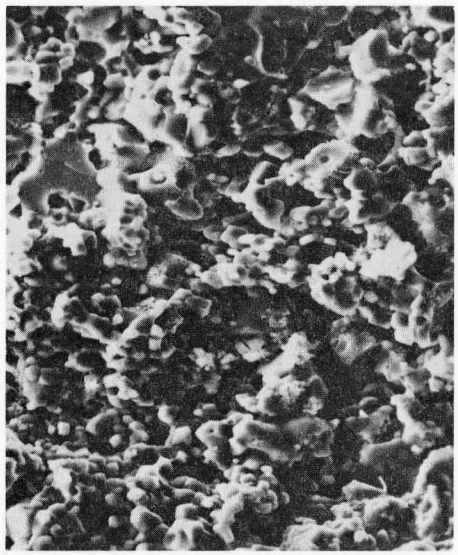

Figure 4-38

4 MP11 fracture surface.
(540x)
Increased intergranular fracture.

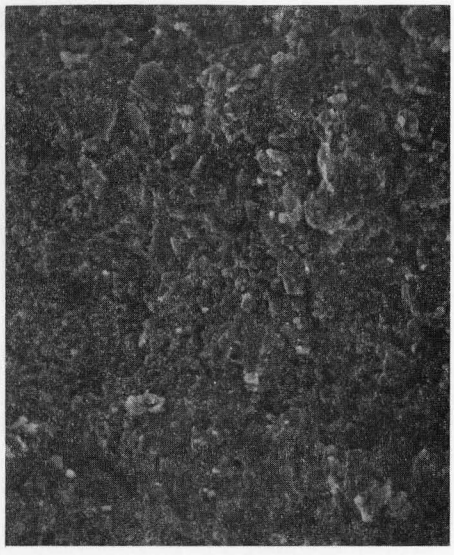

Figure 4-39

4 MP13 fracture surface.
(530x)
Increased transgranular fracture.

Figure 4-40

4 MP15 fracture surface.
(560x)
Note rounding of grains and cracking of hydrated CaO phase.

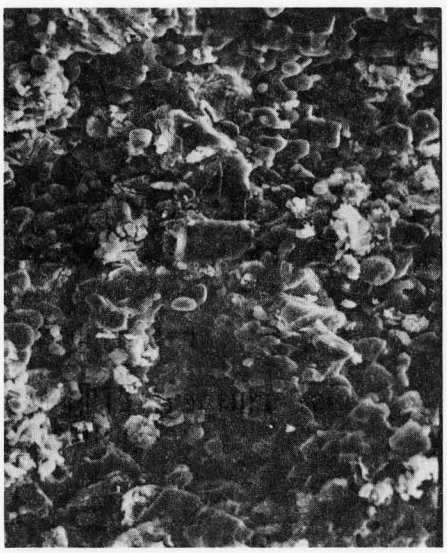

Figure 4-41

6 MP6 fracture surface.
(560x)

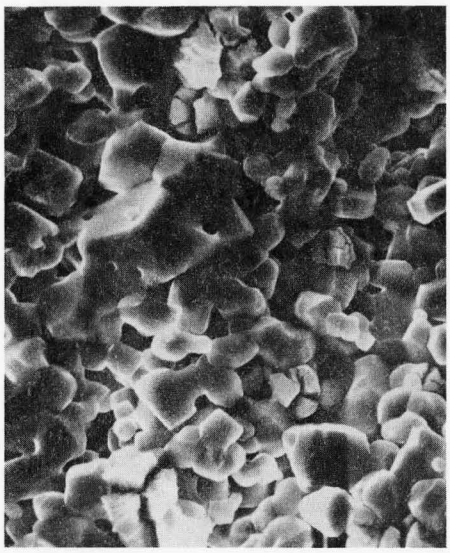

Figure 4-42

6 MP11 fracture surface.
(1120x)

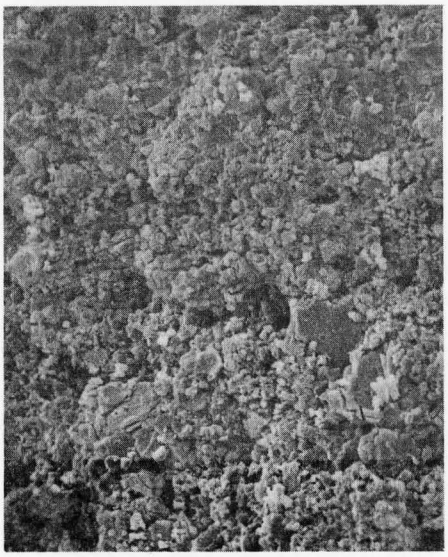

Figure 4-43

6 MP13 fracture face
(550x)

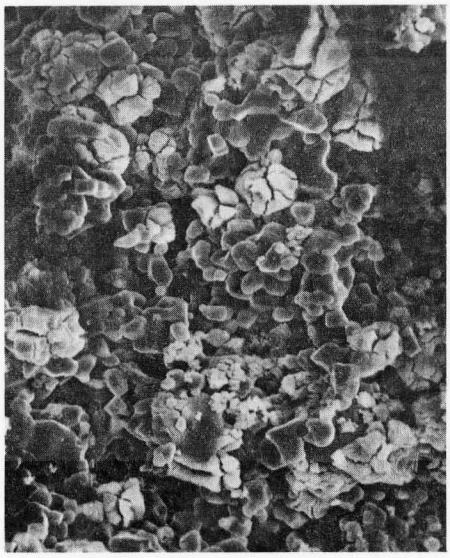

Figure 4-44

6 MP15 fracture surface.
(580x)
Note rounded grains.

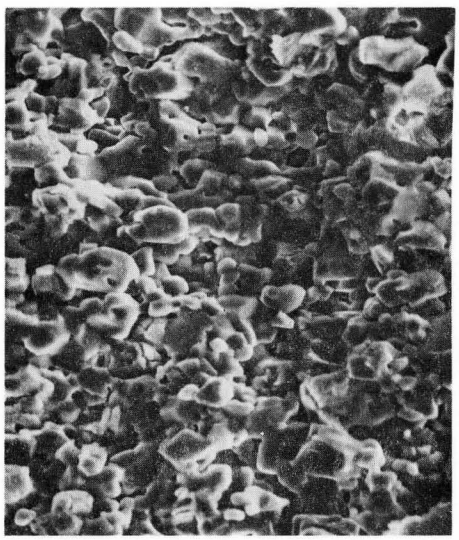

Figure 4-45

8MP11
(560x)

Figure 4-46

8MP13
(1100x)

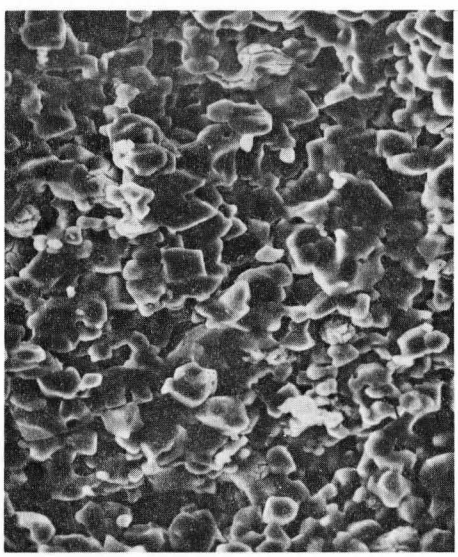

Figure 4-47

8MP15
(570x)

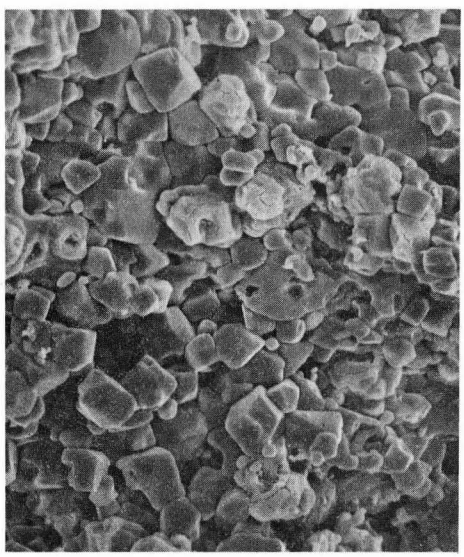

Figure 4-48

6MV13 fracture surface. (560x) Liquid is known to exist in this system at 1300°C. Note rounding of grains and compare with Figure 4-47.

on the fracture surfaces at 1500°C are very rounded. A feature which would be expected in the presence of a film of liquid at the grain boundaries.

Comparison of the fracture topographies obtained at 1500°C with those of 6MV13 (Figure 4-48) show considerable similarities. This latter specimen exhibited very low strength at 1300°C, almost certainly due to the presence of a liquid phase. The crevices between the grains in Figure 4-48 indicate a tearing action may have occured during failure. These features are not so clearly visible in the undoped material.

One possibilty that cannot be ruled out, however, is that the rounding of the grains is due to thermal etching during the short period of time the specimens spent in the furnace following fracture. Although hydration of the CaO phase tends to obscure details, there appears to be no substantial difference in the behavior of the two phases in the vanadium oxide doped material.

The impurity responsible for the formation of any grain boundary liquid is almost certainly the Na_2O native to the MgO. A simple calculation based on cubic grains 20 μm diameter indicates that the grain boundary surface area per cubic centimeter is $1500cm^2$. Since chemical analysis indicates that there will be .0003 gm Na_2O or 3×10^{18} molecules per cc MgO, a monolayer of Na_2O could form. This is important since Na_2O is known to be a powerful fluxing agent as evidenced by its use in glass and for fluxing high titania blast furnace slags (163).

A K_{1C}-temperature dependence similar to those obtained for the 6MP and 8MP material has previously been observed for silicon nitride (142) and impure alumina (139) (see Section 2.7.5.). These results were interpreted as indication of a viscous liquid at the grain boundaries coupled with grain pullout due to the weak grain boundaries.

The possibility that a second phase is present in the magdol structure is supported by the work of Liepold (12,13) who showed that very low levels of Ca and Si segregate at the grain boundaries of MgO without forming a second phase discernable by conventional ceramographic techniques (see Section 2.2.1.).

4.3.3. Effect of SiO_2 on the Fracture Results

The effect of temperature on the K_{1C} values of the 6MSi magdol is presented in Figure 4-49. The silica doped material showed exceptional toughness at 1500°C. The statistical analysis of the data (Table 4-5) shows that the K_{1C} value at 1300°C is significantly higher than the room temperature value (at the 95% confidence level) while the value at 1500°C is not significantly different from that at room temperature. The value 6MSi15 is however significantly higher than the value for 6MP15 (99% confidence).

Examination of the fractographs in Figures 4-50 to 4-52 (summarized in Table 4-6) indicate that a high degree of transgranular fracture occurs at 1100°C, 1300°C and 1500°C as compared with the undoped material. The presence of many fine cracks in the specimen (Figure 4-27) did not result

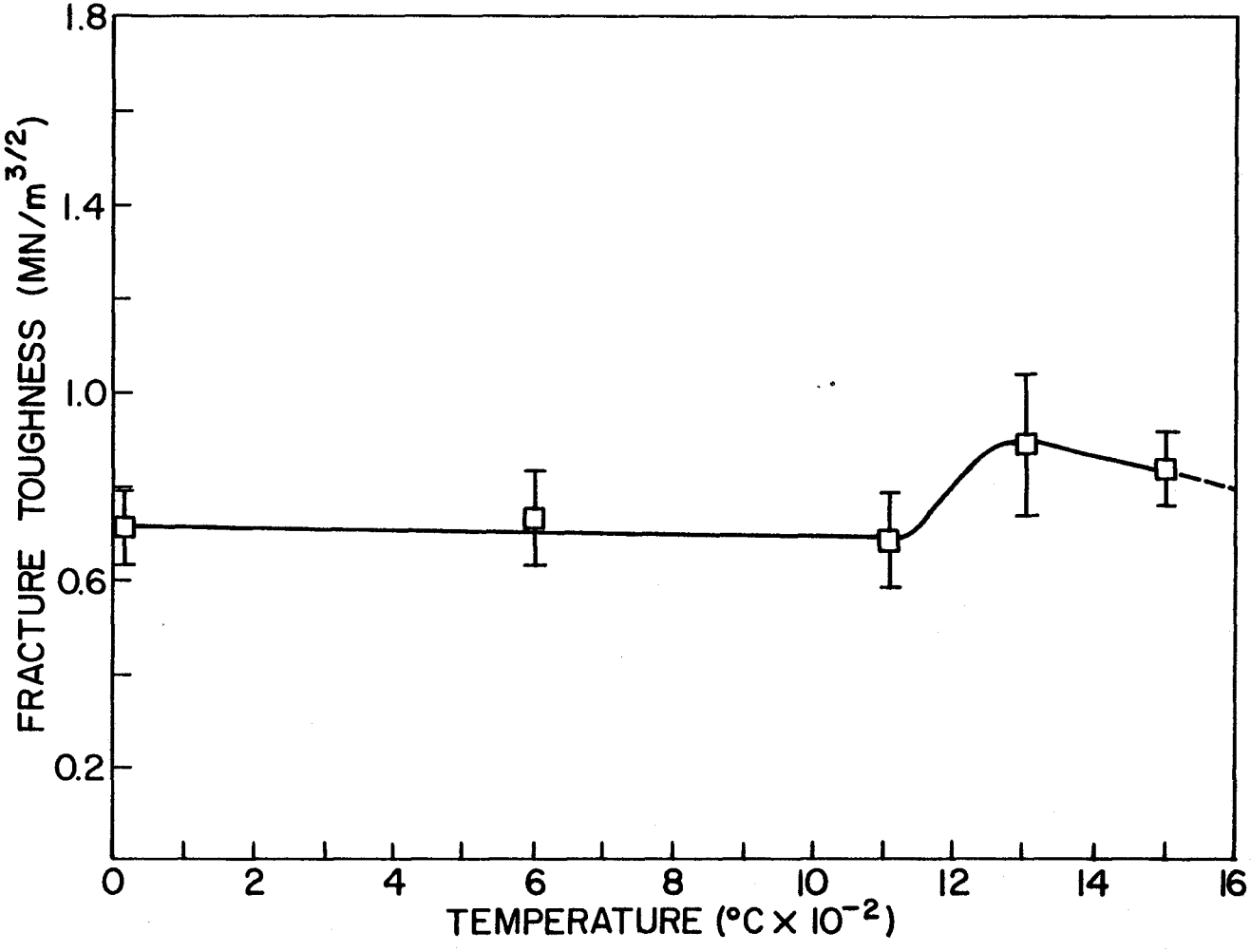

Figure 4-49 Temperature dependence of K_{1C} for 60% MgO doped with 1% SiO_2 (6MSi)

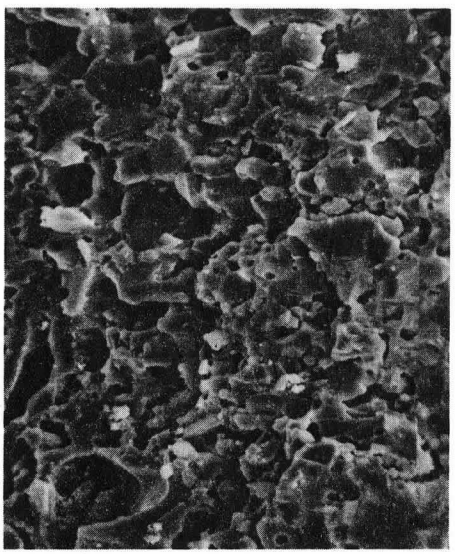

Figure 4-50

6MSi6 fracture surface.
(570x)

Figure 4-51

6MSi13 fracture surface.
(590x)

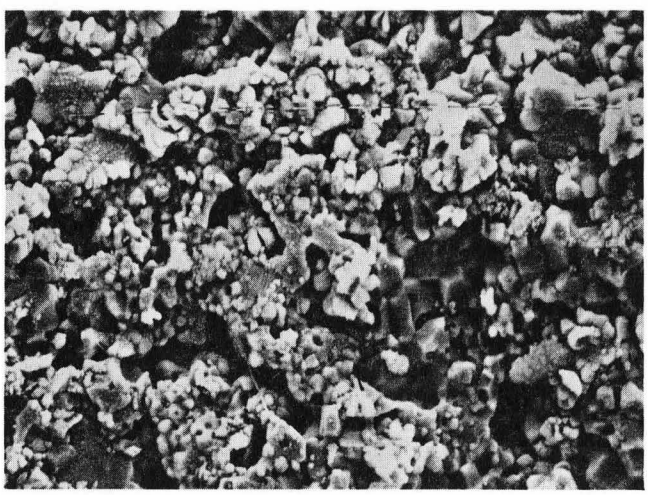

Figure 4-52

6MSi15 fracture surface.
(560x). Note that there is little
evident rounding of grains at 1500°C.

in any detectable reduction in the toughness of this material. It is likely that these microcracks are the result of the decomposition of $3CaO \cdot SiO_2$ to CaO and $2CaO \cdot SiO_2$ at 1250°C. This effect is well known (164) and results in the "dusting" of silica-rich refractories containing CaO.

The fact that the 1300°C K_{1C} value also showed a significant increase over the 1100°C value (at the 99% confidence level) may indicate that the $3CaO \cdot SiO_2$ has reformed thus relieving stresses caused by the original decomposition.

As discussed in Section 2.7.4. the presence of a large number of microcracks at the crack tip may lead to a greater toughness either by deflecting the crack or allowing a limited amount of stress relaxation at the crack by means of a pseudoplastic zone as discussed by Green (158). The fact that the 40% MgO doped with silica also showed a significant increase in toughness over the undoped material indicates that the silica doped magdols are not as sensitive to MgO content as the undoped materials.

An alternative possibility for the increased toughness of the silica doped materials is the formation of refractory silicate precipitates preventing fracture of the grain boundaries (which are weak in undoped materials). They may do this by acting as a getter for the Na_2O and other contaminants which may be concentrated at the boundaries. Alternatively the physical presence of the precipitates (which were shown to form in the single phase materials) may prevent shearing of the grain boundaries, resulting in transgranular fracture.

4.3.4. Effect of Ta_2O_5 on the Fracture Results

The temperature dependence of K_{1C} for Ta_2O_5 doped magdols shown in Figure 4-53 is similar to that of 6MSi as there is a significant increase in the toughness of the 6MTa11 over 6MTaRm result (95% confidence) and 6MP11 material (99% confidence), (Tables 4-5 and 4-7). Like the 6MSi material the values of K_{1C} for 6MTa15 are not significantly different from those of 6MTaRm and at the 99.9% confidence level they are higher than those of 6MP15.

The values of K_{1C} obtained for the 6MTa material are higher than those obtained in the silica system at 1100°C and 1300°C (99% confidence) and statistically the same at 1500°C. If the formation of refractory tantalate compounds accounts for the increased K_{1C} then the decomposition of $5CaO{\cdot}Ta_2O_5$ to $4CaO{\cdot}Ta_2O_5$ and CaO at 1460°C may play a role, although no microcracks such as observed in the 6MSi materials were detected, possibly accounting for the increased toughness of 6MTa materials over 6MSi at 1100°C and 1300°C. The fact that the decomposition reaction to form $5CaO{\cdot}Ta_2O_5$ occurs at 1460°C may explain the drop in toughness at 1500°C.

From the fractographs presented in Figures 4-54 to 4-56 and summarized in Table 4-6 it is evident that fracture is extensively transgranular at 1100°C although the effect is not so pronounced as in 6MSi. At higher temperatures in the 6MTa magdol fracture becomes extensively intergranular. The rounded appearance of the 6MTa13 (Figure 4-55) strongly

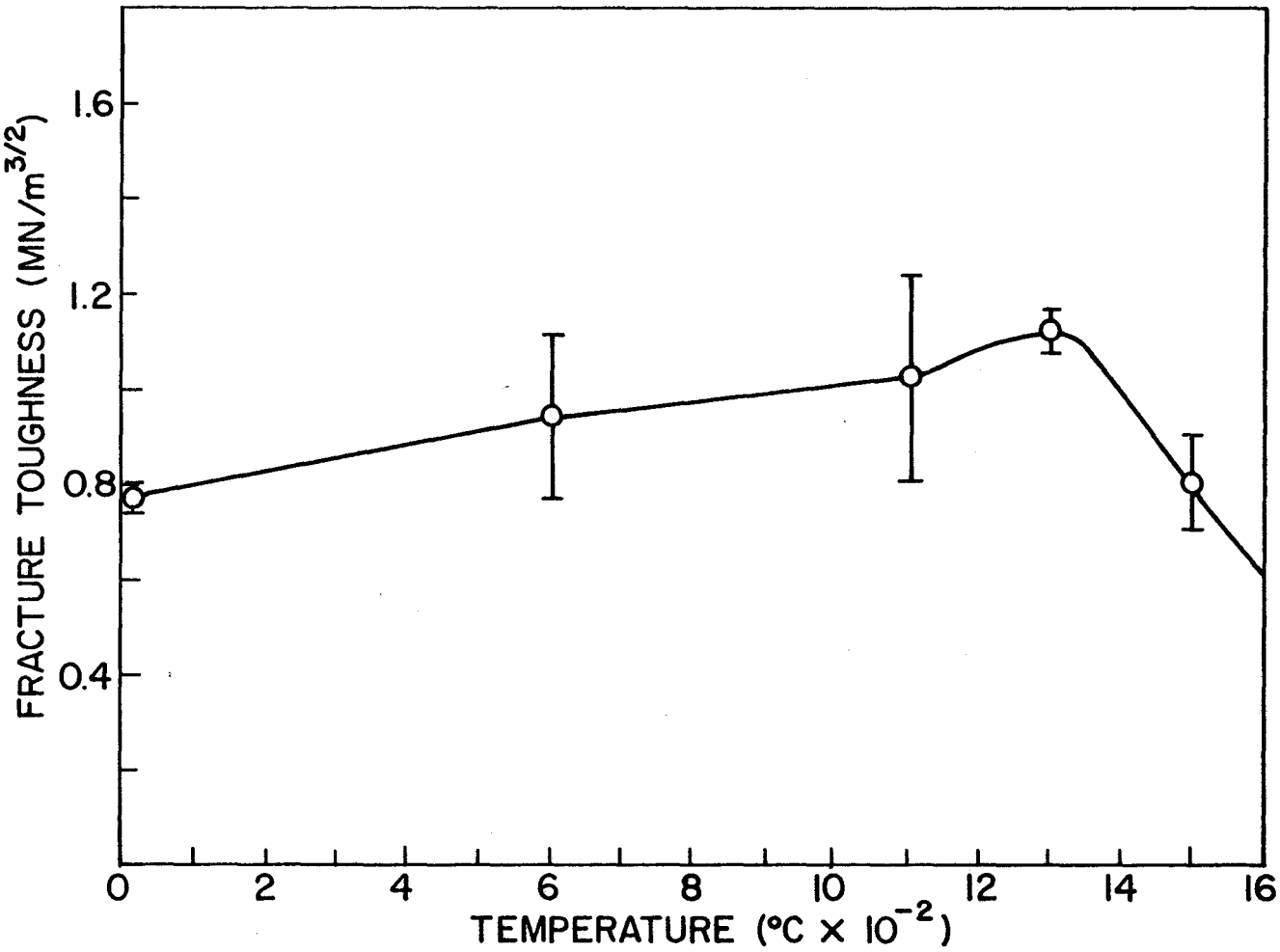

Figure 4-53 Tempeaature dependence of K_{1C} for 60% mg0 doped with 1% $Ta_2 0_5$ (6MTa)

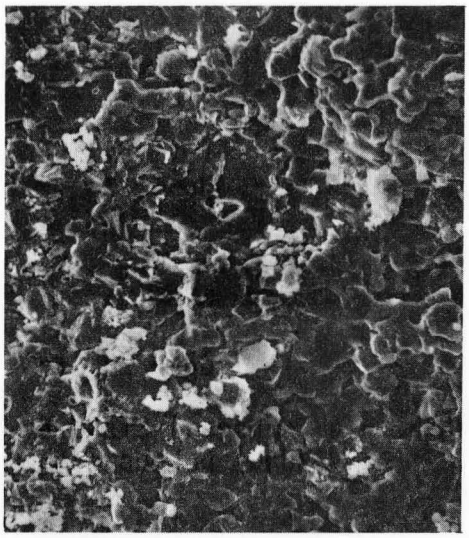

Figure 4-54

6 MTa 6 fracture face shows transgranular fracture (550x).

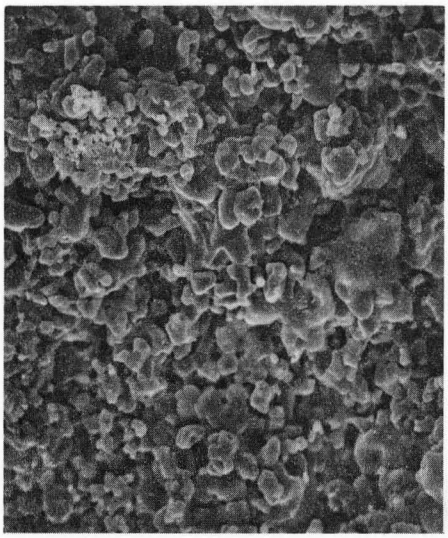

Figure 4-55

6 MTal3 fracture face in intergranular and rounded (550x).

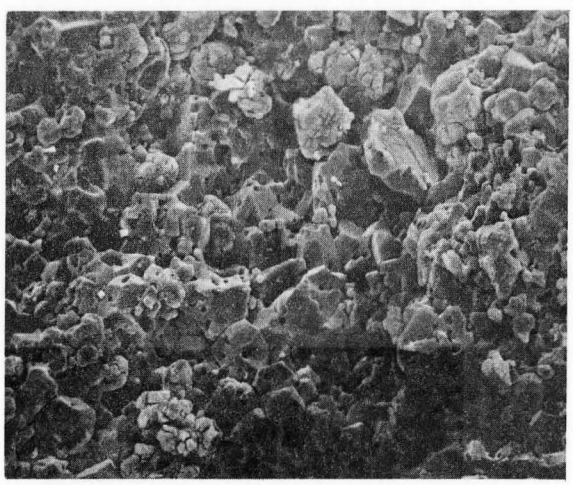

Figure 4-56

8 MTal3 fracture face is intergranular, not rounded (560x).

indicates a liquid phase yet in contrast the 8Mtal3 (Figure 4-56) specimen shows no rounding. This difference can be attributed to a longer residence in the hot furnace for the former samples resulting in thermal rounding. It can be concluded that liquid is not in fact extensive in the 6MTa specimens.

In view of the above results a reasonable explanation of the toughness temperature relation is the formation of a refractory tantalate which, possibly combined with a getting action for Na_2O results in stronger grain boundaries and increased toughness at high temperatures.

4.3.5. Effect of Fe_2O_3 on Fracture Toughness

The effect of temperature on the K_{1C} values of the 60% MgO compositions doped with 1% Fe_2O_3 is plotted in Figure 4-58. This system is interesting since it shows no sign of toughening due to liquid phase despite microstructural evidence of its presence (Figures 4-61 to 4-62).

Liquid would not be expected from the equibrium data as the iron oxide would form a solid solution with the MgO phase. However magnesio-ferrite precipitates are expected during cooling and, in the CaO-Fe_2O_3 system, a limited amount of non equibrium liquid may form as the eutectic temperature in the Fe_2O_3-CaO system is 1205°C and less than 1200°C for the FeO-CaO system. Thus it is possible that the large statistically significant (98% confidence) fall in toughness above 1300°C is due to the formation of a liquid at the surface of the CaO grains, completely destroying the strength of a large fraction of the grain boundaries.

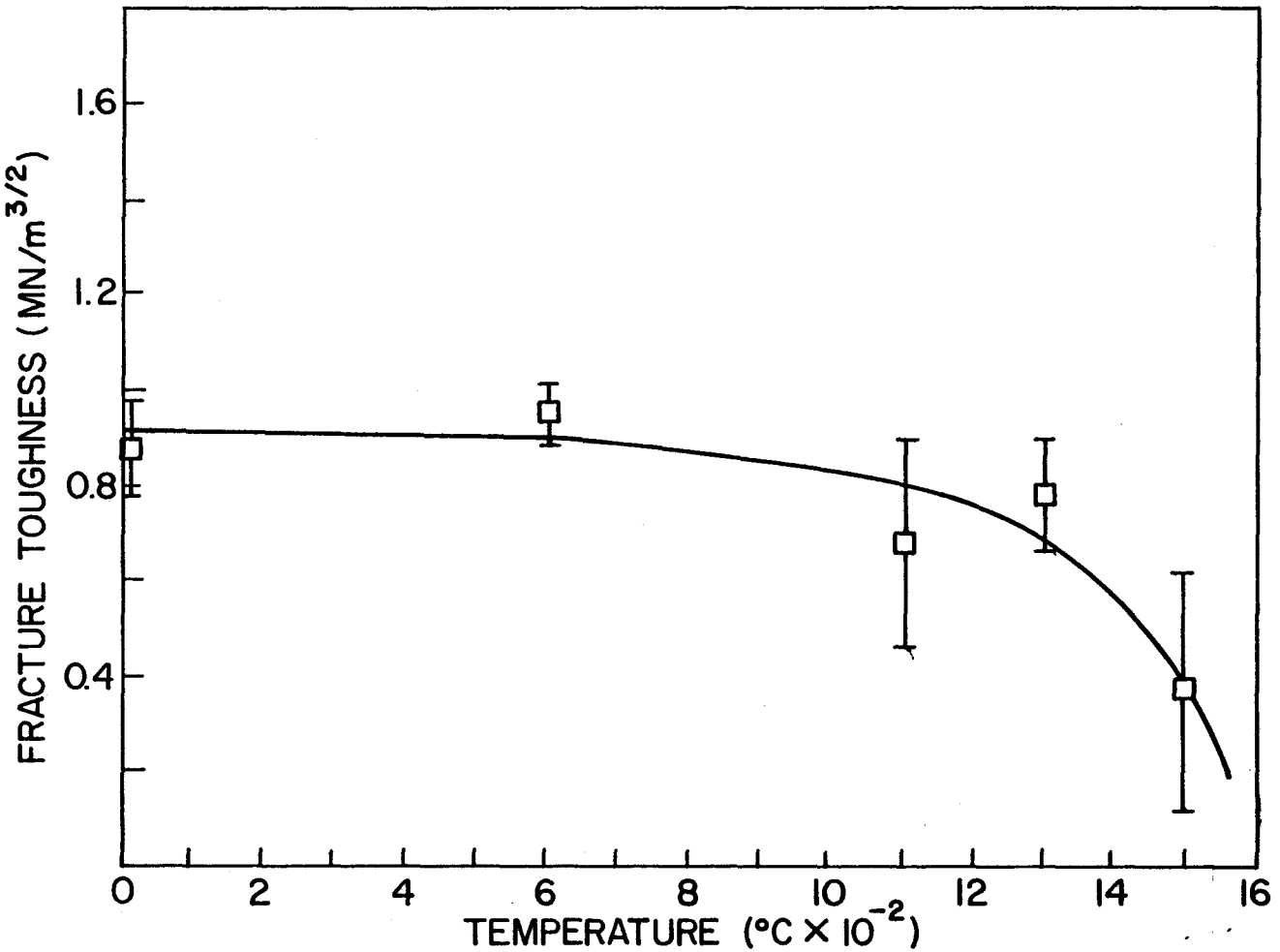

Figure 4-57 Temperature dependence of K_{1C} for 60% MgO doped with 1% Fe_2O_3 (6Mfe)

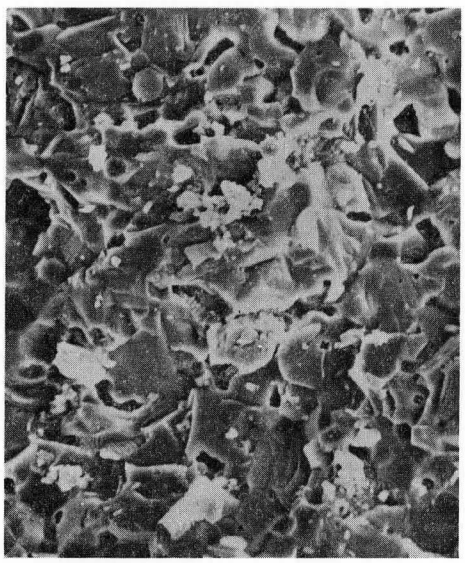

Figure 4-58

6MFe6 fracture face shows transgranular fracture (580x).

Figure 4-59

6MFe11 shows some transgranular fracture (600x).

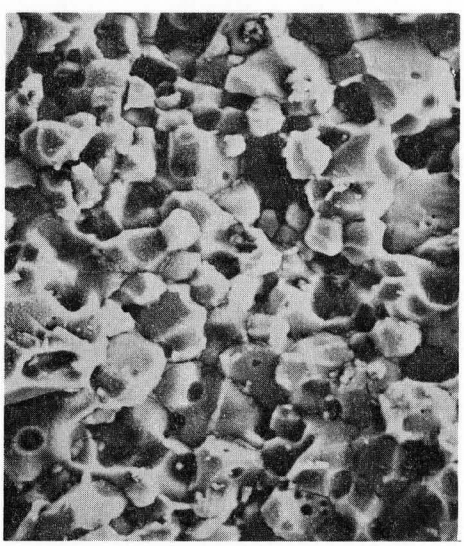

Figure 4-60

6MFe13 shows intergranular fracture. Evidence of grain boundary phase can be seen (580x).

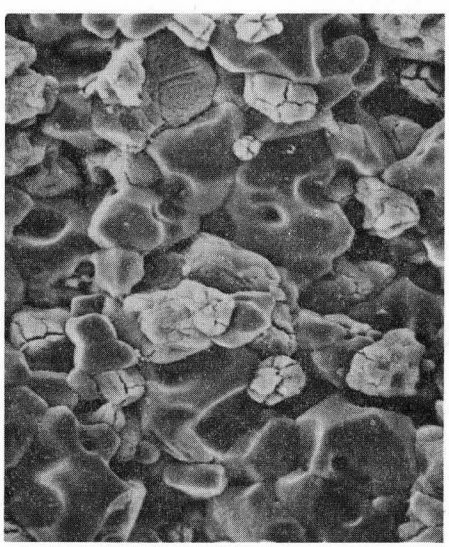

Figure 4-61

6MFe15 shows intergranular fracture with rounded grains CaO has hydrated (580x).

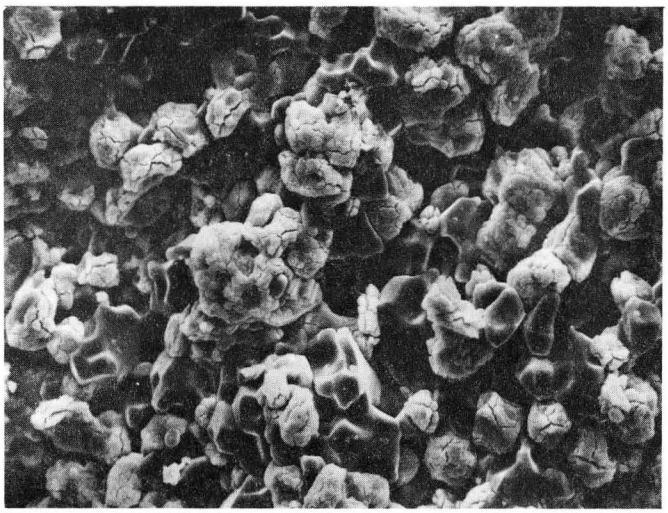

Figure 4-62 4MFe13 shows intergranular fracture with rounded grains. Compare with Figures 4-60 and 4-61 (550x).

The fracture surfaces support the interpretation (Figures 4-58 to 4-64). Both the 4MFe13 and 6MFe13 show completely intergranular fracture and very rounded grains similar to those observed in the V_2O_5 doped material (Figure 4-48).

That this can be attributed to iron oxide fluxing of the CaO grains is supported further by the greater extent of rounding evident in the 4MF13 (Figure 4-62) as compared with 6MF13 (Figure 4-60) since there is a greater CaO content in the former.

The absence of a toughness-temperature peak in these results such as found in silicon nitride and alumina, may indicate that the liquid formed in this case is very fluid. This possibility is discussed further in Section 4.4. Alternatively this result could indicate that the temperature related peak in toughness is very narrow for this composition and has therefore escaped detection. The effects of shifts in the K_{1C} peak temperature are also discussed in Section 4.4.

4.3.6. The Effect of TiO_2 on Fracture Results

Unfortunately only three points were determined for the TiO_2 doped magdol. These results are plotted in Figure 4-63. Enough information is available however to note significant features of the fracture behavior.

The titania addition was found to significantly increase the toughness of 6MTi11 over 6MP11 (99% confidence) but demonstrated no effect on the toughness of the 4Mti material. The behavior of the 6MTi13 was not

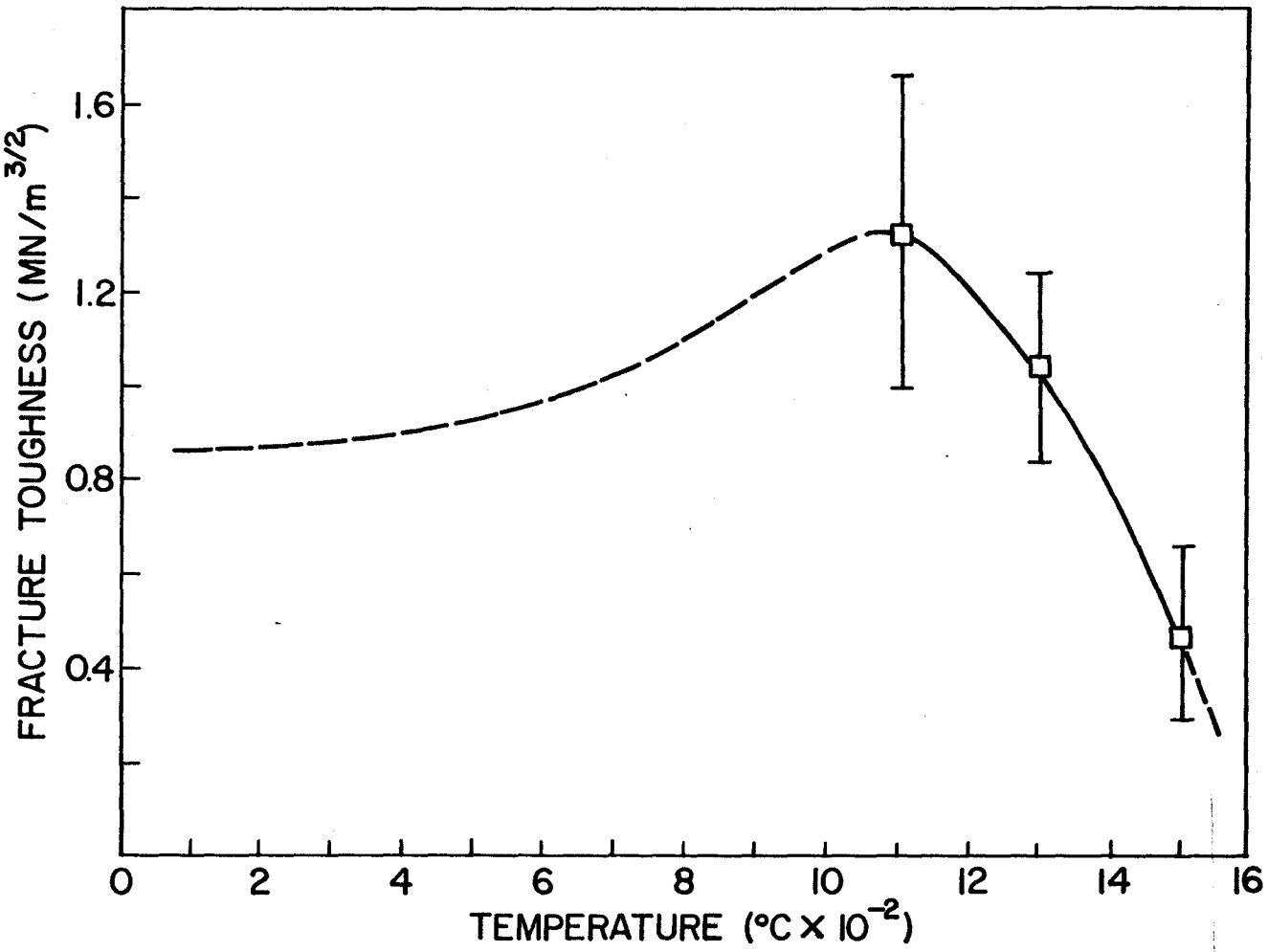

Figure 4-63 Temperature dependence of K_{1C} for 60% MgO doped with 1% TiO_2

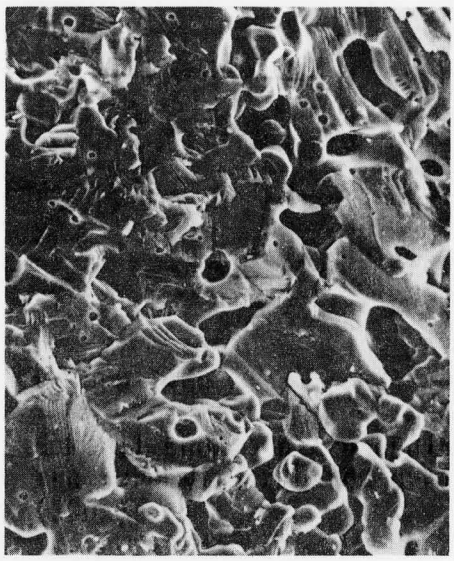

Figure 4-64

4 MTi room temperature fracture surface shows transgranular fracture (590x)

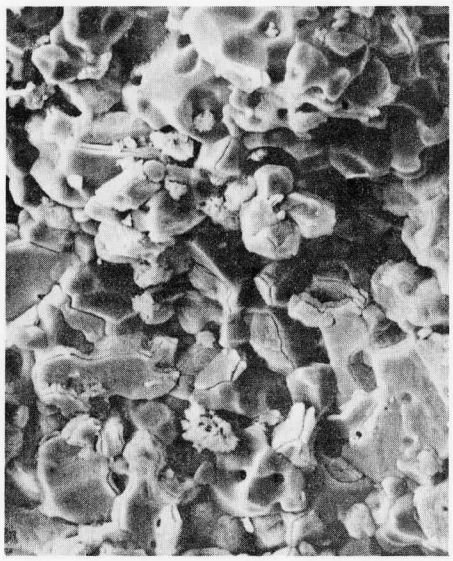

Figure 4-65

4 MTil3 shows intergranular failure with rounded grains (610x)

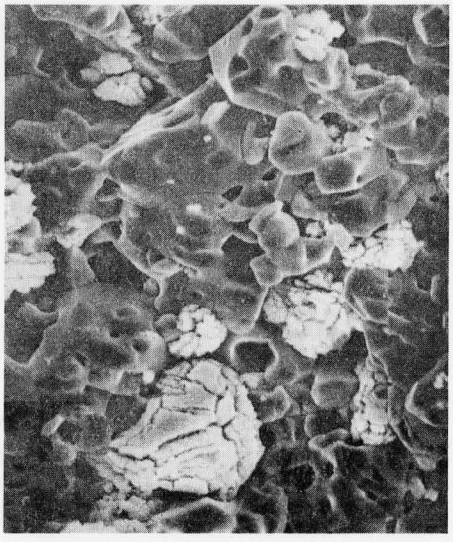

Figure 4-66

6 MTill shows intergranular fracture with rounded grains (590x)

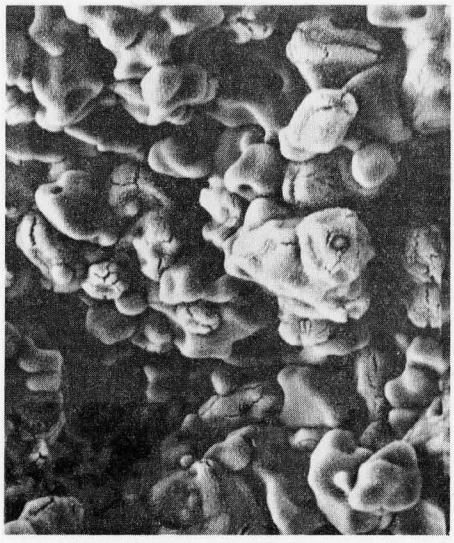

Figure 4-67

6 MTil5 shows intergranlular fracture with rounded grains (640x).

significantly different from the 6MPl3 (Table 4-7). In contrast the 4MTil3 material showed (99% confidence) a significant increase in toughness over 4MPl3. This latter result indicates that it is likely the 4MTi material exhibits a toughness-temperature peak, unlike the 4MP material. The rapid fall of the K_{1C} value above 1300°C indicates the possible influence of a grain boundary liquid phase of decreasing viscosity as also proposed for silicon nitride.

The appearence of the fracture faces (Figures 4-65 to 4-67) strongly suggests the presence of a liquid phase. The grains demonstrate pronounced rounding similar to the V_2O_5 doped material at 1300°C (Figure 4-48).

The occurence of Ti-rich precipitates in the single phase microstructures could indicate the formation of a non-equibrium titania-rich liquid although it would not be expected from phase equilibrium (Section 2.6.4.). The viscous nature of TiO_2 rich liquids has been well documented in blast furnace slags (162).

Thus the formation of a viscous grain boundary liquid is a reasonable explanation for the fracture behavior observed in these specimens.

4.3.7. Effects of GeO_2 on Fracture Results

Only two samples of 80% MgO doped with GeO_2 were tested so no firm conclusions may be drawn. The samples were tested at 1300°C and produced a K_{1C} value of 0.981 $MN/m^{3/2}$. Examination of the fracture surface (Figure 4-68) shows completely intergranular fracture with no

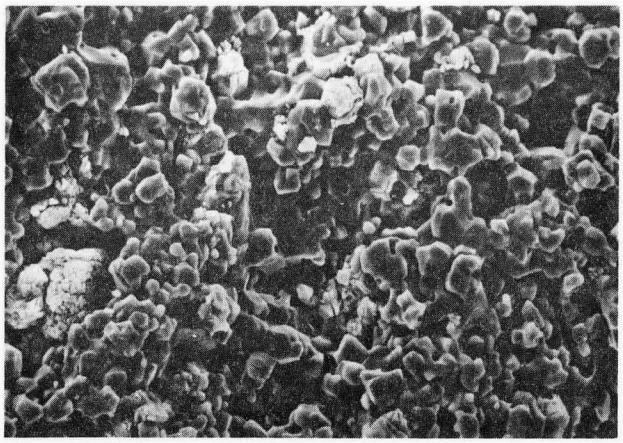

Figure 4-68 8MGel3 shows intergranular fracture and little grain edge rounding (575x).

indication of any grain rounding due to liquid formation. In view of the refractory nature of the compounds formed by MgO and CaO with GeO_2, it is reasonable that its behavior should resemble that of the silica doped material. This is particularly supported by the potential micro-cracking resulting from the decomposition of $3CaO \cdot GeO_2$ to $2CaO \cdot GeO_2$ and CaO at 1320°C.

4.4. General Discussion of Fracture Results

4.4.1. Similarities and Differences

When all of the fracture toughness results for the 60 percent magdols are considered, very strong evidence for the presence of a limited "liquid" formation at high temperatures is apparent. The most compelling evidence is the extensive rounding of the intergranular fracture observed in the TiO_2, Fe_2O_3, and undoped materials. This behavior was apparent even when the specimens were rapidly removed from the furnace following fracture.

Statistical analysis of the difference between the K_{1C} values at room temperature and other temperatures were undertaken for each additive and the results of the Student t Test are presented in Table 4-5. These results confirm the existence of three segments of the K_{1C} vs. temperature plots.

The table indicates that, with two exceptions, there are no significant differences between the room temperature K_{1C} values and those for temperatures up to 1100°C for all dopants. Similarly, additions of several dopants had no influence on the fracture toughness at 20°C and 600°C. These results in conjunction with the fractographs indicate completely brittle fracture which is independent of the dopants for temperatures between 600°C and 1100°C.

At 1100°C and 1300°C the fracture surfaces and K_{1C} results indicate the additives modify the fracture mechanism. This generally

results in increased toughness, compared with a pure system as the 4MP samples.

The third type of behavior exhibited at temperatures above 1300°C by all additives except SiO_2 and Ta_2O_5 is a sharply reduced fracture toughness. The micrographs of these fracture surfaces indicate that the grain boundaries are weak and there is considerable evidence for the existence of a grain boundary liquid phase.

For the V_2O_5 doped material, a liquid is likely near 1200°C. This is in agreement with both Brown (93) and Nicholson's (93a) work and the phase equibria data discussed previously. In this sample the grain rounding and separation shown in Figure 4-48, clearly resembles that of the 6MP15, 6MTi13, 6MFe13, and 6MF15 samples. Conversely 6MSi and 6MTa showed only minimal evidence of such behavior.

This can be directly related to the plots of fracture toughness as a function of temperature as the 4MP, 6MSi, 6MFe and possibly 6MGe failed to show pronounced peaks of toughness near 1300°C. Similar peaks in the fracture toughness temperature plots have been attributed to liquid formation in silicon nitride and alumina as previously outlined in Section 2.7.5.

The occurence of rounded grains and K_{1C} peaks in the 6MP and 8MP compositions suggests that as little as 0.01% Na_2O in the MgO is sufficient to cause serious strength and toughness reduction of magdols at elevated temperatures.

The absence of such a peak in the iron oxide doped magdol, despite

microstructural indications of liquid formation, may be due to the formation of a highly fluid liquid. This may in turn result in the appearance of a very narrow peak close to the temperature of formation of the eutectic liquid. The manner in which such a peak could be over looked is illustrated in Figure 4-69.

A similar argument could be advance for the SiO_2 doped magdol however, the distinctive appearance of rounded grains was not observed on the fracture faces rendering such a mechanism unlikely.

In the case of the 4MSi and 8MSi specimen, fracture tests were generally done only at 1300°C and similar problems of interpretation are encountered as the values at 1300°C tell almost nothing about the nature of the K_{1C} temperature dependence. Any shifting of the K_{1C} peak temperatures to higher or lower values will result in rapid changes in the value of K_{1C}. This severely reduces the significance of these values. One may speculate on these values by analogy with the results of the other doped and undoped compositions. The statistical evidence presented in Table 4-7 indicates that there is no significant difference between the room temperture fracture toughness of the doped 60% MgO materials. If this is also true for the 40% MgO material then the 4MTi11 and 4MTi13 values indicate this closely resembles the 6MTi. This result is in contrast to the well defined differences observed between 4MP an 6MP.

This result is not unreasonable since if the differences between the undoped compositions is in fact due to the slight Na_2O content then a 1% addition of another liquid forming oxide might be expected to

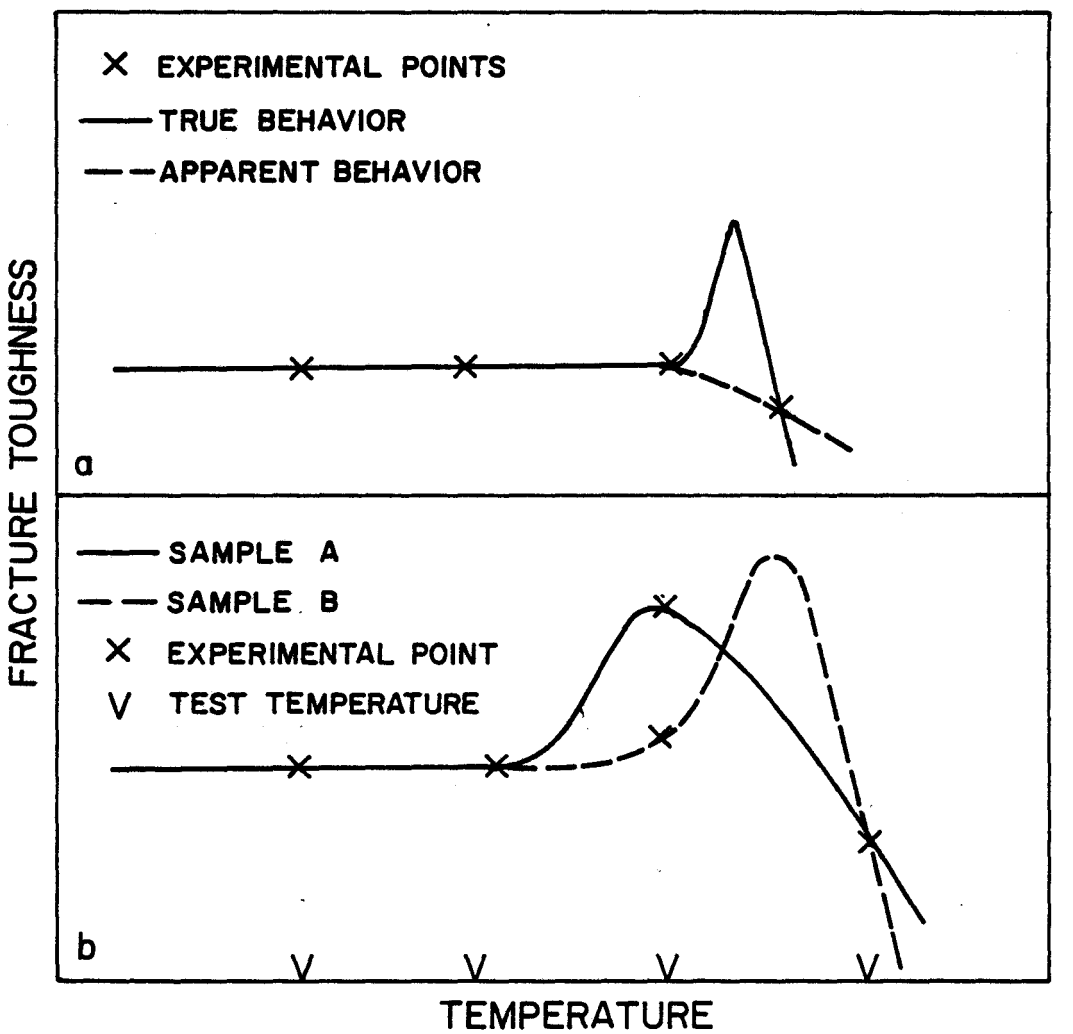

Figure 4-69 a) A few experimental points may bracket a "narrow" toughness peak.

b) Constant temperature tests may produce anomalous results if the fracture peak is displaced.

completely dominate the fracture behavior.

As the results, with the exception of SiO_2 and Ta_2O_5 doped material, strongly indicate the formation of a liquid phase at elevated temperatures, it is interesting to speculate on the effect of the viscosity of these eutectic liquids on the K_{1C} values. This could be pronounced since if failure is occuring by grain boundary sliding and tearing higher viscosities will result in greater apparent toughness.

4.4.2. Corrections for Porosity Differences

A factor which must be considered in analysis of the toughness results is the role of porosity. As noted in Section 2.7.3, Knudsen's(125) porosity correction for Youngs Modulus accounts for much of the difference in K_{1C} values for porous alumina or reported by Claussen (140).

Using the observed bulk density data for the magdol compositions and equation 2.14 estimates of the K_{1C} values for fully dense materials were made in an effort to remove any effects of porosity. Statistical significance tests were undertaken via the Student t analysis. These results, presented in Table 4-8, show that there is little difference from the non-corrected values summarized in Table 4-7.

Aside from generally slight changes in the levels of significance obtained, only two major changes occured. The first of these was in the comparison between 6MP13 and 6MTi13 where a significant difference appears (at 90% confidence level). This has little importance however in view of the temperature of the test. This may only in fact indicate a slight shift in the location of the toughness peak rather than an increase in its magnitude.

Table 4-8

Significance of the differences between doped and undoped magdols at equivalent temperatures following correction for porosity differences.

	With Dopands			
Standard	Si	Fe	Ti	Ta
4MP11	--	--	NSD	--
13	NSD	NSD	99.9+	99+
6MPRm	NSD	NSD	--	NSD
6	NSD	NSD	--	NSD
11	NSD	NSD	99+	99.9+
13	99.9-	99.9-	90+	NSD
15	99.9+	NSD	NSD	99.9+
8MP13	--	--	95-	NSD

The other change is the disappearance of the 90% confidence of a difference between 8MP13 and 8MTal3. This is interesting as different mechanisms may be operating in these two systems and quite different temperature-toughness profiles would be expected. However, due to the small number of tests done for in this range and the weakness of the confidence, no firm conclusion may be drawn.

4.4.3. Dependence of K_{IC} on Percent MgO

The 1100°C and 1300°C fracture toughness results when plotted as a function of % MgO (Figures 4-70 and 4-71) indicate, with the exception of the anomolous TiO_2 doped material tested at 1300°C, a general trend toward increased toughness with increased MgO. Examination of values at other temperatures reveals no such trend. Despite this apparent increase in toughness, analysis of the experimental data by means of the Student t test (Table 4-9) indicates that the only significant differences are those between 4MP11 and 8MP11 and 4MP13 and 6MP13. The application of the possible porosity correction to the results actually reduces the difference between the 6MP and 8MP whilst having no effect on the statistical significance.

Several possible explanations suggest themselves for this behavior. The most direct is that the toughness of the material increases with the increase in MgO content. The two phase material then shows direct relations between the volume fraction of each phase and its fracture toughness. However, the fact that the 60% and 80% MgO toughness values are so similar when corrected may indicate that this is not correct. A

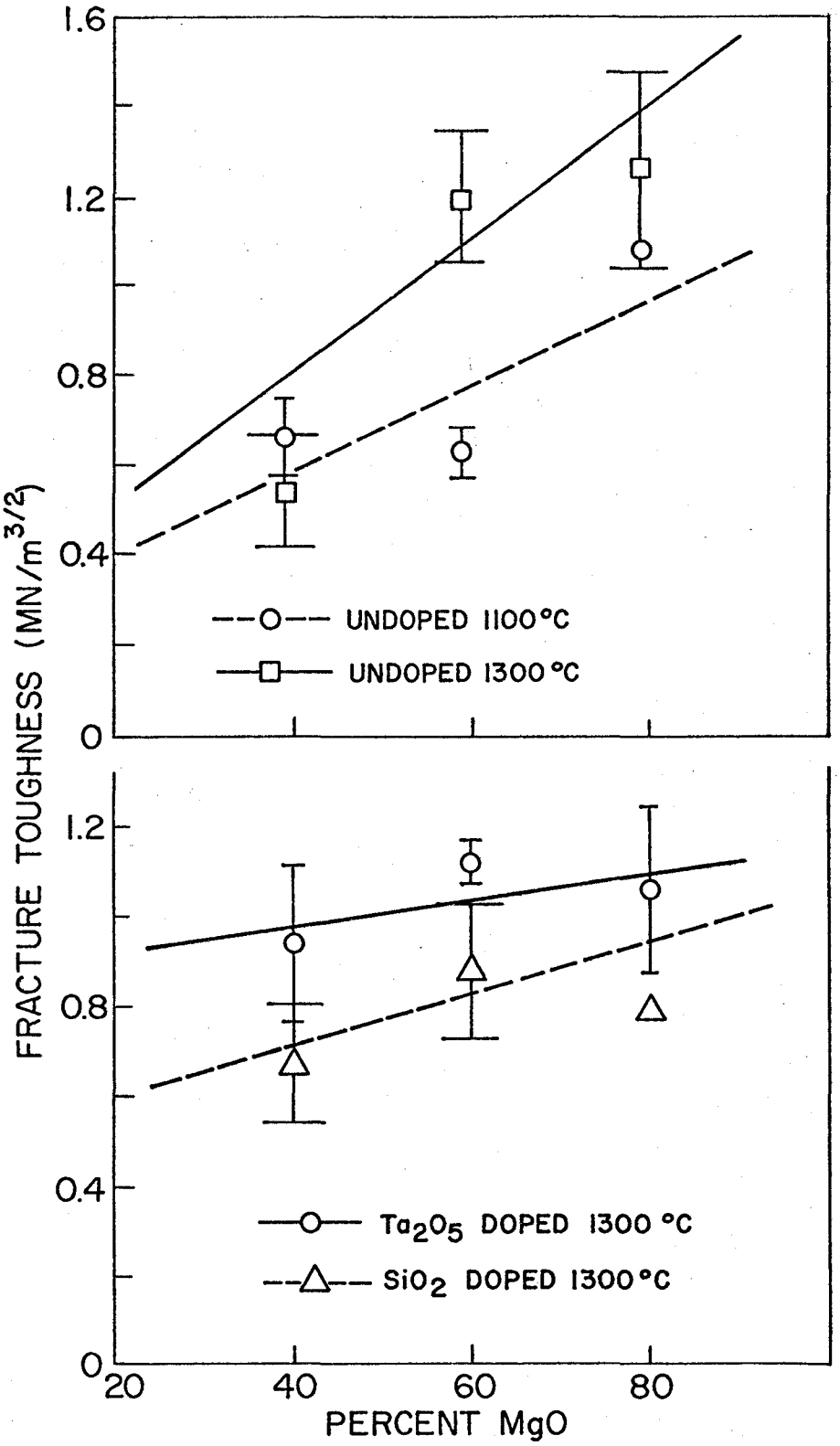

Figure 4-70 Effect of MgO content upon fracture toughness of magdols at 1300°C and 1100°C.

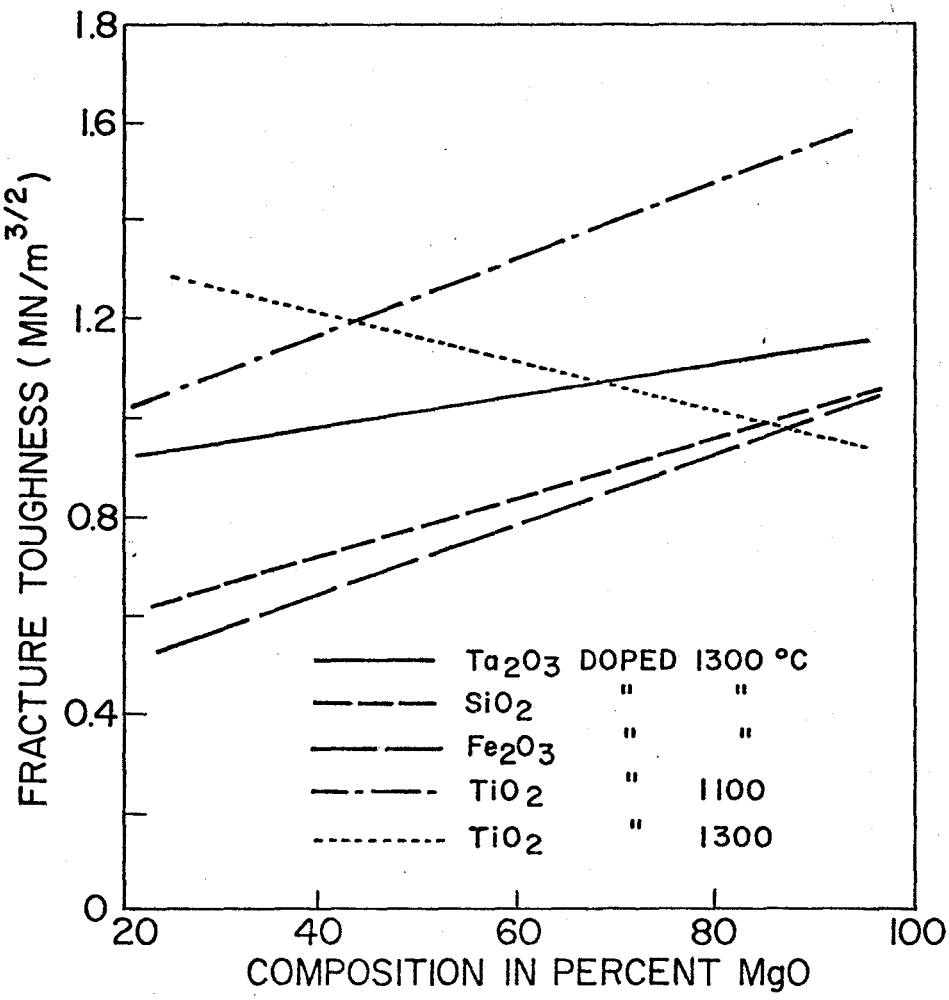

Figure 4-71 Comparison on the dependence of K_{1C} on MgO content between dopants.

Table 4-9

Statistical Significance of MgO Content

Standard	Compared with Higher MgO Contents			
	60 MgO	60 MgO (Corrected)	80 MgO	80 MgO (Corrected)
4MPRm	NSD	NSD	--	--
4MP6	NSD	NSD	--	--
4MP11	NSD	NSD	99.9+	99.9+
4MP13	99.9+	99.9+	99.99+	99.99+
4MP15	NSD	NSD	90-	95-
6MP11	--	--	NSD	NSD
6MP13	--	--	NSD	NSD
6MP15	--	--	NSD	NSD
4MFe13	90+	90+	--	--
4MTi11	NSD	NSD	--	--
4Mti13	NSD	NSD	NSD	NSD
6MTi13	--	--	NSD	NSD
4MSi13	95+	90+	--	--
4MTa13	NSD	NSD	NSD	NSD

further consideration is that results of lower temperature tests do not show this relation when the possibility of plastic contributions to γ_I are minimized. The possibility exists that the transformation in K_{1C} values between 40% and 60% MgO at 1300°C indicates that it is the appearance of a continuous MgO phase in this composition range which produces this effect.

Another factor which must be considered is the direct relation between the Na_2O content and the MgO content of the material. If the Na_2O is an active grain boundary flux, as proposed previously, it is likely that the presence and formation of a viscous liquid could be associated with the jump in toughness between 4MP13 and 6MP13. This is particularly compelling since intergranular fracture is predominant at this temperature.

The possibility that hydration of the CaO phase may account for this behavior cannot be ruled out despite efforts to prevent hydration by use of P_2O_5 desicant and rapid testing following specimen fabrication. It is interesting to note in this regard that the 40% and 60% MgO doped with Fe_2O_3 show a marginally significant K_{1C} increase with increased MgO at 1300°C and these specimens were observed to have good stability when exposed to the atmosphere following testing. Unfortunately the fracture results in this temperature range are difficult to interpret due to the possible presence of a liquid phase and $MgO \cdot Fe_2O_3$ precipitates.

It appears therefore, in view of the low temperature fracture results on undoped material, that the difference between the fracture

toughness of the 40% and 60% MgO materials is due to the presence of the Na_2O contaminant in the MgO raw material coupled with the appearance of a continuous MgO phase.

4.4.4. Effect of Liquid Viscosity

If the fracture behavior above 1100°C is due to extensive grain boundary sliding or viscous deformation due to the presence of a limited amount of liquid at the grain boundaries, the viscosity of the liquid should play a major role.

Relatively little information is available on the viscosity of liquid oxides except in silica-rich glass and slag-forming systems. This is only of limited applicability. Conversely little information is available as to the identity of the liquids formed in these samples. Despite this, the effect of temperature on the viscosity of steel making slag is usually given by the relation (155)

$$\eta = A\exp[\Delta E/RT]$$

where η is the viscosity at a temperature T

A is a constant

R is the gas constant

E is the "Activation Energy"

It is also well established that liquids having a well developed silicate network show high viscosities over a wide temperature range. Short-chain liquids exhibit a rapidly declining viscosity with temperature as shown in Figure 4-72.

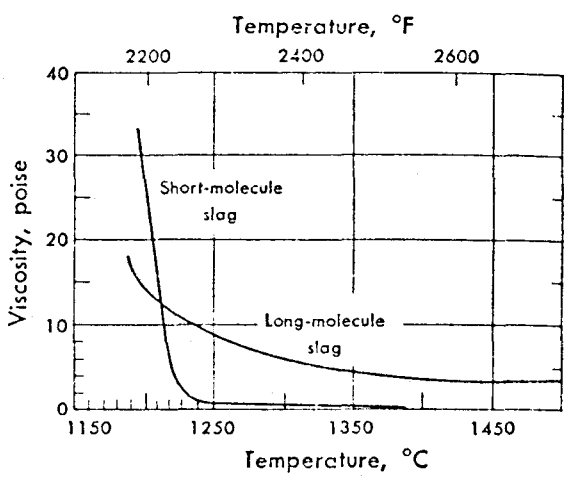

Figure 4-72 Viscosities of Long-Molecule and Short-Molecule Slags.

(Ref. 156)

In the present work the SiO_2 and TiO_2 dopants are both noted for their network forming ability whilst the other dopants do not form networks and would form fluid liquids. FeO exemplifies this as it has a viscosity of only 0.3 poise at 1400°C.

Thus in view of the potential fluidity of an iron oxide based liquid and the observed rounding of grains in the fractographs, it is likely that if a peak in toughness due to liquid formation does occur, it would be extremely narrow and difficult to detect.

4.4.5. Subcritical Crack Extension

Examination of specimens loaded to near failure strength showed the machined notch to be extended by intergranular cracking at temperatures as low as 1100°C as shown in Figures 4-73 and 4-74

The second Figure shows this effect for 60% MgO doped with Ta_2O_3 at 1100°C. This composition showed a statistically significant increase in strength over the 6MP11 and also a statistically significant (95% confidence) increase over its room temperature value. It is possible that the transition between transgranular and intergranular fracture is of particular importance here with the deflection of the crack by the grain boundaries contributing to the increased toughness.

An important implication of this result is that the blunt notches introduced by the diamond saw are capable of starting a sharp crack from the notch base prior to fracture. A corrollary of this is that the toughness values based upon the notch depth will be systematically low

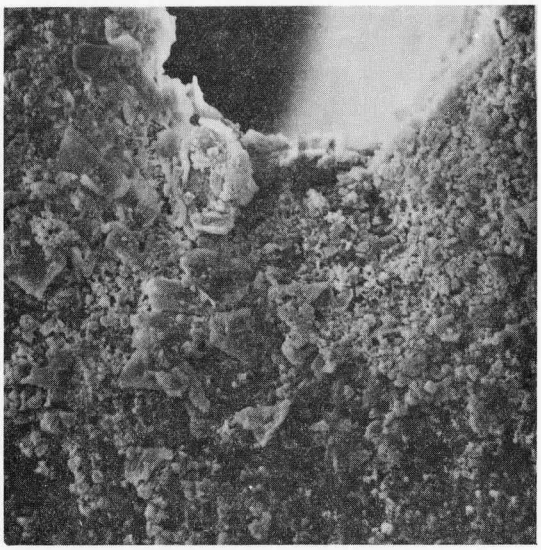

Figure 4-73a

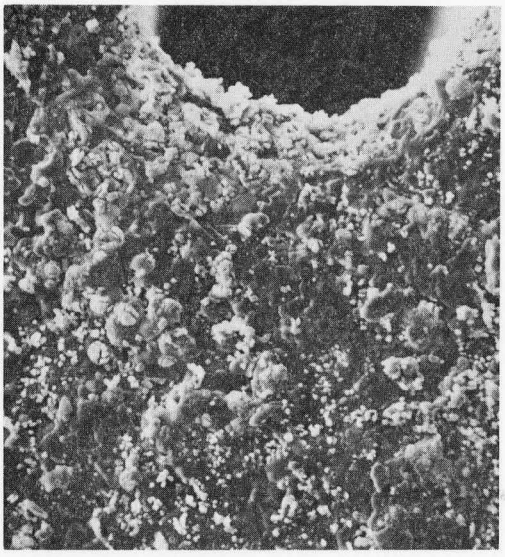

Figure 4-73b

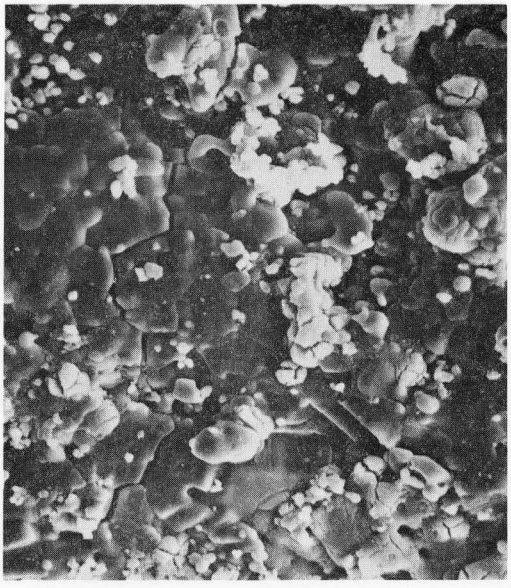

Figure 4-73c

Figure 4-73

Notch tip of a) 6Tall, b) 6Tal5, c) detail of b, following loading to less than failure load. Subcritical crack initiation can be seen in the specimen tested at 1500°C. (Magn. a) 280x, b) 280x, c) 700x)

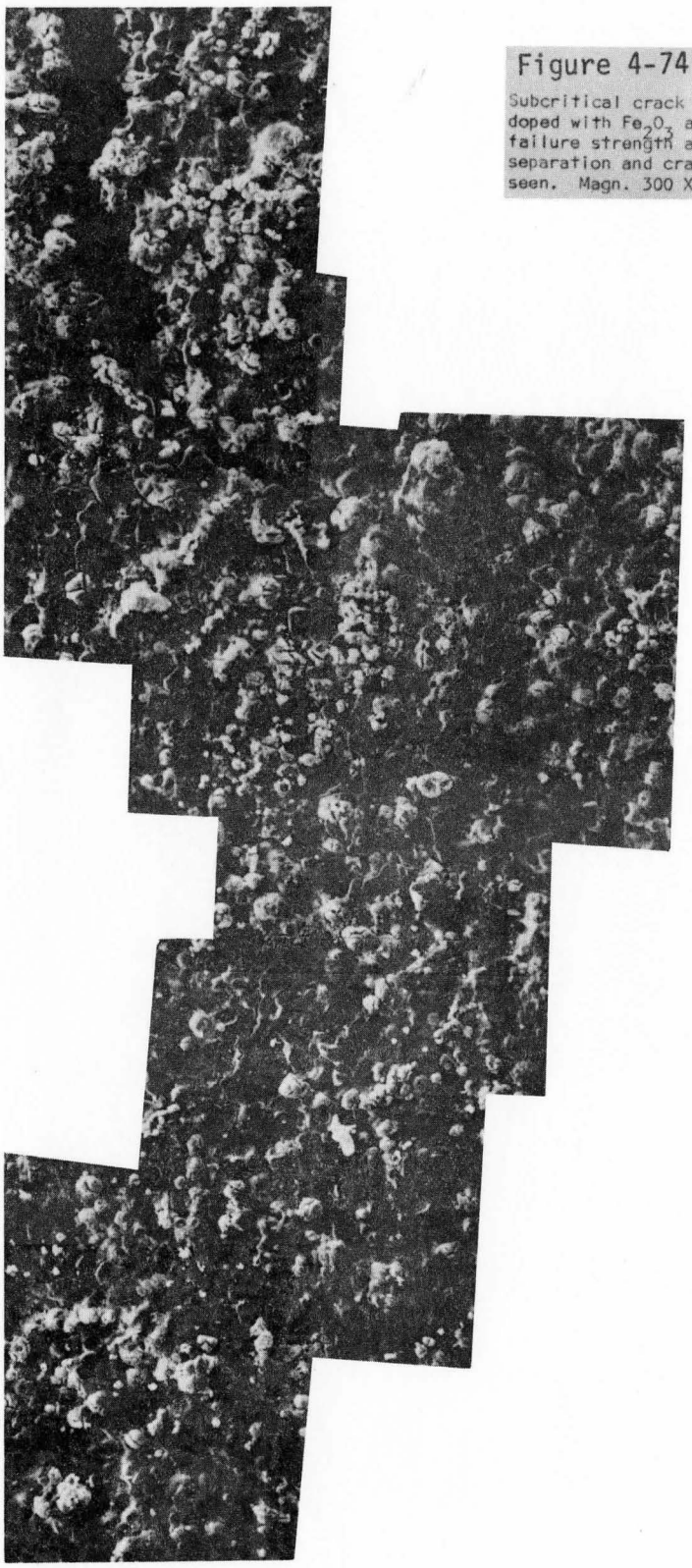

Figure 4-74

Subcritical crack growth in 60 % MgO doped with Fe_2O_x and loaded to 75 % failure strength at 1500 C. Grain separation and crack branching are seen. Magn. 300 X.

due to the subcritical crack extension.

However, as there exists no means of accurately measuring the crack position at the point of failure, no estimate of the magnitude of this effect was made. Simpson (128) in his work on Al_2O_3 studied this effect extensively and concluded that this occurs at all temperatures and results in correct values of K_{1C} only if the ratio of the crack extension to the notch root radius is greater than 0.5. This condition appears to be satisfied for specimens tested in this work.

The Fe_2O_3 doped specimens preloaded at 1500°C also showed intergranular cracking and branched in several places which extended almost half way through the sample. Transducer curves for this and other samples tested at 1500°C showed non elastic behavior, in contrast to the linear load-deformation curves produced at lower temperatures. The structure of the crack indicates that extensive grain boundary separation is occuring as would be expected in the presence of a liquid phase. Independent evidence of grain boundary liquids has already been presented in Section 4.3.5. If this liquid was highly viscous or absent, the extensive crack branching observed would be expected to increase the toughness. In this case however, the low viscosity liquid has allowed the microstructure to tear apart with little resistance resulting in a low "toughness" value.

CHAPTER 5

SUMMARY AND CONCLUSIONS

The dopants tested had very marked effects upon the grain growth and sintering of the single phase oxides. Comparison of the results in Table 4-1 (for single phase oxides) with those in Table 4-2 (for magdol compositions) it is apparent that the additives had little effect upon the grain size obtained in the magdols compared to the single phase material. This indicates that the presence of the second insoluble phase in the microstructure was the major factor controlling grain size. The fired density and fracture toughness parameters were much more strongly influenced by the additives.

In the single phase grain growth and sintering results several types of behavior occurred:

1) In the undoped material entrapped pores typical of exaggerated grain growth were noted. This may be attributed to the presence of minor levels of Na_2O in the MgO.
2) Ta_2O_5 is an effective sintering aid and grain growth promotor for MgO most probably due to a gettering action for other native impurities. Very low additions seem to be most effective. In CaO the Ta_2O_5 causes exaggerated growth but is much less effective than in

MgO. At the 0.5% level Ta_2O_5 is moderally effective in increasing sintered density.

3) TiO_2 was very effective as a sintering agent producing dense ceramics at levels up to 6.6% TiO_2 in both MgO and CaO. Increased additions result in refined grain sizes possibly due to precipitate pinning of grain boundaries.

4) SiO_2 is not effective as a sintering aid or grain growth promoter in either MgO or CaO. The inhibition of sintering is more severe in CaO than in MgO. The effect is due to the formation of highly refractory compounds at interoxide contact points.

5) Fe_2O_3 is very effective as a grain growth promoter and sintering aid in both MgO and CaO. In both cases liquid formation is responsible, iron oxide with CaO impurities in the MgO and CaO-Fe_2O_3 eutectic in the CaO system. The defect structure produced by iron solution in MgO must also be a factor in the enhanced grain growth with increased addition in MgO.

6) WO_3 is not effective as a grain growth promoter in MgO and inhibits grain growth by a precipitate mechanism. In the CaO systems grain growth was enhanced by a getting action. Increased additions result in refined grain size.

7) GeO_2 resulted in increased grain sizes with increased additions in both MgO and CaO. Liquid formation is not likely in this system and the mechanism is unknown. Further study should be done.

8) V_2O_5 results in increased grain size in CaO with increased addition. A liquid assisted grain growth process is indicated similar to that found in V_2O_5 doped MgO by other authors. The refractory strength of materials doped with V_2O_5 are very poor due to this low temperature liquid.

The effects of the oxide additives on the magdols grain size can not be correlated with the behavior observed in the single oxides, while the bulk density values can be partially correlated.

1) In the case of silica a very uniform grain size was obtained. However, the bulk densities were disappointing. The increase in bulk density with MgO content is due to the reduced number of CaO-SiO_2 contacts.

2) Iron oxide doping resulted in very high bulk densities due to liquid formation however grain size was much smaller than expected from single oxide study due to the presence of the second insoluble phase.

3) TiO_2 doping also produced relatively good densities of near 90% theoretical showing a minimum grain size at 60% MgO which corresponds to the maximum number of unlike contact

points. The grain size of MgO is less than that of the CaO like the undoped material and in contrast to the single oxide results. The increased densities are consistent with limited liquid formation during sintering.

4) Tantalum oxide was not effective in modifing the microstructure of the magdols as the CaO grains were larger than the MgO grains and the sintered density was very poor. Again these results are consistant with solid state sintering.

5) GeO_2 was also found to produce poor sintered densities.

The results of the fracture tests at elevated temperatures showed much more distinctive variations and can be interpreted with greater ease. The conclusions are as follows:

1) The undoped material was strongly affected by the Na_2O contamination in the MgO. The development of a peak in toughness near 1300°C with increased MgO content is due to grain boundary sliding due to grain boundary concentration of impurities.

2) Additions of SiO_2 and Ta_2O_5 resulted in increased high temperature fracture toughness by forming stable precipitates either preventing grain boundary sliding or "getting" the impurities. Decompositon reactions at high temperatures produce micro cracks which moderately increase toughness in both cases.

3) TiO_2 additions result in a viscous liquid formation leading to high toughness followed by rapid decline as temperature increases.

4) Fe_2O_3 resulted in a very fluid liquid which resulted in rapid loss of toughness at a low temperature.

Finally several topics for future work were noted. The kinetics of grain growth and sintering of two phase solids has not been well investigated theoretically. The mechanisms by which more additions cause enhanced grain growth have not been clearly identified in the literature and more study is required.

Of more practical importance the effects of these additives should be evaluated in combination and in commercially available dolomite.

APPENDIX I

ORIGIN OF THE NUMERICAL CONSTANT IN THE K_{1C} EQUATION

The K_{1C} formula derived by Brown and Strawley (143) for 4 point bend is

$$K_{1C} = Y6Ma^{\frac{1}{2}}/BW^2$$

where Y is a constant

M is the bending moment

a is crack length

B is beam depth

W is beam width.

In order to convert this to a form convenient for use the quantity Lx, where L is one half of the total load P and x is the distance between the knife edges, must be substitued for the bending moment M giving

$$K_{1C} = Y3Pgx\ a^{\frac{1}{2}}/(BW^2 \times 10^{-6})$$

where g is the acceleration due to gravity and the 10^{-6} factor serves to convert the dimensions of the specimen from centimeters to meters thus yielding units of $MN/m^{3/2}$.

APPENDIX II

STATISTICAL TREATMENT OF EXPERIMENTAL DATA

References

1. Statistical Treatment of Experimental Data, H.D. Young, McGraw Hill, 1962.
2. Simplified Statistical Analysis, H.H. Holscher, Cahners Books, 1971.

Propagation of error

The relation used to calculate the fracture toughness was:

$$K_{1C} = \frac{6YaL\sqrt{n}}{bw^2}$$

The errors associated with each of the measured values was estimated and using the propagation of error theory

$$\text{Experimental error} = \sum_{1}^{n} \varepsilon_i^2$$

where ε_i is is fractional error.

A typical set of results is;

$$K_{1C} = 1.122 \pm .040 MN/m^{3/2}$$

Comparing this error with the standard deviation of .173 for this set of data, it is seen that the experimental error is much less than standard deviation and it is therefore reasonable to quote the standard deviations rather than experimental errors.

Rejection of Experimental Data

Any experimental data may safely be rejected if there is any a priori reason for suspecting its validity. However occassionally data is obtained which is highly unusual possibly due to some undetected error in procedure. In order to decide upon the rejection or acceptance of data Chauvenets Criterion was used. This states that data should be rejected if the probability P of obtaining it is $< 1/2N$ where N is the number of measurements. If P(T) is the probability of a measurement falling within $T\sigma$ of the mean of a normal distribution then we must find T such that for a group of six samples

$$P(T) = 1 - 1/(2 \times 6) = .9167$$

thus $T = 1.73$.

Thus any value amoung six values which deviates from the mean by more than 1.73σ has less than 1/2N probability of occuring and should be discarded.

t Test

Small smaple statistics depends upon the best estimate available of the standard deviation of the data in order to test for significant

differences. Thus for the data collected in this work the t test was used to determine if any significant differences existed in the K_{1C} values of the bars doped with different additives. This is defined as follows:

$$t = \frac{\bar{x}_1 - \bar{x}_2}{\left[\frac{\sigma_1^2}{N_1} + \frac{\sigma_2^2}{N_2}\right]^{1/2}}$$

where $\bar{x}_1, \bar{x}_2$ are the two sample means

σ_1, σ_2 are the two samples standard deviations

N_1, N_2 are the two numbers of samples.

For the purposes of this work a 90% probability of significant difference can be considered an indication of an effect which is considerably less than the confidence level usually quoted, however since these ceramic materials are highly variable compared to other applications of this statistic this procedure can be justified.

Significant Digits

In order to obtain the maximum benefit from statistical analysis more digits should be carried than are significant as differences in samples may be hidden by rounding. Accordingly more digits than ordinarily presented are carried throughout the work.

REFERENCES

1. Halm, L. "Magnesite or Dolomite?", J. Brit. Cer. Soc., 7, 42 (1970).

2. Gilpin, W.C. "Magnesite and Dolomite", Ref. J., April, (1972).

3. Jackson, B. & Laming, J. "Significance of Mechanical Properties of Basic Refractories", T. Brit. Cer. Soc., 68 21 (1969).

4. Lu, W.K. & Nicholson, P.S. Proposal to AISI, McMaster 1976.

5. Dasguta, D.R. "Decomposition of Dolomite", Min. Mag., 36, 138 (1962).

6. Ohba, H. Taikabutsu, 17[94], 364 (1965).

7. Bradley, W. Amer. Min., 38, 207 (1965).

8. Britton, H.T.S., Greg, S.J., & Wilsor, G.L. "Calcination of Dolomite II", Trans. Far. Soc., 48, 63 (1952).

9. Obst, V.K.H. "Solubility of CaO and MgO in Calcined Dolomite", Tonind Ztg. 90[9], 411 (1966).

10. Leipold, M.H. "Impurity Distribution in MgO", J. Amer. Cer. Soc., 49[8], 498 (1966).

11. Leipold, M.H. "Grain Boundary Impurities", Chapter 12, Ceramic Microstructures, (ed.Pask & Fulrath), Wiley (1968).

12. Cutler, I. High Temperature Materials, Vol 5-III, Pg. 161, (ed. Alper), Academic (1970).

13. Nawaz, G. Phd Thesis, M.I.T., 1948.

14. Livey, D.T., Wankyn, B.M., Hewitt M., Murray P. Trans. Brit. Cer. Soc., 56[5], 217 (1957).

15. Allison, A.G., Sesler, E.C., Haldy, N.L., & Duckworth, W.H. "Sintering of High Purity Magnesia", J. Amer. Cer. Soc., 39[4], 151 (1956).

16. Henney, J.W. & Jones, J.W.S. "Effect of Ge_2O_3 Vapour on Sintering MgO", T. Brit. Cer. Soc., 68, 20 (1969).

17. Quirk, J.E. J. Amer. Cer. Soc. 42[4], 178 (1959).

18. Hyde, C. & Duckworth, W.H. Wadd Tech., Rpt., 61-262 Contract AF 33 (616) - 6238 June 1961.

19. Kriek, H.T.S., Ford, W.F., & White, J. "Effect of Additions on the Sintering of MgO", T. Brit. Cer. Soc., 58 Pg. 1, (1959).

20. Rosenquist, T. "Principles of Extractive Metallurgy", Pg. 238, McGraw-Hill (1973).

21. Iwai, S., Murotani, H., Morikawa, H., & Aoki, H. Yogyp Kyokai Shi 77 [12], 411 (1969).

21a. Eubank, W.R. J. Amer. Cer. Soc., 34[8], 225 (1951).

22. Hench, L.L., & Russel, R. "Effect of Cr_2O_3 Vapourization on the Sintering of MgO", T. Brit. Cer. Soc., 67, Pg. 377 (1968).

23. Oh, K., Morikawa, H., Iwai, S., Aoki, H. Thermal Decomposition and Sintering of Synthetic Magnesite, Yogyo Kyokai Shi, 82 [8], 442 (1974).

24. Moodie, A.F., Warble, C.E., & Williams, L.S. "Magnesia Precursor & Sintering Study", J. Amer. Cer. Soc., 49 [12], 676 (1966).

25. Saraeda, O. "Properties of Quick Lime Obtained under different conditions of Calcination", Gypsum & Lime, 100, Pg. 12 (1969).

26. Brown, R.A. "Sintering in CaO and CaO containing Strontium", J. Amer. Cer. Soc., 44 [9], 693 (1965).

27. Fisher, H.C. "Calcination of Calcite I", J. Amer. Cer. Soc., 38 [7], 245 (1955).

28. Fisher, H.C. "Calcination of Calcite II", J. Amer. Cer. Soc., 38 [8], 284 (1955).

29. Cutler, I.B., Jones, J.T. & Maitra, P.K. "Role of Structural Defects in Sintering MgO and Al_2O_3", J. Amer. Cer. Soc., 41 [9], 353 (1958).

30. Cutler, I.B. High Temperature Materials, Vol 5-III (ed. Alper) Academic Press (1972).

31. Jorgenson, B.J., & Westbrook, J.H. "Role of Solute Segregation at Grain Boundaries during Final Stage Sintering of Al_2O_3, J. Amer. Cer. Soc., 47 [7], 332 (1964).

31a. Hollenberg, G.W., & Gordon, S. "Origin of Anomalously high Activation Energies in Sintering of Impure Refractory Oxides", J. Amer. Cer. Soc., 56 [2], 109 (1973).

32. Doman, R.C., Bar, J.B., McNally, R.M., & Apler, A.M. "Phase Equilibrium in the system CaO-MgO", J. Amer. Cer. Soc., 46 [7], 67 (1963).

33. Burke, J.E. "Grain Growth", Chp.33, Ceramic Microstructures, ed. Pask & Fulrath, Wiley 1968.

34. Burke, J.E. "Role of Grain Boundaries in Sintering", J. Amer. Cer. Soc., 40 [3], 80 (1957).

35. Frenkel, J. J. Phys., 9 385 (1945).

36. Coble, R.L. J. Amer. Cer. Soc., 41, 55 (1958).

37. Coble, R.L. J. App. Phys., 32, 787 (1961).

38. Coble, R.L., & Burke, J.E. Progress in Ceramic Science, Pg 197-253, Vol. 3, (ed. Burke, J.E.), Pergamon Press 1963.

39. Johnson, D.L. "General Model for the Intermediate Stage of Sintering", J. Amer. Cer. Soc., 53 [10], 574 (1970).

40. Beere, W. "Unifying Theory of Stability of Penetrating Liquid Phase and Sintering of Bodies", ACTA MET., 23 [1], 131 (1975).

41. Beere, W. "Second Stage Sintering Kinetics of Powder Compacts", ACTA MET, 23 [1], 139 (1975).

42. Beere, W. "Critical Assessment of the Intermediate Stage of Sintering", Met. Sci., 10 [8], 294 (1976).

42a. Anderson, P.J. & Morgan, P.L. "Effect of H_2O on Sintering MgO", Faraday Soc. Trans 60, 930 (1964).

42b. Eastman, P.F., & Cutler, I.B. "Effect of H_2O in Sintering MgO", J. Amer. Cer. Soc., 49 [10], 526 (1966).

42c. Peterson, D.O., & Cutler, I.B. "Effect of H_2O on Sintering of CaO", J. Amer. Cer. Soc., 51 [1], 21 (1968).

43. Kuczynski, G.C. "Sintering in Multi Component Systems", Pg. 685 in Sintering and Related Phenomenon, (ed. Kuczynski, G.C.) Gordon & Breach (1967).

44. Eremenko, E. Liquid Phase Sintering, Consultants Bureau, N.Y. (1970).

45. White, J. Materials Science Research, Pg. 8, Vol.6, (ed. Kuczynski, G.C.) Plenum Press (1973).

46. Huppman, M. "Sintering in the presence of a Liquid Phase", Ibid, Vol 10.

47. Whalen, T.J. & Hamenik, M. Sintering and Related Phenomenon, Pg. 715 (ed. Kuczynski) Gordon & Breach (1967).

48. Kingery, W.D. "Densification during Sintering in the Presence of a Reactive Liquid", J. App. Phys., 30 [3], 301 (1959).

49. Danials, A.U., Lowrie, R.C., Gibby, R.L., & Cutler, I.B. "Observation of Normal Grain Growth in CaO and MgO" J. Amer. Cer. Soc., 45 [6], 282 (1962).

50. Rice, R.W. "Fabrication and Characterization of CaO", J. Amer. Cer. Soc., 52 [8], 420 (1969).

51. Hepworth, M.A, & Rutherford, J. "Fabrication of High Density CaO Ceramics", Amer. Cer. Soc. Bull., 43 [1], 18 (1964).

52. Kapaddia, C.M. & Leipold, M.H. "Grain Growth in Pure Dense MgO", J. Amer. Cer. Soc., 57 [1], 41 (1974).

53. Spriggs, R.M., Brissette, L.A. & Vasilos, T. "Grain Growth in Fully Dense MgO", J. Amer. Cer. Soc., 47 [8], 417 (1964).

54. Gupta, T.K. "Sintering of MgO: Densification and Grain Growth", J. Mat. Sci., 6, 25 (1971).

55. Lowrie, R.C., & Cutler, I.B. "The Effect of Porosity on the Rate of Grain Growth in MgO", in Sintering and Related Phenomenon, (ed. Kuczynski, G.C.) Plenum (1967).

56. Cutler, I.B. "Sintered Alumina and Magnesia"in High Temperature Materials, Vol 5-III, (ed.Alper) Academic (1970).

57. MacEwan, J.R. "Grain Growth in Sintered UO_2", J. Amer. Cer. Soc., 45 [1], 37 (1962).

58. Gordon, R.S., Marchant, D.D., & Hollenberg, G.W. "Effects of Small Amounts of Porosity on Grain Growth of Hot Pressed MgO and Magnesiowustite", J. Amer. Cer. Soc., 53 [7], 399 (1970).

59. Smith, C.S. "Grain Phases and Interfaces:An Interpretation of Microstructure", A.I.M.E., 175, 15 (1948).

60. White, J. "Magnesia Based Refractories", Pg. 124 in High Temperature Materials, Vol 5-I (ed. Alper) Academic (1970).

61. Busit, D.S., Ford, W.E., Jackson, B., & Stephenson, I.M. "Kinetics of Grain Growth in 2 Phase Solid-Liquid Systems," T. Brit. Cer. Soc., 64, 173 (1965).

62. Stevenson, I.M., & White, J. "Factors controlling Microstructures in 2 and 3 Phase Solid-Liquid Systems", Ibid 66, 443 (1967).

63. Jackson, B., & Ford, W.F. Ibid 65, 19 (1966).

64. Richmond, C. Phd Thesis, Sheffield (1971).

65. Richmond, C. Unpublished work (1968) quoted by White Ref. 45.

66. Tacvorian, S. Bull. Fran. Ceram. 23, 3 (1954).

67. Tacvorian, S. Compt. Ren., 234, 2363 (1952).

68. Tacvorian, S. O.N.E.R.A., Pub. No.78, 32 (1955).

69. Radcliffe, P.S. Private Communication (1976).

70. Nelson, J.W. & Cutler, I.B. "Effect of Oxide Additions on the Sintering of MgO", J. Amer. Cer. Soc., 41 [10], 406 (1958).

71. Nelson, J.W., & Cutler, I.B. "Effect of Oxide Additions on the Sintering of MgO", Tech. Rpt. #11, AECL 3848-20F2 (1956).

72. Layden, G.K., & McQuarrie, M.C. "The Effect of Additives on MgO", J. Amer. Cer. Soc., 42 [2], 89 (1959).

73. ---------- Phase Diagrams For Ceramists, Plate 237, Pub. by Amer. Cer. Soc.

74. ---------- Ibid, Plate 2314.

75. ---------- Ibid, Plate 598.

76. Mateki J. Cer. Assn. Jap. 60, 17 (1952).

77. Nicholson, G.C. "Grain Growth in MgO containing Iron Oxides and Titanium Oxide", J. Amer. Cer. Soc., 49 [1], 47 (1966).

78. Riegger, O.K., Madden, G.I., & Van Vlack, L.H. "Microstructure of Periclase when subjected to Steel making Variables", A.I.M.E. MET. TRANS 227, 97 (1963).

79. Greenwood, G.W. "Growth of Dispersed Precipitates in a Solution", ACTA MET, 4 [5], 243 (1956).

80. ---------- Phase Diagrams for Ceramists, Plate 2154, Publ. by Amer. Cer. Soc.

81. ---------- Ibid, Plate 4203.

82. ---------- Ibid, Plate 2216.

83. ---------- Ibid, Plate 2218.

84. ---------- Ibid, Plate 2108

85. ---------- Ibid, Plate 43.

86. Tanaka J. Soc. Chem. Ind. Jap., 42 [6], 387 (1939).

87. ---------- Phase Diagrams for Ceramists, Plate 4336, Pub. by Amer. Cer. Soc.

88. ---------- Ibid, Plate 4312.

89. ---------- Ibid, Plate 4553.

90. Rouf, M.A., Cooper, A.H., & Bell, H.B. T. Brit. Cer. Soc. 68, 263 (1969).

91. ---------- Phase Diagrams for Ceramists, Plate 2318, Pub. by Amer. Cer. Soc.

92. ---------- Ibid, Plate 4316.

93. Brown, R.A. "Sintering of Very Pure MgO and MgO containing Vanadium", Am. Cer. Soc. Bull.44 [6], 483 (1965).

93a. Nicholson, G.C. "Grain Growth in MgO Containing a Liquid Phase", J. Amer. Cer. Soc., 48 [10], 525 (1965).

94. Alvarez-Estranda, Botia — Bol. Soc. Espan. Ceram. 5 [2], 201 (1966).

95. Sano, G., & Kogjo, M. — Nagoya Kogyo Gijutsu Shikensko Hokoko, 14 [5], 201 (1965).

96. ---------- — Phase Diagrams for Ceramists, Plate 4335, Pub. by Amer. Cer. Soc.

97. ---------- — Ibid, Plate 4341.

98. ---------- — Ibid, Plate 251.

99. ---------- — Ibid, Plate 2306

99a.---------- — Ibid, Plate 2320.

100.---------- — Ibid, Plate 4309.

101.---------- — Ibid, Plate 264.

102.---------- — Ibid, Plate 2470.

103. Arias, A. — "Effect of Inclusions on Grain Growth of Oxides", J. Amer. Cer. Soc., 49 [1], 621 (1966).

104. Budnikov, PP., Volodin, P.L., & Tresuyatskii, S.G. — Ogneupory 25, 70 (1960).

105. Budnikov, P.P., Matveev, M.A., & Yanovskii, V.K. — Ogneupory 30, 32 (1965).

106. ---------- — Phase Diagrams for Ceramists, Plate 2472, Pub. by Amer. Cer. Soc.

107. Atlas, L.M. — "Sintering of MgO with Li_2O", J. Amer. Cer. Soc., 40 [6], 196 (1957).

108. Hart, P.E., Atkin, R.B., & Pask, J.A. — "Densification of MgO with LiF", J. Amer. Cer. Soc., 53 [2], 83 (1970).

109. Rice, R.W. — "Production of Transparent Polycrystaline MgO", (Abstract) Am. Cer. Soc. Bull.41, [4], 271 (1962).

110. Pagett, G.C., & Cox, J.A., & Clements, J.F. "Stress Strain Behavior of Refractories at High Temperatures", J. Trans. Brit. Cer. Soc., 68, 63 (1969).

111. Lythe , T.W., & Pagett, G.C. "Equipment for Determining High Temperature Properties of Basic Refractories", J. & T. Brit. Cer. Soc., 68, 43 (1969).

112. Jenkins, G.M. Br. J. App. Phys., 13, 29 (1962).

113. Copley, S.M., & Pask , J.A. "Deformation of Polycrystaline Ceramics", in Mat. Sci. Res. Vol. 13 (ed. Kriegel & Palmour) Plenum (1966).

114. Copley, S.M. & Pask, J.A. "Deformation of Polycrystaline Ceramics", J. Amer. Cer. Soc.,48 [12], 636 (1965).

115. Murray Unpublished work quoted as Ref. 23, by Copley & Pask (Ref. 113).

116. Selsing, J. "Internal Stress in Ceramics", J. Amer. Cer. Soc., 44 [8], 419 (1961).

117. Hasselman, D.P.H., & Fulrath, R.M. "Effect of Cylindrical Porosity on Youngs Modulus of Polycrystaline Brittle Ceramics", J. Amer. Cer. Soc., 48 [10], 545 (1965).

118. Dieter, G.E. Mechanical Metallurgy, Pg. 444, McGraw Hill (1961).

119. Davies, D.G.S. "Statistical Approach to Engineering design in Ceramics", Proc. Brit. Cer. Soc., #22, Pg. 429, (1973).

120. Kingery , W.D. Introduction to Ceramics, Wiley (1961).

121. Green, D.J. Phd Thesis, McMaster 1976.

122. -------- Fracture Toughness, ISI #121, Iron & Steel Institute (1968).

123. Gilman, J.J. "Strength of Ceramic Crystals" in Physics and Chemistry of Ceramics, (ed. Klingsberry), Pg. 240, Gordon & Breach (1963).

124. Mendelson, M.I., & Fine, M.E. "Enhancement of Fracture Properties of Wustile by Precipitates", J. Amer. Cer. Soc., 57 [4], 154 (1974).

125. Knudsen, F.P. "Effect of Porosity on Youngs Modulus of Al_2O_3" J. Amer. Cer. Soc.,45 [2], 94 (1962).

126. Pabst, R.F. "Determination of K_{1C} factors with Diamond Saw Cuts in Ceramics", Fracture Mechanics of Ceramics 2 (ed. Bradt, Hasselman and Lange), Plenum 1974.

127. Davage , R.W. & Tapin , G. "Effects of Temperature and Enviroment on the Strength of 2 polycrystaline Aluminas", Proc. Brit Cer. Soc., 15,47 (1970).

128. Simpson , L.A. J. Amer. Cer. Soc., 57 [4], 151 (1974).

129. Cahn J.W. "The Impurity- Drag effect in Grain Boundary Motion", ACTA MET., 10 [9], 789 (1962).

130. Westbrook , J.H. Analysis of the Nature of Grain Boundaries, Chapter 8 in Ceramic Microstructures, (ed. Pask& Fulrath) Wiley (1968).

131. Shewmon , P.G. Transformations in Metals, Pg. 117, McGraw Hill (1969).

132. Hillert "On the Theory of Normal and Abnormal Grain Growth", ACTA MET., 13, 227 (1965).

133. Feltham, P. "Grain Growth in Metals", ACTA MGT., 5 [2], 97 (1957).

134. Aust, K.T. & Rutter, J.W. TRANS AIME, 224, 111 (1962).

135. Thumler, F. & Thomma, W. Met. Rev. 115, The Metals and Metallurgical Trust (1967).

136. Stuijts, A.L. Annual Review of Materials Science,Pg. 363, (ed. Huggins, Bube & Roberts), Annual Reviews Inc. (1973).

137. Johnson, D.L. "General Models for the Intermediate Stage of Sintering", J. Amer. Cer. Soc., 53 [10], 574 (1970).

138. Beere, W. "Critical Assessment of the Intermediate Stage of Sintering", Mer. Sci., 10 [8], 294 (1976).

139. Claussen, N., Pabst, R., & Lahman, C.P. "Influence of Microstructure of Al_2O_3 and ZrO_2 on K_{1C}", Proc. Brit. Cer. Soc., 25, 139 (1975).

140. Davidge, R.D., & Tapin, G. "Effect of Temperature and Environment on the Strength of Polycrystaline Alumina", Ibid, 15, 47 (1970).

141. Chan, W. "Thermal Cycling of Fusion Cast Refractories", M. Eng. Thesis, McMaster (1976).

142. Evans, G., & Wiederhorn, S.M. "Crack Propagation and Failure Prediction in Silicon Nitride at Elevated Temperatures", J. Mat. Sci. 9, 270 (1974).

143. Brown, W.F., & Scrawley, J.E. ASTM STP 410, ASTM (1966).

144. Weiderhorn, S.M. J. Amer. Cer. Soc., 50 [8], 407 (1967).

145. Rice, R. "Strength Grain Size Effects in Ceramics", Proc. Brit. Cer. Soc., 20, 205 (1972).

146. Evans, G., & Davidge, R.W. "Strength and Fracture of Fully Dense Polycrystalline MgO", Phil. Mag., 1969, Pg. 373.

147. Simpson, L.A., & Merrett, G.J. "Effect of Annealing on Toughness, Strength and Microstructure of Hot Pressed Alumina", J. Mat. Sci. 9, 685 (1974).

148. Bailey, J.E., & Hill, N.A. "Effect of Porosity and Microstructure on the Mechanical Properties of Ceramics", Proc. Brit. Cer. Soc., 15, 15 (1970).

149. Gardner, R.E., & Robinson, G.W. "Improved Polishing for Ultra High Density MgO", J. Amer. Cer. Soc., 45 [2], 46 (1963).

150. Richardson, J.H. — Optical Microscopy for the Materials Sciences, McGraw Hill (1970).

151. Sweeting, T.B., & Pask, J.A. — "Effect of Processing on Microstructure and Mechanical Properties of MgO", J. Amer. Cer. Soc., 59 [5,6], 226 (1976).

152. Radcliff, P.S. — Private communication (1976).

153. Nakamura, T. — MSc Thesis, Utah (1962).

154. Samsonov, G.V. — Oxide Handbook, Plenum (1973).

155. Lay, K.W. — J. Amer. Cer. Soc., 51 [7], 373 (1968).

156. Elliott, J.F. — Thermochemistry for Steelmaking, Pg. 659 (ed. Elliott, Gleiser and Ramakrishna), Addison Welsly, (1963).

157. Evans, A.G., Gilling, D., & Davidge, R.D. — "Temperature Dependence of the Strength of Polycrystaline MgO", J. Mat. Sci. 5, 187 (1970).

158. Green, D.J. — MSc Thesis, McMaster (1972).

159. Evans, G.C. — Progress in Materials Science, Pg. 241, Vol. 21, No. 3/4 (1976).

160. Coppola, J.A., & Bratt, R.C. — "Effect of Porosity on Fracture of Al_2O_3", J. Amer. Cer. Soc., 56 [7], 392 (1973).

161. Evans, G.C., Heuer, A.H., & Porter, D.L. — "Fracture Toughness of Ceramics", Pg. 537 in Fracture 1977, Vol. I, Waterloo (1977).

162. Lu, W.K. — Alkalies in the Blast Furnace, McMaster (1973).

163. Chesters, J.H. — Refractories for Iron & Steelmaking, Metals Society (1974).